A fabrication process for flexible single-crystal perovskite devices

https://doi.org/10.1038/s41586-020-2526-z

Received: 5 October 2019

Accepted: 22 May 2020

Published online: 29 July 2020

Check for updates

Yusheng Lei[1,9], Yimu Chen[1,9], Ruiqi Zhang[1], Yuheng Li[1], Qizhang Yan[1], Seunghyun Lee[2], Yugang Yu[3], Hsinhan Tsai[4], Woojin Choi[5], Kaiping Wang[3], Yanqi Luo[1], Yue Gu[3], Xinran Zheng[6], Chunfeng Wang[7], Chonghe Wang[1], Hongjie Hu[1], Yang Li[1], Baiyan Qi[3], Muyang Lin[1], Zhuorui Zhang[1], Shadi A. Dayeh[1,3,5], Matt Pharr[2], David P. Fenning[1], Yu-Hwa Lo[3,5], Jian Luo[1,3], Kesong Yang[1], Jinkyoung Yoo[4], Wanyi Nie[4] & Sheng Xu[1,3,5,8]✉

Organic–inorganic hybrid perovskites have electronic and optoelectronic properties that make them appealing in many device applications[1–4]. Although many approaches focus on polycrystalline materials[5–7], single-crystal hybrid perovskites show improved carrier transport and enhanced stability over their polycrystalline counterparts, due to their orientation-dependent transport behaviour[8–10] and lower defect concentrations[11,12]. However, the fabrication of single-crystal hybrid perovskites, and controlling their morphology and composition, are challenging[12]. Here we report a solution-based lithography-assisted epitaxial-growth-and-transfer method for fabricating single-crystal hybrid perovskites on arbitrary substrates, with precise control of their thickness (from about 600 nanometres to about 100 micrometres), area (continuous thin films up to about 5.5 centimetres by 5.5 centimetres), and composition gradient in the thickness direction (for example, from methylammonium lead iodide, $MAPbI_3$, to $MAPb_{0.5}Sn_{0.5}I_3$). The transferred single-crystal hybrid perovskites are of comparable quality to those directly grown on epitaxial substrates, and are mechanically flexible depending on the thickness. Lead–tin gradient alloying allows the formation of a graded electronic bandgap, which increases the carrier mobility and impedes carrier recombination. Devices based on these single-crystal hybrid perovskites show not only high stability against various degradation factors but also good performance (for example, solar cells based on lead–tin-gradient structures with an average efficiency of 18.77 per cent).

The schematic and optical images in Fig. 1a illustrate the fabrication process of single crystals using a solution-based lithography-assisted epitaxial-growth-and-transfer method. A bulk crystal of hybrid perovskites (for example, methylammonium lead iodide, $MAPbI_3$) serves as the substrate to epitaxially grow single-crystal hybrid perovskites (see Supplementary Discussion 1 and Supplementary Figs. 1–3 for more details). A 2-μm layer of patterned polymer (for example, parylene) serves as the growth mask[13,14] (Extended Data Fig. 1). The as-grown epitaxial single-crystal film can be transferred to an arbitrary substrate, maintaining a good crystallinity and a strong adhesion to the substrates (Extended Data Fig. 2; see Supplementary Discussions 1 and 2 and Supplementary Figs. 2–9 for more details). Figure 1b shows scanning electron microscope (SEM) images of an intact single-crystal $MAPbI_3$ thin film transferred onto a curved general substrate, with dimensions of about 1 cm × 1 cm × 2 μm and a monolithic cross-section without any grain boundaries that are typically seen in polycrystalline $MAPbI_3$ thin films (Fig. 1b, inset, and Supplementary Fig. 10). With a more rigid growth mask, a scaled single-crystal $MAPbI_3$ thin film with dimensions of about 5.5 cm × 5.5 cm × 20 μm can be achieved (Extended Data Fig. 3; see Supplementary Discussion 3 for more details).

A high-resolution transmission electron microscope (TEM) image further reveals the epitaxial relationship and an absence of dislocations in the as-grown $MAPbI_3$ single-crystal thin film (Fig. 1c). θ–2θ X-ray diffraction (XRD) and photoluminescence (PL) studies prove the high crystallinity of the single-crystal $MAPbI_3$ thin films fabricated by this growth-and-transfer method (Fig. 1d, e). Similar full-width at half-maximum (FWHM) of the XRD ω-scan (400) and PL peaks of the as-fabricated single-crystal $MAPbI_3$ thin films to those of the bulk single crystals indicate their comparably high crystal quality (Fig. 1d, e; see Supplementary Discussion 4 and Supplementary Fig. 11, 12 for more details). The high crystal quality is attainable over a growth temperature ranging from 80 °C to 160 °C (Fig. 1d, bottom), indicating the potential broad applicability of this growth-and-transfer method to other perovskites with different growth temperatures and crystallization conditions. Furthermore, the ratio of the PL intensity (I_{PL}) of the transferred epitaxial single-crystal thin film to the excitation intensity (I_E) shows a

[1]Department of Nanoengineering, University of California San Diego, La Jolla, CA, USA. [2]Department of Mechanical Engineering, Texas A&M University, College Station, TX, USA. [3]Material Science and Engineering Program, University of California San Diego, La Jolla, CA, USA. [4]Los Alamos National Laboratory, Los Alamos, NM, USA. [5]Department of Electrical and Computer Engineering, University of California San Diego, La Jolla, CA, USA. [6]Department of Physics, Tsinghua University, Beijing, People's Republic of China. [7]College of Physics and Optoelectronic Engineering, Shenzhen University, Shenzhen, People's Republic of China. [8]Department of Bioengineering, University of California San Diego, La Jolla, CA, USA. [9]These authors contributed equally: Yusheng Lei, Yimu Chen. ✉e-mail: shengxu@ucsd.edu

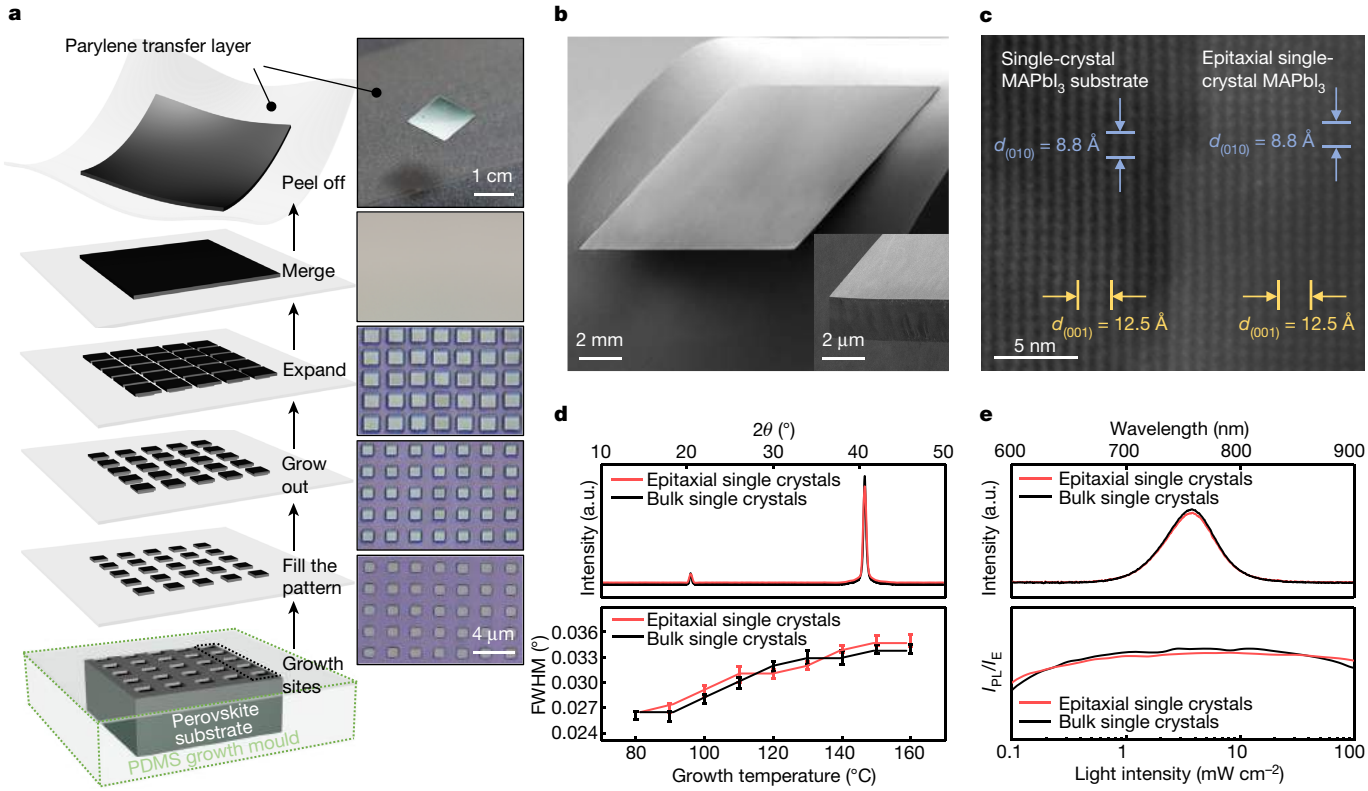

Fig. 1 | The lithography-assisted epitaxial-growth-and-transfer method for fabricating high-quality, single-crystal hybrid perovskite thin films. **a**, Schematics (left) and corresponding optical images (right) showing the solution-based epitaxial growth, merging and transferring processes of the single-crystal perovskite thin film. The bottom four optical images share the same scale bar, 4 μm. **b**, SEM images showing a single-crystal $MAPbI_3$ thin film with dimensions of about 1 cm × 1 cm × 2 μm on a bent PDMS substrate. Inset: magnified cross-section of the thin film without grain boundaries. **c**, A high-resolution TEM image showing the interfacial area of the homo-epitaxial single-crystal $MAPbI_3$. The epitaxial layer shows a well-aligned tetragonal lattice structure without dislocations. Contrast across the interface comes from different batches of growth solutions[33]. *d*, *d*-spacing. **d**, θ–2θ XRD comparison between the bulk single-crystal and the transferred epitaxial single-crystal thin film (on a PDMS substrate), showing that this growth-and-transfer method does not degrade the material crystallinity. The FWHM of the (400) peak in XRD ω-scan suggests high-quality, single-crystal perovskite thin films can be grown over a wide range of temperatures, which is applicable for different materials in the perovskite family. The error bars show the range from three measurements. **e**, PL and PL intensity comparisons between bulk single crystals and transferred epitaxial single-crystal thin films, showing the high quality of the transferred single-crystal thin films.

close tendency to that ratio of the bulk single crystal (Fig. 1e, bottom), providing additional evidence that this growth-and-transfer method will not cause noticeable non-radiative recombination or quenching in the transferred epitaxial single-crystal thin film[15,16].

The carrier diffusion length of the single-crystal thin film with different thicknesses has been calculated by measuring the carrier mobility and carrier lifetime using time-of-flight (ToF) and time-resolved PL (Extended Data Fig. 4 and Supplementary Discussion 5). The results show that the carrier mobility and the carrier lifetime increase with the crystal thickness. This can be attributed to the better crystal quality of the larger thickness, where there is a lower surface-to-volume ratio, a lower trap density, and smaller XRD and PL FWHM values in thicker films, as evidenced by thickness-dependent crystal-quality studies (Supplementary Fig. 13)[6]. The carrier diffusion length is estimated to saturate at about 5–7 μm, indicating that most charge carriers in thicker films are more likely to recombine rather than being collected[17].

Thickness-dependent external quantum efficiency (EQE) spectra have been measured and are shown in Fig. 2a, with the integrated current densities plotted in the inset. For a film thickness in the range of about 600 nm to about 2 μm, increasing the thickness improves the EQE, which should be due to the enhanced light harvesting and the better crystal quality of thick materials. In the roughly 2 μm to 5 μm range, even though the crystal quality is still improved, the carrier collection efficiency becomes the dominant limiting factor, and the EQE decreases as the thickness increases. Current density–voltage (J–V) measurements under 1-sun illumination of single-crystal $MAPbI_3$-based photovoltaic devices in Fig. 2b show a similar trend. When the single-crystal absorber thickness is below 2 μm, increasing the single-crystal absorber thickness can enhance the light absorption and therefore the current density. When the single-crystal absorber thickness is above 2 μm, the light absorption saturates (Supplementary Fig. 14). Further increasing the single-crystal absorber thickness will reduce only the fill factor (FF) and the open-circuit voltage (V_{OC}) (inset of Fig. 2b), which is due to the strong interfacial charge accumulation caused by the weaker build-in field in the thicker films. Note that in Fig. 2b, the source of the V_{OC} data for the J–V curves is different from that of the V_{OC} data in the inset. The inset data are from in situ-fabricated devices with untransferred single-crystal films, where any possible confounding factors from transfer steps besides the thickness can be minimized (Supplementary Discussion 6 and Supplementary Fig. 15).

We plot the slope of the J–V curve near the high-internal-field region (that is, the short-circuit current condition) and the low-internal-field region (that is, the V_{OC} condition) as a function of the absorber thickness (Fig. 2c). Owing to the small contributions from extrinsic resistance (Supplementary Fig. 16), the slopes near these two regions can serve as an indication of charge collection efficiency[18]. Ideally, a steep slope near the low-internal-field region and a close-to-zero slope near the high-internal-field region represent fast carrier transport and efficient charge collection. We find that devices with

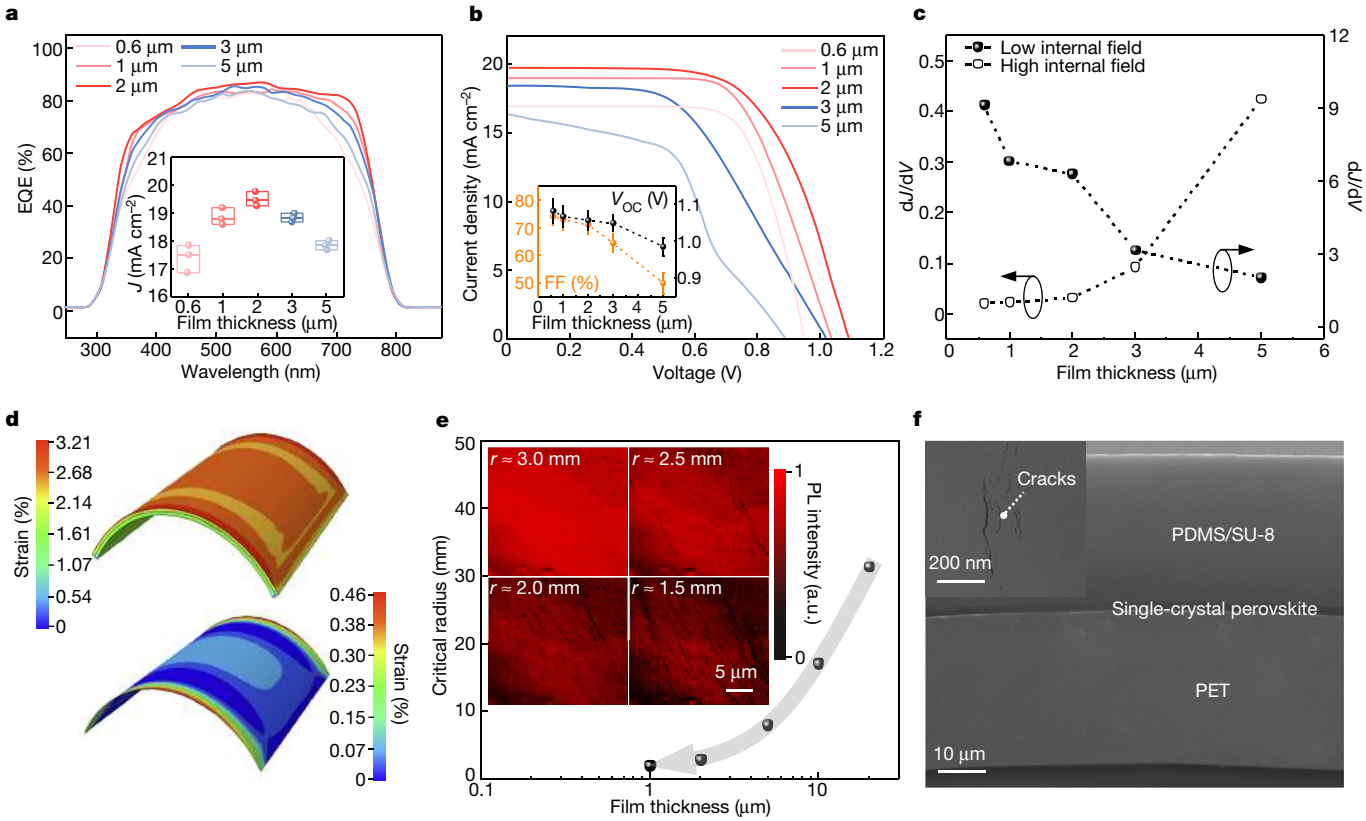

Fig. 2 | Thickness-dependent carrier transport and mechanical properties of the single-crystal hybrid perovskite. a, EQE measurements of the single-crystal hybrid perovskite with different thicknesses. Efficiency loss is observed when the film is either too thin or too thick, due to insufficient absorption or carrier collection, respectively. Inset: the integrated current density from the EQE measurements. Each box contains three data points with a maximum value (top line), a mean value (middle line) and a minimum value (bottom line). The efficiency loss leads to a low short-circuit current density (J_{sc}). **b**, J–V measurements of single-crystal $MAPbI_3$ photovoltaics with different absorber thicknesses fabricated using this growth-and-transfer method. The inset shows a decrease in both FF and V_{oc} with increasing absorber thickness; specifically, the inset V_{oc} results come from in situ devices. The error bars show the range from three measurements. **c**, J–V slopes at the low and high internal fields with different absorber thicknesses. Increasing the absorber thickness will cause a field-dependent charge collection at both the V_{oc} and J_{sc} regions. **d**, Finite element analysis of the single-crystal perovskite thin film with an NMP design at a bending radius of 2.5 mm. The top image shows the strain distribution in the entire sandwich structure, where the bending strain mostly occurs in the PET and SU-8/PDMS layers. The bottom image shows the strain distribution in the sandwiched single-crystal perovskite layer with all other layers hidden, where the maximum strain in the single-crystal perovskite layer is around 0.36%. **e**, Flexibility test results of the NMP design with different single-crystal perovskite film thicknesses. A smaller thickness leads to a smaller bending radius, which shows the remarkable flexibility of these brittle crystals. Inset: PL images show morphologies and cracks of the film at different bending radii. **f**, SEM images at a bending radius of about 2.5 mm, showing the relative thickness of different layers in the NMP design. The inset shows a magnified cross-section of the single-crystal $MAPbI_3$, illustrating the onset of fracture.

a thickness of 600 nm to 2 μm present efficient charge extraction: further increasing the film thickness will reduce the net field across the film. Therefore, the collection has to rely more on the carrier self-diffusion rather than field-driven drifting, where any potential barriers from trap states will substantially decrease the collection efficiency. Consideration of all the factors discussed leads to the conclusion that the optimal thickness for the single-crystal $MAPbI_3$ thin film used in this study is about 2 μm (see Supplementary Table 1 for more details).

Controlling the thickness of a single-crystal hybrid perovskite thin film can also tailor its mechanical properties. For a general material:

$$\sigma_{st} \propto \frac{Eh}{2r}$$

where σ_{st} is the maximum stress of the material, E is the Young's modulus, h is the thickness and r is the bending radius. Reducing the material thickness offers clear benefits in flexibility. Further enhancement of the device integrity can be achieved by placing the film on the neutral mechanical plane (NMP) (Supplementary Discussion 7), and the minimal bending radius for a roughly 2-μm-thick single-crystal film can reach about 2.5 mm (Extended Data Fig. 5).

Figure 2d shows the simulated strain distribution (maximum principal logarithmic strain) in a polyethylene terephthalate (PET)–$MAPbI_3$–SU-8/polydimethylsiloxane (PDMS) sandwich (top) as well as only the perovskite layer extracted from the NMP (bottom) when they are bent at a radius of 2.5 mm (see Supplementary Fig. 17 for other bending radii). The maximum principal strain in the majority of the single-crystal $MAPbI_3$ is less than 0.25%; the largest value occurs near the edge due to Poisson effects with a value of about 0.36%, which is close to the fracture strain of this material[19]. Mechanical tests clearly show the outstanding flexibility of single-crystal $MAPbI_3$ thin films under the NMP design (Fig. 2e; see Supplementary Fig. 18 for details). PL mapping of a roughly 2-μm-thick single-crystal $MAPbI_3$ with the NMP design under different bending radii shows that cracks begin to appear when the bending radius reaches about 2.5 mm (Fig. 2e, inset). Corresponding cross-sectional SEM images also show the onset of fractures at a bending radius of about 2.5 mm (Fig. 2f). The onset of the fractures is further confirmed by the I–V measurements under different bending radii (Supplementary Fig. 19), demonstrating the excellent flexibility and agreement with the simulations.

By feeding a continuous flow of precursors of different compositions (Extended Data Fig. 6; see Methods and Supplementary Discussion 1

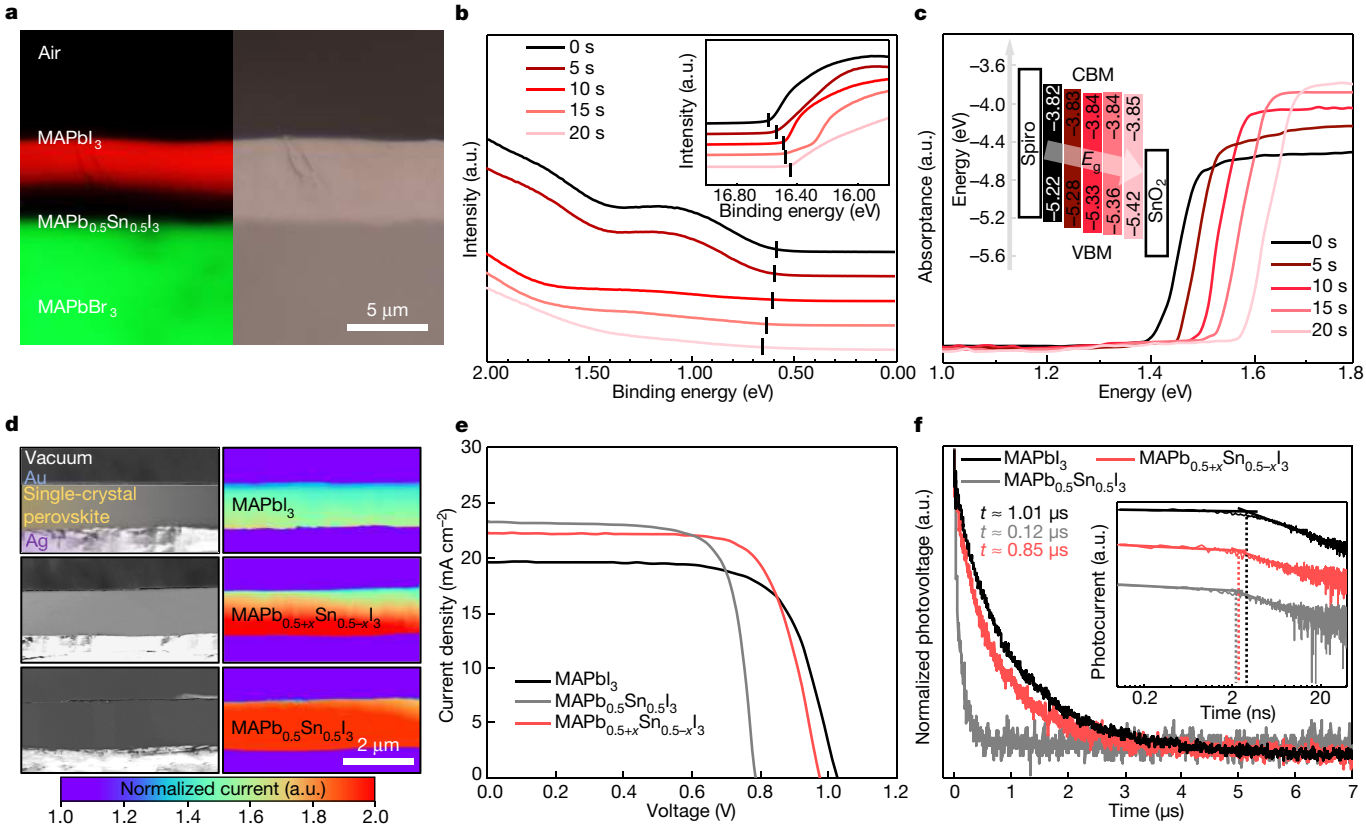

Fig. 3 | Bandgap-graded single-crystal perovskite thin films. a, A PL image (left) of the graded single-crystal $MAPb_{0.5+x}Sn_{0.5-x}I_3$ grown on a $MAPbBr_3$ substrate. $MAPbBr_3$ is chosen here as a representative example to show the compatibility of this growth-and-transfer method in the perovskite family. The dark tin-rich area is because of the infrared emission of the tin-alloyed $MAPbI_3$ being invisible on the camera. The contrast has been enhanced to better show the colour difference. A corresponding optical image (right) shows the graded $MAPb_{0.5+x}Sn_{0.5-x}I_3$ without noticeable structural interfaces. **b**, UPS measurements of samples at different growth times during the alloyed growth process: the bottom being $MAPb_{0.5}Sn_{0.5}I_3$ and the top being $MAPbI_3$. Inset: the VBM position is calculated from the low-binding-energy cut-off and the high-binding-energy cut-off, marked by the black vertical lines. **c**, UV–vis spectroscopy absorption of single-crystal thin films with the same composition as the surface composition of the graded structure at different growth times. Replacing tin with lead in the perovskite increases the bandgap. Inset: schematic showing the energy diagram based on calculations using the UPS and UV–vis data. E_g, bandgap energy; Spiro, the hole transport layer 2,2′,7,7′-tetrakis-9,9′-spirobifluorene (spiro-MeOTAD). **d**, SEM images and corresponding EBIC mapping of cross-sections of three different single-crystal perovskites: $MAPbI_3$ (top), graded $MAPb_{0.5+x}Sn_{0.5-x}I_3$ (middle) and $MAPb_{0.5}Sn_{0.5}I_3$ (bottom). The EBIC results show uniform current intensities for $MAPbI_3$ and $MAPb_{0.5}Sn_{0.5}I_3$ and a gradient current intensity for graded $MAPb_{0.5+x}Sn_{0.5-x}I_3$. **e**, Representative J–V curves of $MAPbI_3$, $MAPb_{0.5}Sn_{0.5}I_3$ and graded $MAPb_{0.5+x}Sn_{0.5-x}I_3$ single-crystal photovoltaic devices. The $MAPb_{0.5+x}Sn_{0.5-x}I_3$ single-crystal photovoltaic device shows the best performance among the three, due to the enhanced J_{SC} and relatively high V_{OC}. **f**, Transient photovoltage measurements show that the graded single-crystal $MAPb_{0.5+x}Sn_{0.5-x}I_3$ shows a relatively long carrier lifetime due to the easier exciton separation and charged carrier collection facilitated by the graded bandgap. Inset: ToF measurements show that the carrier mobility in graded single-crystal $MAPb_{0.5+x}Sn_{0.5-x}I_3$ is close to that in the compositionally uniform single-crystal $MAPb_{0.5}Sn_{0.5}I_3$. The inflection points of the photocurrent curves are marked by the dotted lines.

for more details), bandgap-graded single-crystal hybrid perovskite thin films can be achieved. $MAPb_{0.5}Sn_{0.5}I_3$ is chosen as the upper limit of the tin alloying concentration in this study. The resulting graded bandgap, gradually transitioning from $MAPb_{0.5}Sn_{0.5}I_3$ to $MAPbI_3$, is evidenced by the clear red–infrared interface in the PL image (Fig. 3a, left, and Supplementary Fig. 20). The bandgap-graded single crystal is stable without noticeable lead ion or tin ion migration or change in concentration gradient driven under an electrical field (Supplementary Fig. 21). Note that unlike conventional heterojunctions, no structural interface exists in the graded layer (Fig. 3a, right). The trap density in the graded single crystal is comparable to that of a pure $MAPbI_3$ single crystal (Supplementary Fig. 13c) and almost two orders of magnitude lower than that of a heterojunction with an abrupt interface (Supplementary Fig. 22).

We combine ultraviolet photoelectron spectroscopy (UPS) and ultraviolet–visible spectroscopy (UV–vis) to characterize the energy band structure of the graded single crystal in the growth process (Supplementary Discussion 8 and Supplementary Fig. 23). The UPS data show that the valence band maximum (VBM) position becomes lower (Fig. 3b) and the UV–vis results reveal that the bandgap becomes larger (Fig. 3c) as the growth continues. The summarized band structure of the $MAPb_{0.5+x}Sn_{0.5-x}I_3$ graded single-crystal is presented by the inset schematics in Fig. 3c. As the growth progresses and more lead is incorporated into the crystal, the position of the VBM becomes lower, and the position of the conduction band minimum (CBM) also becomes lower, but not as dramatically as the VBM. The changes in VBM and CBM result in a gradually increasing bandgap from the bottom ($MAPb_{0.5}Sn_{0.5}I_3$) to the surface ($MAPbI_3$), and the band structure of $MAPb_{0.5+x}Sn_{0.5-x}I_3$ is also supported by first-principles calculations (Extended Data Fig. 7 and Supplementary Discussion 9).

Figure 3d shows electron-beam-induced current (EBIC) mapping results along the cross-sections of three different single crystals. The compositionally uniform $MAPb_{0.5}Sn_{0.5}I_3$ (Fig. 3d, bottom) generates a higher current than the compositionally uniform $MAPbI_3$ (Fig. 3d, top), indicating easier exciton formation, charge dissociation and charge collection in $MAPb_{0.5}Sn_{0.5}I_3$ owing to its lower bandgap and weaker exciton binding[20]. The graded $MAPb_{0.5+x}Sn_{0.5-x}I_3$ (Fig. 3d, middle) shows a gradually decreasing

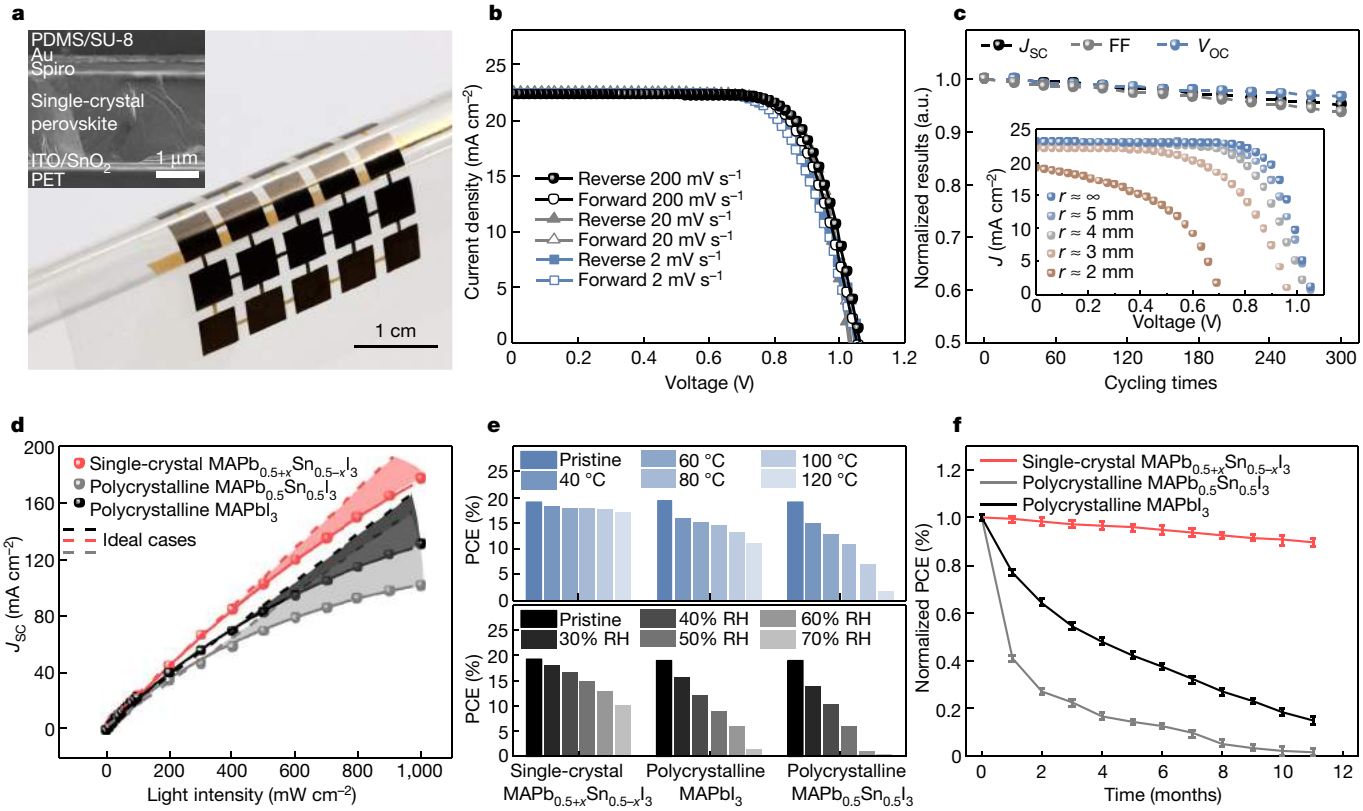

Fig. 4 | Flexible bandgap-graded single-crystal perovskite photovoltaics. **a**, An optical image showing an array of flexible single-crystal photovoltaic islands with a total working area of 6.25 cm^2 (0.5 cm × 0.5 cm × 25). Inset: a cross-sectional SEM image of the single-crystal perovskite photovoltaic device. **b**, Negligible *J*–*V* hysteresis in the graded single-crystal $MAPb_{0.5+x}Sn_{0.5-x}I_3$ photovoltaic devices. **c**, Cycling test results of the graded photovoltaic device at $r \approx 5$ mm. Inset: *J*–*V* curves at different bending radii. **d**, J_{SC} as a function of illumination intensity for graded single-crystal $MAPb_{0.5+x}Sn_{0.5-x}I_3$, polycrystalline $MAPb_{0.5}Sn_{0.5}I_3$, and polycrystalline $MAPbI_3$ photovoltaic devices. The polycrystalline devices tend to deviate from a linear relationship at higher intensities due to degradation in the absorber. The degree of dispersion is reflected by the shaded regions. **e**, Thermal and humidity stability test results of the graded single-crystal $MAPb_{0.5+x}Sn_{0.5-x}I_3$, polycrystalline $MAPb_{0.5}Sn_{0.5}I_3$ and polycrystalline $MAPbI_3$. Unencapsulated devices are used in only the humidity stability test. The ageing times for the thermal and humidity stability tests are 2 h and 30 min, respectively. RH, relative humidity. **f**, Long-term shelf-stability test results (over 11 months) of the graded single-crystal $MAPb_{0.5+x}Sn_{0.5-x}I_3$, polycrystalline $MAPb_{0.5}Sn_{0.5}I_3$ and polycrystalline $MAPbI_3$ photovoltaic devices in a dark dry box. A top SU-8/PDMS layer also covered the polycrystalline photovoltaic devices to maintain the same encapsulation. The single-crystal photovoltaic devices show much better stability in terms of PCE than their polycrystalline counterparts. Error bars show the range from three measurements with different aperture positions.

current when the tin content is reduced from 50% at the bottom to 0% at the surface. Any possible contribution from the top gold electrode that may have introduced a higher recombination rate has been excluded (Supplementary Fig. 24). EQE measurements show the median average current density in the graded absorber compared with $MAPbI_3$ and $MAPb_{0.5}Sn_{0.5}I_3$, indicating the existence of an engineered bandgap (Supplementary Fig. 25). *J*–*V* measurements reveal the overall performance of these three different absorbers (Fig. 3e). Both the $MAPb_{0.5}Sn_{0.5}I_3$ and the graded $MAPb_{0.5+x}Sn_{0.5-x}I_3$ absorbers give a higher short-circuit current density (J_{SC}) than $MAPbI_3$, as alloying tin with the lead decreases the bandgap and the exciton binding energy. However, $MAPb_{0.5}Sn_{0.5}I_3$ shows a much lower V_{OC} compared with $MAPbI_3$, because of its higher defect concentrations, shorter carrier lifetimes and lower bandgap. Surprisingly, the graded $MAPb_{0.5+x}Sn_{0.5-x}I_3$ gives a relatively high V_{OC} and has the best overall performance among the three absorbers (Supplementary Fig. 26).

We combine calculations and experiments to understand the high V_{OC} of the graded $MAPb_{0.5+x}Sn_{0.5-x}I_3$. The calculation results show a decrease in carrier effective mass (for both electrons and holes) when more tin is incorporated into lead perovskites (Extended Data Fig. 7). ToF results show that the carrier mobility in the graded $MAPb_{0.5+x}Sn_{0.5-x}I_3$ is on par with that in $MAPb_{0.5}Sn_{0.5}I_3$ (Fig. 3f, inset). However, transient photovoltage measurements show that the carrier lifetime in the graded structure is much higher than that in $MAPb_{0.5}Sn_{0.5}I_3$ (Fig. 3f), contradictory to our understanding that adding tin into lead perovskites normally results in a lower carrier lifetime because of the high recombination rate in tin perovskites[21,22]. We ascribe the measured high carrier lifetime in the $MAPb_{0.5+x}Sn_{0.5-x}I_3$ to its graded bandgap, which is similar to the built-in field of a p–n junction. The graded bandgap of the $MAPb_{0.5+x}Sn_{0.5-x}I_3$ facilitates the carrier separation, transport and collection with an extended carrier lifetime (Supplementary Discussion 10 and Supplementary Fig. 27)[23,24], resulting in a relatively high V_{OC}.

We integrate the single-crystal thin films in various devices. Single-crystal perovskite light-emitting diodes have been demonstrated using this growth-and-transfer method (Extended Data Fig. 8). The pixel size can range from 1 μm to 100 μm, with potential applications for flexible displays with tunable colour, high resolution, high stability and high quantum efficiency. Furthermore, this growth-and-transfer method allows the engineering of the material morphology and orientation[13]. A textured anti-reflective single-crystal perovskite photodetector shows improved performances over one with a flat surface (Extended Data Fig. 8). The focus of this study is photovoltaic devices. Shown in Fig. 4a is a flexible array of photovoltaic devices in an island-bridge layout[25], with each island a single-crystal perovskite photovoltaic device interconnected by the metallic bridges. The corresponding cross-sectional structure of an island is illustrated in the inset of Fig. 4a. The mode value of power conversion efficiency (PCE) of a 0.5 cm × 0.5 cm island under a 3 mm × 3 mm mask is 15–17% for single-crystal $MAPbI_3$, and 17–19% for graded single-crystal $MAPb_{0.5+x}Sn_{0.5-x}I_3$ (Supplementary Fig. 26).

The highest PCE that has been measured is 20.04% under the initial reverse scanning. To further improve the single-crystal device performance, surface/interface passivation and strategic layer design are needed. Most devices show negligible J–V hysteresis at different scan rates and directions (Fig. 4b). The entire array of graded single-crystal $MAPb_{0.5+x}Sn_{0.5-x}I_3$ photovoltaics shows an overall PCE of about 10.3% with a working area of about 9 cm^2 (Supplementary Fig. 28).

In mechanical testing, the flexible photovoltaic device undergoes bending–straightening cycles. The islands in the middle of the array experience the most bending (Supplementary Fig. 29) and are therefore selected to demonstrate the mechanical stability of the entire array (Fig. 4c; see Supplementary Fig. 30 for the other islands). At $r \approx 5$ mm, a small decrease in V_{OC} (from 100% to 96.5%) and J_{SC} (from 100% to 94.9%), and a decay in FF (from 100% to 93.7%) are observed after a 300-time cycle. The decrease may be due to the increase in series resistance caused by the interfacial delamination. Further decreasing r causes a substantial drop in V_{OC}, J_{SC} and FF, which possibly results from the material failure (for example, cracks in the absorber) (Fig. 4c, inset). Polycrystalline photovoltaics of the same device configuration show substantial performance degradation under the same cyclic bending tests (Supplementary Fig. 31), which may be caused by the fast material and device degradation at the grain boundaries during bending (Supplementary Discussion 11 and Supplementary Fig. 32)[26,27].

Stress-stability test results, in which the J_{SC} is measured as a function of light intensity, are presented in Fig. 4d. Owing to the lack of a way to realize lead–tin composition gradients in the polycrystalline structure without junction formation, only $MAPb_{0.5}Sn_{0.5}I_3$ and $MAPbI_3$ have been fabricated in polycrystalline photovoltaics for comparison (Supplementary Discussion 12). The relationship between J_{SC} and light intensity for the graded single-crystal $MAPb_{0.5+x}Sn_{0.5-x}I_3$ photovoltaics is close to linear, indicating good charge collection[28]. Single-crystal photovoltaics of graded $MAPb_{0.5+x}Sn_{0.5-x}I_3$, $MAPb_{0.5}Sn_{0.5}I_3$ and $MAPbI_3$ show similar stress stability (Supplementary Fig. 33). However, the J_{SC}–light intensity curves for polycrystalline $MAPb_{0.5}Sn_{0.5}I_3$ and $MAPbI_3$ photovoltaics tend to deviate from the linear relationship at higher light intensities, probably due to degradation facilitated by the presence of grain boundaries.

Figure 4e shows single-crystal photovoltaic devices have better stability than polycrystalline devices under different thermal and humidity conditions (see Supplementary Discussion 12 for the humidity control, and Supplementary Fig. 34 for additional humidity and thermal stability comparisons). Thermogravimetric analysis confirms that the single-crystal film decomposes at a higher temperature than the polycrystalline film (Supplementary Fig. 35). In situ X-ray photoelectron spectroscopy (XPS) results reveal that degradation factors (for example, pinholes and grain boundaries) in the polycrystalline structure facilitate oxygen and moisture diffusion, leading to a rapid oxidization of Sn^{2+} and overall degradation rate[22,29,30] (Extended Data Fig. 9). Besides, single-crystal devices show a slower decay than polycrystalline devices with the same measurement conditions and encapsulation in 1,000-h continuous illumination stability tests under 1-sun intensity by tracking the maximum power point[31,32] (Extended Data Fig. 10). Such a difference is attributed to the suppressed ion migration and the intrinsic slow self-doping effect in the single crystals (Supplementary Discussions 13 and 14). In addition, to manifest the difference in the single-crystal and polycrystalline perovskites, we replace the thermal/light sensitive 2,2′,7,7′-tetrakis-9,9′-spirobifluorene (spiro-MeOTAD) with the more stable poly(bis(4-phenyl)(2,4,6-trimethylphenyl)amine)[32]. The stability differences among those devices become even more pronounced (Supplementary Fig. 36). Finally, long-term shelf-stability studies (Fig. 4f and Supplementary Fig. 37) further prove that single-crystal devices have much better stability than their polycrystalline counterparts regardless of the composition (Supplementary Discussion 14 and Supplementary Figs. 38–41).

Online content

Any methods, additional references, Nature Research reporting summaries, source data, extended data, supplementary information, acknowledgements, peer review information; details of author contributions and competing interests; and statements of data and code availability are available at https://doi.org/10.1038/s41586-020-2526-z.

1. Yang, W. S. et al. Iodide management in formamidinium-lead-halide-based perovskite layers for efficient solar cells. *Science* **356**, 1376–1379 (2017).
2. Lin, K. et al. Perovskite light-emitting diodes with external quantum efficiency exceeding 20 per cent. *Nature* **562**, 245–248 (2018).
3. Feng, J. et al. Single-crystalline layered metal-halide perovskite nanowires for ultrasensitive photodetectors. *Nat. Electron.* **1**, 404–410 (2018).
4. National Renewable Energy Laboratory. *Best Research-Cell Efficiency Chart* https://www.nrel.gov/pv/cell-efficiency.html (NREL, US Department of Energy, 2020).
5. Wang, Q. et al. Large fill-factor bilayer iodine perovskite solar cells fabricated by a low-temperature solution-process. *Energy Environ. Sci.* **7**, 2359–2365 (2014).
6. Liu, Z. et al. Gas–solid reaction based over one-micrometer-thick stable perovskite films for efficient solar cells and modules. *Nat. Commun.* **9**, 3880 (2018).
7. Jiang, Q. et al. Surface passivation of perovskite film for efficient solar cells. *Nat. Photon.* **13**, 460–466 (2019); correction **13**, 500 (2019).
8. Leblebici, S. Y. et al. Facet-dependent photovoltaic efficiency variations in single grains of hybrid halide perovskite. *Nat. Energy* **1**, 16093 (2016).
9. Zhang, W. et al. Enhanced optoelectronic quality of perovskite thin films with hypophosphorous acid for planar heterojunction solar cells. *Nat. Commun.* **6**, 10030 (2015).
10. Zheng, G. et al. Manipulation of facet orientation in hybrid perovskite polycrystalline films by cation cascade. *Nat. Commun.* **9**, 2793 (2018).
11. Chen, Z. et al. Thin single-crystal perovskite solar cells to harvest below-bandgap light absorption. *Nat. Commun.* **8**, 1890 (2017).
12. Lee, L. et al. Wafer-scale single-crystal perovskite patterned thin films based on geometrically-confined lateral crystal growth. *Nat. Commun.* **8**, 15882 (2017).
13. Lei, Y. et al. Controlled homoepitaxial growth of hybrid perovskites. *Adv. Mater.* **30**, 1705992 (2018).
14. Chen, Y. et al. Strain engineering and epitaxial stabilization of halide perovskites. *Nature* **577**, 209–215 (2020).
15. Zou, W. et al. Minimising efficiency roll-off in high-brightness perovskite light-emitting diodes. *Nat. Commun.* **9**, 608 (2018).
16. Richter, J. M. et al. Enhancing photoluminescence yields in lead halide perovskites by photon recycling and light out-coupling. *Nat. Commun.* **7**, 13941 (2016).
17. Gong, X. et al. Contactless measurements of photocarrier transport properties in perovskite single crystals. *Nat. Commun.* **10**, 1591 (2019).
18. Tsai, H. et al. Design principles for electronic charge transport in solution-processed vertically stacked 2D perovskite quantum wells. *Nat. Commun.* **9**, 2130 (2018).
19. Ćirić, L. et al. Mechanical response of $CH_3NH_3PbI_3$ nanowires. *Appl. Phys. Lett.* **112**, 111901 (2018).
20. Bokdam, M. et al. Role of polar phonons in the photo excited state of metal halide perovskites. *Sci. Rep.* **6**, 28618 (2016).
21. Noel, N. K. et al. Lead-free organic-inorganic tin halide perovskites for photovoltaic applications. *Energy Environ. Sci.* **7**, 3061–3068 (2014).
22. Tong, J. et al. Carrier lifetimes of >1 μs in Sn-Pb perovskites enable efficient all-perovskite tandem solar cells. *Science* **364**, 475–479 (2019).
23. Dullweber, T., Rau, U. & Schock, H. A new approach to high-efficiency solar cells by band gap grading in Cu(In, Ga)Se_2 chalcopyrite semiconductors. *Sol. Energy Mater. Sol. Cells* **67**, 145–150 (2001).
24. Hutchby, J. A. & Fudurich, R. L. Theoretical analysis of $Al_xGa_{1-x}As$-GaAs graded band-gap solar cell. *J. Appl. Phys.* **47**, 3140–3151 (1976).
25. Wang, C., Wang, C., Huang, Z. & Xu, S. Materials and structures toward soft electronics. *Adv. Mater.* **30**, 1801368 (2018).
26. Wang, S., Jiang, Y., Juarez-Perez, E. J., Ono, L. K. & Qi, Y. Accelerated degradation of methylammonium lead iodide perovskites induced by exposure to iodine vapour. *Nat. Energy* **2**, 16195 (2017).
27. Yun, J. S. et al. Humidity-induced degradation via grain boundaries of $HC(NH_2)_2PbI_3$ planar perovskite solar cells. *Adv. Funct. Mater.* **28**, 1705363 (2018).
28. Tsai, H. et al. Light-induced lattice expansion leads to high-efficiency perovskite solar cells. *Science* **360**, 67–70 (2018).
29. Ke, W. & Kanatzidis, M. G. Prospects for low-toxicity lead-free perovskite solar cells. *Nat. Commun.* **10**, 965 (2019).
30. Chen, M. et al. Highly stable and efficient all-inorganic lead-free perovskite solar cells with native-oxide passivation. *Nat. Commun.* **10**, 16 (2019).
31. Domanski, K., Alharbi, E. A., Hagfeldt, A., Grätzel, M. & Tress, W. Systematic investigation of the impact of operation conditions on the degradation behaviour of perovskite solar cells. *Nat. Energy* **3**, 61–67 (2018).
32. Ono, L. K., Qi, Y. & Liu, S. F. Progress toward stable lead halide perovskite solar cells. *Joule* **2**, 1961–1990 (2018).
33. Liu, M., Jing, D., Zhou, Z. & Guo, L. Twin-induced one-dimensional homojunctions yield high quantum efficiency for solar hydrogen generation. *Nat. Commun.* **4**, 2278 (2013).

Methods

Materials

The materials used in this study were purchased for direct use without further purification, which include lead iodide (PbI_2, 99.99%, Tokyo Chemical Industry), methylammonium iodide (MAI, 99.9%, Greatcell Solar), tin iodide (SnI_2, anhydrous 99.99%, Sigma Aldrich), tin(II) chloride dihydrate ($SnCl_2{\cdot}2H_2O$, 98%, Sigma Aldrich), spiro-MeOTAD (LT-S922, Luminescence Technology), 4-tert-butylpyridine (Sigma Aldrich), bis(trifluoromethylsulfonyl)amine lithium salt (Sigma Aldrich), chlorobenzene (TCI America), anhydrous acetonitrile (99.8%, Sigma Aldrich), anhydrous ethanol (Sigma Aldrich), anhydrous dimethylformamide (DMF, 99.8%, Sigma Aldrich), anhydrous gamma-butyrolactone (Sigma Aldrich), indium tin oxide-coated polyethylene terephthalate (PET/ITO, Zhuhai Kaivo Optoelectronic Technology, Visiontek Systems), poly(pyromellitic dianhydride-co-4,4′-oxydianiline) (polyimide precursor, Sigma Aldrich), 1-methoxy-2-propanol acetate (SU-8, MicroChem) and polydimethylsiloxane (PDMS, monoglycidyl ether terminated, average molecular weight $M_n \approx 5{,}000$, Sigma Aldrich).

Device fabrication

Patterned ITO/PET substrates were first cleaned with water, acetone and isopropyl alcohol in an ultrasonication bath for 15 min, respectively. The substrates were then treated by oxygen plasma for 3 min before coating. The $SnCl_2$ solution (0.045 g $SnCl_2{\cdot}2H_2O$ in 2 ml of anhydrous ethanol) was spin-coated at 5,000 r.p.m. for 40 s followed by 2 h of 150 °C baking to serve as the electron transporting layer. The coated substrates were then used for single-crystal hybrid perovskite thin-film transfer in the lithography-assisted epitaxial-growth-and-transfer method (see Supplementary Discussion 1 for details). After all the transferring and etching steps, spiro-MeOTAD solution was spin-coated as the hole transporting layer at 3,500 r.p.m. for 30 s onto the ITO/SnO_2/single-crystal perovskite substrate. The obtained samples were loaded into a vacuum chamber for gold deposition. A mixture of SU-8 and PDMS was coated onto the gold layer for overnight curing. For the polycrystalline $MAPbI_3$ device fabrication, 0.2026 g of MAI and 0.5877 g of PbI_2 were dissolved into 1 ml of DMF/dimethyl sulfoxide (DMSO) solvent (DMF:DMSO = 19:1) to form a clear precursor solution. It has been found that the traditional 4:1 or 9:1 (refs. [34,35]) solvent ratio sometimes results in milky coloured films. Then 75 µl of the precursor was dropped on top of a prepared substrate (ITO/SnO_2) and the spin speed was set at 6,000 r.p.m. for 30 s. At the seventh second, 500 µl of diethyl ether was quickly dropped at the centre of the substrate. After spin coating, the substrate was transferred onto a hotplate (110 °C) for 5 min. A black $MAPbI_3$ polycrystal thin film was achieved. For $MAPb_xSn_{1-x}I_3$, MAI was fixed at 0.2026 g for all of the different compositions. The calculated amounts of SnI_2 and PbI_2 were dissolved into 1 ml of DMF/DMSO solvent (DMF:DMSO = 19:1) to form clear precursor solutions. Then 75 µl of precursor solution was dropped on top of a prepared substrate (ITO/SnO_2) and the spin speed was set at 6,000 r.p.m. for 30 s. At the tenth second, 500 µl of diethyl ether was quickly dropped at the centre of the substrate. After spin coating, the substrate was transferred on a hotplate (110 °C) for 5 min. A black $MAPb_xSn_{1-x}I_3$ polycrystal thin film was achieved. It is worth pointing out that if any cloudy or milky colour appears, the dropping of the antisolvent should be moved to a slightly earlier time.

Characterization

All SEM images were taken using a Zeiss Sigma 500 SEM. All optical images were taken using a Zeiss Axio Imager Optical Microscope. The XRD data were measured by a Rigaku 393 Smart lab diffractometer equipped with a Cu Kα1 radiation source (λ = 0.15406 nm) and a Ge 394 (220 × 2) monochromator. The TEM images were taken using an FEI 200 kV Sphera microscope. Samples for the TEM were prepared using a frozen focused ion beam (FEI Scios Dual Beam FIB/SEM). J–V measurements were carried out using a Keithley 2400 source meter under a simulated air mass of 1.5 irradiation (100 mW cm^{-2}) and a xenon-lamp-based solar simulator (Oriel LCS-100). The same shadow mask was used during the device measurement to avoid edge effects for small-area photovoltaic devices. A monocrystalline silicon photovoltaic device (Newport 532, ISO1599, calibrated by the National Institute of Standards and Technology) was used for light intensity calibration before all measurements. EQE data were collected by illuminating the device under monochromatic light using a tungsten source (chopped at 150 Hz) while collecting the photocurrent by a lock-in amplifier in the a.c. mode. The light source spectrum response was corrected by a calibrated silicon diode (FDS1010, Thorlab). Energy dispersive X-ray spectroscopy linear scanning was performed through a field emission environmental SEM (FEI/Phillips XL30 ESEM) system. The EBIC was collected using a FEI Scios Dual Beam microscope with a Mighty EBIC 2.0 controller (Ephemeron Labs) and a Femto DLPCA-200 preamplifier. For the cross-section configuration measurements, the thin single-crystal perovskite sample was pre-deposited with electrodes on two flat sides by electron-beam evaporation. Then, the sample was loaded onto the EBIC holder fixed by fast-dry silver epoxy. The acceleration voltage and current were 15 kV and 15 pA, respectively. The EBIC and SEM images of the same region of interest were collected simultaneously. UPS and XPS measurements were carried out on the surface of the epitaxial single-crystal perovskites films using Kratos AXIS Supra with a He I (21.22 eV) source under 10^{-8} torr chamber pressure. UV–vis and absorption spectra were collected using a Perkin Elmer Lambda 1050 UV–vis system under the reflection mode. Adhesion force tests and cycling bending tests were performed using an Instron Machine (5965 Dual Column Testing Systems) system. For cycling bending tests, a speed mode was used to fix the bending curvature of the device with an extrusion speed of 1 mm min^{-1}. Bending curvature mapping measurements were finished by an HDI Advance three-dimensional scanner (GOMEASURE3D). The devices were fixed onto a series of three-dimensional-printed plastic rods with designed radii to carry out the curvature mapping experiments. ToF was measured by the extraction time in the transient photocurrent to calculate the carrier mobility. An external bias of 0.5 V was used to power the devices with a resistor connected in series. Transient photovoltages were measured with an oscilloscope (Agilent MSO6104A Channel Mixed Signal). A pulsed laser with a pulse width of less than 10^{-10} s was used as the light source. PL and time-resolved PL measurements were performed with a confocal microscopy system focusing a monochromatic 6-ps-pulsed laser with a ×4 objective lens (numerical aperture 0.13) under 1-sun intensity. Samples were measured in a dark environment at room temperature. The trap density was measured using the space-charge limited current method by a Keithley 2400 source meter and a customized probe station in a dark environment. Devices were deposited with gold electrodes by electron-beam evaporation. Thermogravimetric analysis was conducted with a Netzsch STA 449 F1 Jupiter system. All samples were prepared on general glass slides without any other materials introduced. The temperature increase rate was kept at about 1 °C min^{-1} to avoid possible fluctuations.

Data availability

The data that support the findings of this study are available from the corresponding authors on reasonable request.

34. Ahn, N. et al. Highly reproducible perovskite solar cells with average efficiency of 18.3% and best efficiency of 19.7% fabricated via Lewis base adduct of lead (II) iodide. *J. Am. Chem. Soc.* **137**, 8696–8699 (2015).
35. Zhao, P. et al. Antisolvent with an ultrawide processing window for the one-step fabrication of efficient and large-area perovskite solar cells. *Adv. Mater.* **30**, 1802763 (2018).

Acknowledgements We thank S. Shrestha for discussions on the polycrystalline device fabrication, S. Wang for analysis and discussions on the UPS, Y. Wang for discussions on the

adhesion force measurement, J. Wu for analysis and discussion of the EBIC and S. Xiang for feedback on the manuscript preparation. This work was supported by the start-up fund by University of California San Diego. D.P.F. acknowledges California Energy Commission award no. EPC-16-050. The microfabrication involved in this work was in part performed at the San Diego Nanotechnology Infrastructure (SDNI) of UCSD, a member of the National Nanotechnology Coordinated Infrastructure, which was supported by the National Science Foundation (grant number ECCS-1542148). This characterization work was performed, in part, at the Center for Integrated Nanotechnologies, an Office of Science User Facility operated for the US Department of Energy (DOE) Office of Science by Los Alamos National Laboratory (contract 89233218CNA000001) and Sandia National Laboratories (contract DE-NA-0003525).

Author contributions S.X. and Y. Lei conceived the idea. Y. Lei and Y.C. contributed to the growth and transfer method. Y. Lei and Y.C. took the optical and SEM images. Y. Lei and R.Z. carried out the photovoltaic-related characterizations. Y. Lei carried out the EBIC measurements. R.Z. carried out the XRD characterizations. Yuheng Li and K.Y. carried out the DFT calculations. Q.Y. and J.L. contributed to the TEM and XPS characterizations. S.L. carried out the finite element analysis. Y. Lei, Y.Y., H.T., W.C., K.W., Y. Luo, D.P.F., S.A.D., J.Y., W.N. and Y.-H.L. contributed to the carrier dynamic measurement and analysis. Y. Lei, Y.C., Y.G. and Chunfeng Wang contributed to the device fabrication. Y. Lei, S.L., M.L. and M.P. contributed to the flexibility characterizations. X.Z. carried out the FDTD calculations. Y. Lei, Chonghe Wang, H.H., Yang Li, B.Q. and Z.Z. contributed to the schematics and photographs. All authors contributed to discussing the data and commenting on the manuscript.

Competing interests The authors declare no competing interests.

Additional information

Supplementary information is available for this paper at https://doi.org/10.1038/s41586-020-2526-z.

Correspondence and requests for materials should be addressed to S.X.

Peer review information *Nature* thanks Hyunhyub Ko and the other, anonymous, reviewer(s) for their contribution to the peer review of this work.

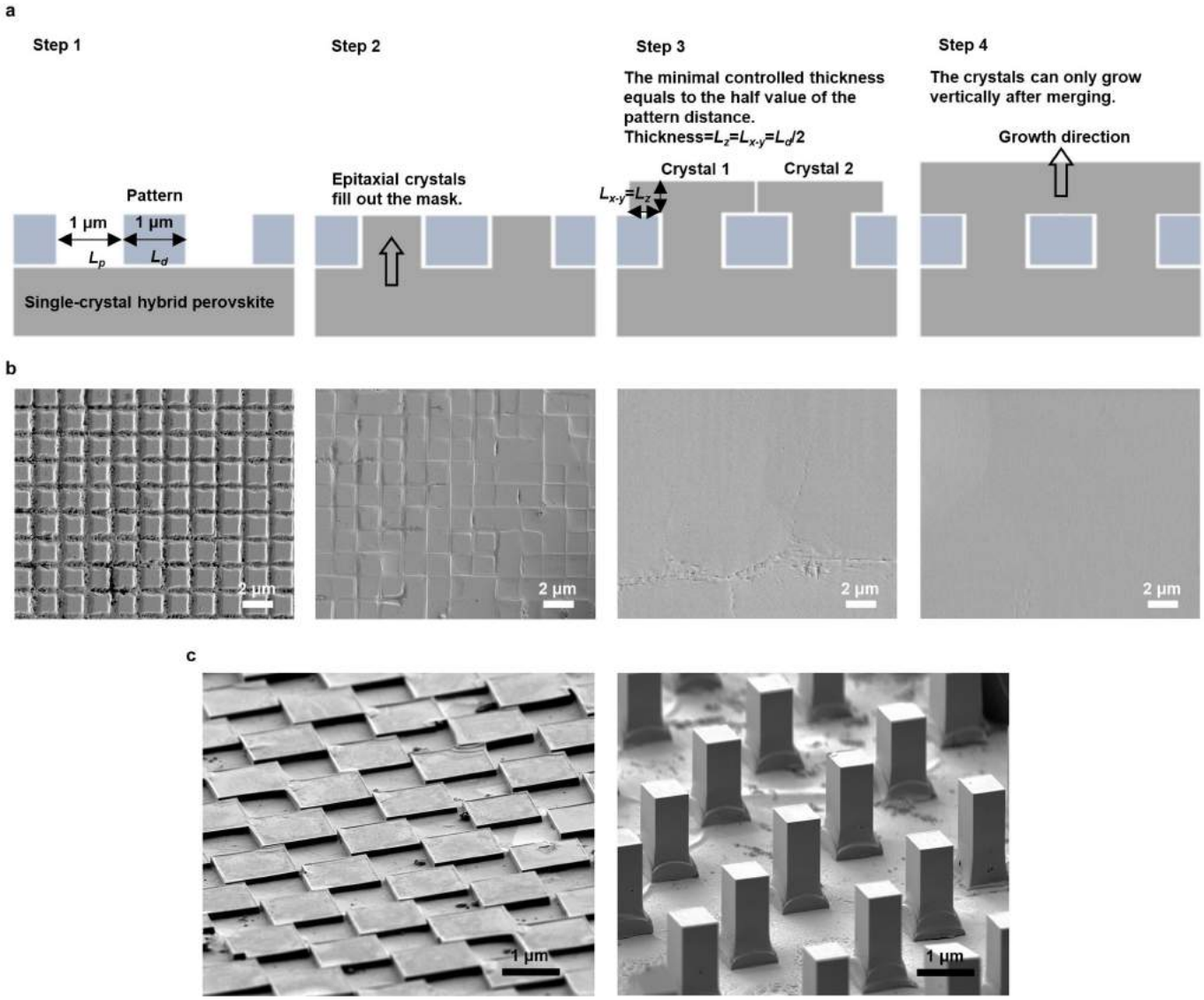

Extended Data Fig. 1 | The mechanism of the lithography-assisted epitaxial-growth-and-transfer method. a, Detailed schematic growth steps. L_p, pattern width; L_d, distance between two patterns; $L_{x\text{-}y}$, growth length in the x–y plane; L_z, growth length in the vertical z direction. **b**, Detailed epitaxial merging steps shown by SEM images (top view). First, individual single-crystals grow out of the mask. The lattice orientation of the epitaxial crystals is the same, which is controlled by the substrate. Then the individual crystals gradually expand and contact with each other. No lattice tilting or twisting can be found. Finally, completely merged single-crystal thin films are formed, where no grain boundaries can be seen. **c**, Titled SEM images of different growth behaviour under different growth temperatures and precursor concentrations. Low temperature and concentration can result in thin films (left), whereas high temperature and concentration lead to rods (right).

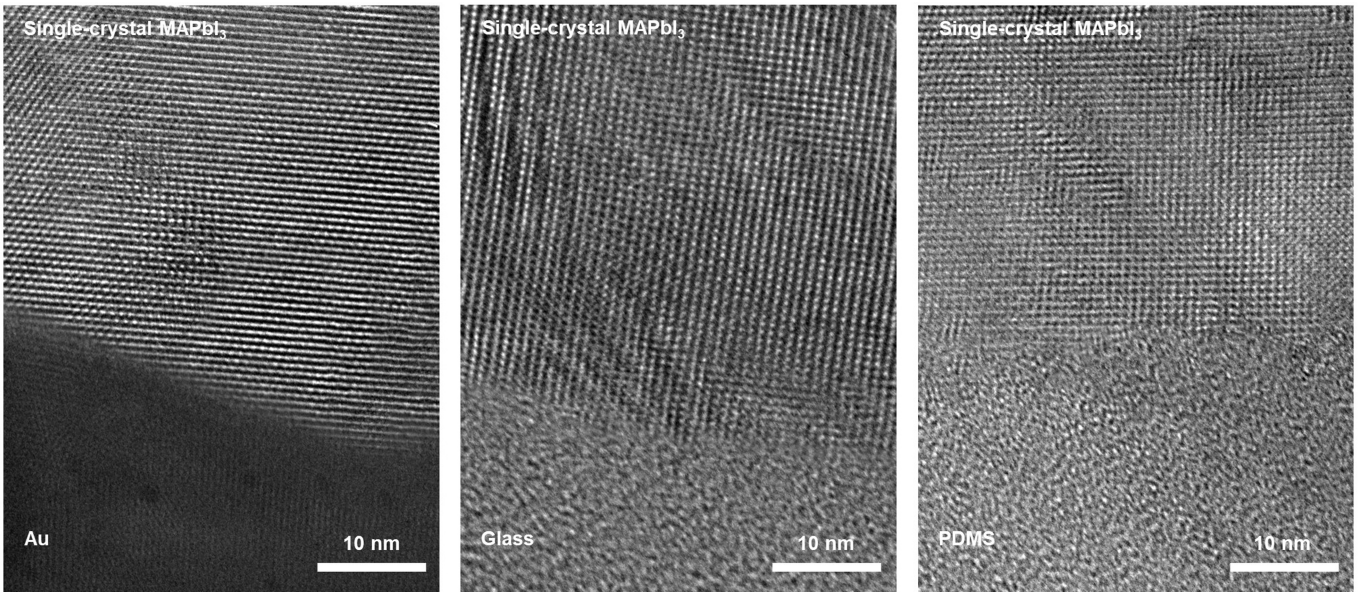

Extended Data Fig. 2 | Characterizations of interfacial crystal quality. High-resolution TEM studies of transferred single-crystal $MAPbI_3$ on different substrates (for example, gold for metals, glass for oxides and PDMS for polymers) using this growth-and-transfer method. The results show that there is no obvious lattice dislocation or polycrystalline structure formed at the interface, indicating that the re-adhesion/re-growth process maintains the single-crystal properties of the transferred materials.

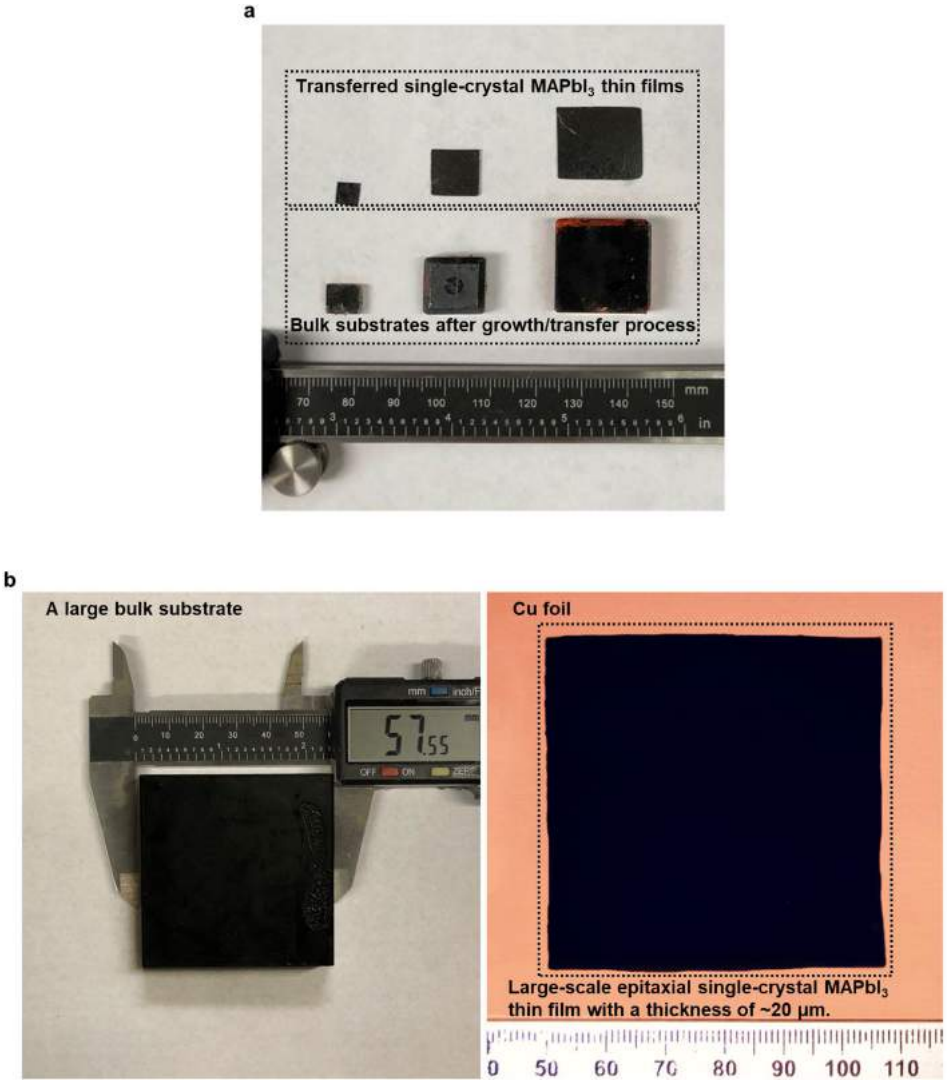

Extended Data Fig. 3 | Scaling up the fabrication method. a, Freestanding transferred single-crystal $MAPbI_3$ thin films fabricated by soft polymer masks and corresponding bulk substrates. **b**, A large bulk substrate (left) that is used to epitaxially grow the single-crystal $MAPbI_3$ thin film (left) and a transferred single-crystal $MAPbI_3$ thin film using a rigid copper foil (20 μm thick) as the mask (right).

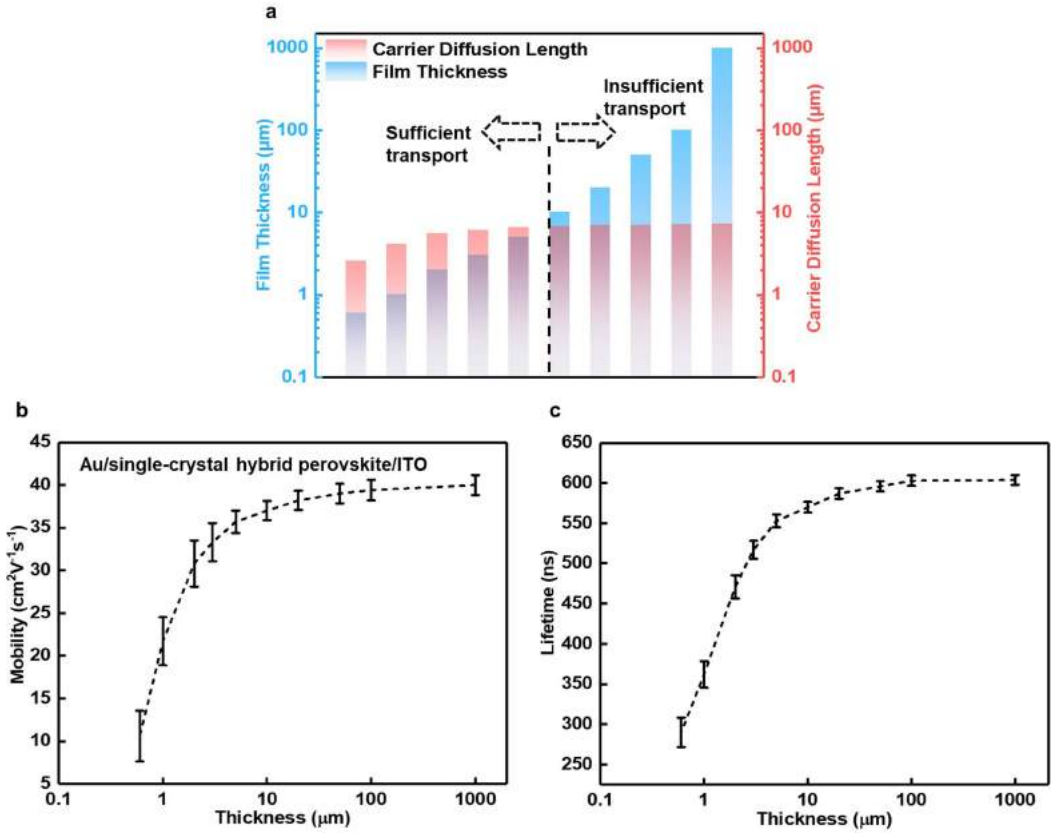

Extended Data Fig. 4 | Carrier diffusion length calculations. a–**c**, Carrier diffusion lengths (**a**) calculated from measured carrier mobilities (**b**) and carrier lifetimes (**c**) with different thicknesses of the single-crystal perovskite. Insufficient charge collection begins when the thickness goes beyond about 5 μm, which can result in a high recombination possibility in the absorber and thus a low device efficiency. Error bars come from three different measurements under the same condition.

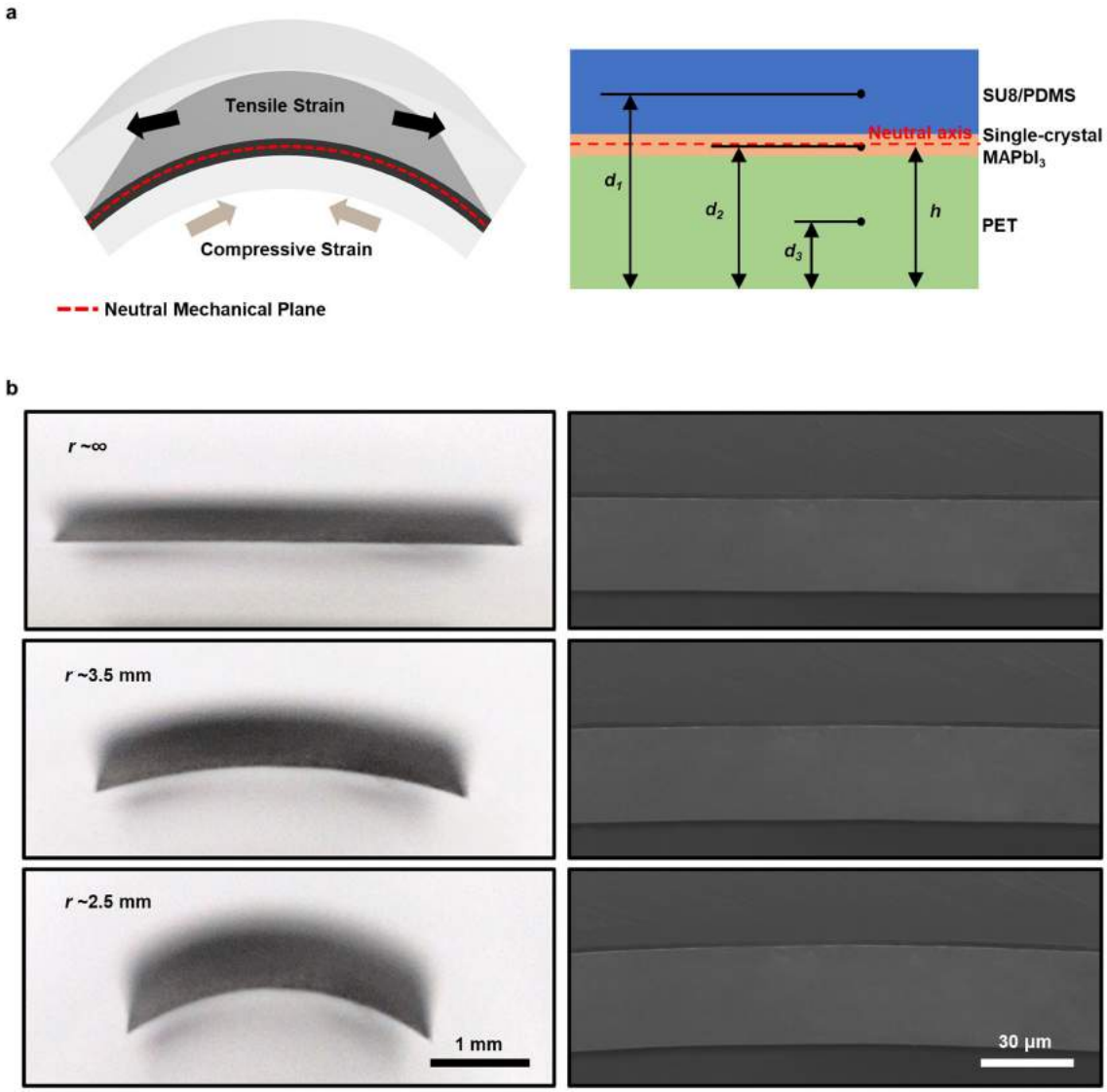

Extended Data Fig. 5 | The NMP design. a, Schematics for calculating the position of the NMP. The SU-8/PDMS top layer is critical for minimizing the strain in the single-crystal perovskite layer. **b**, Optical (left) and SEM (right) images under different bending conditions. The single-crystal perovskite (about 2 μm thick) can be successfully bent to $r \approx 2.5$ mm. All optical images share the same scale bar. All SEM images share the same scale bar.

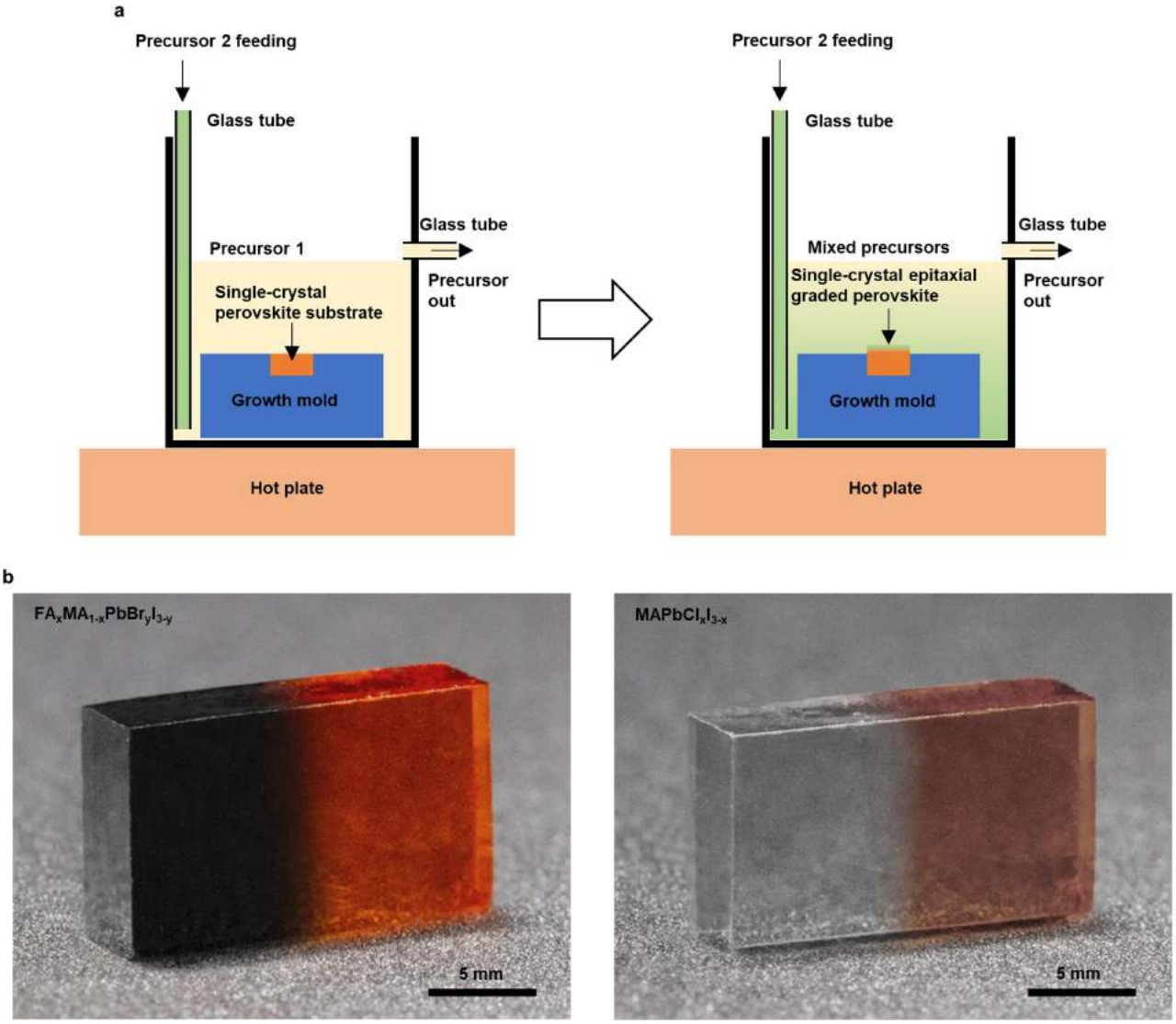

Extended Data Fig. 6 | The growth setup for the bandgap-graded single-crystal perovskites. a, Schematic growth processes with continuously exchanging the precursor solution, which allows the formation of the alloyed structure along the epitaxial growth direction. The perovskite substrate sits in a PDMS growth mould in precursor solution 1. A different precursor solution 2 is fed with designed rates (depending on the solution volume, a calculation example can be seen in Supplementary Discussion 1). **b**, Optical images showing two representative kinds of graded single-crystal perovskites. The alloyed region is at the interface (about 1 mm in width, depending on the alloying rate) between the different coloured crystals. Organic cations, inorganic atoms and halides can all be alloyed.

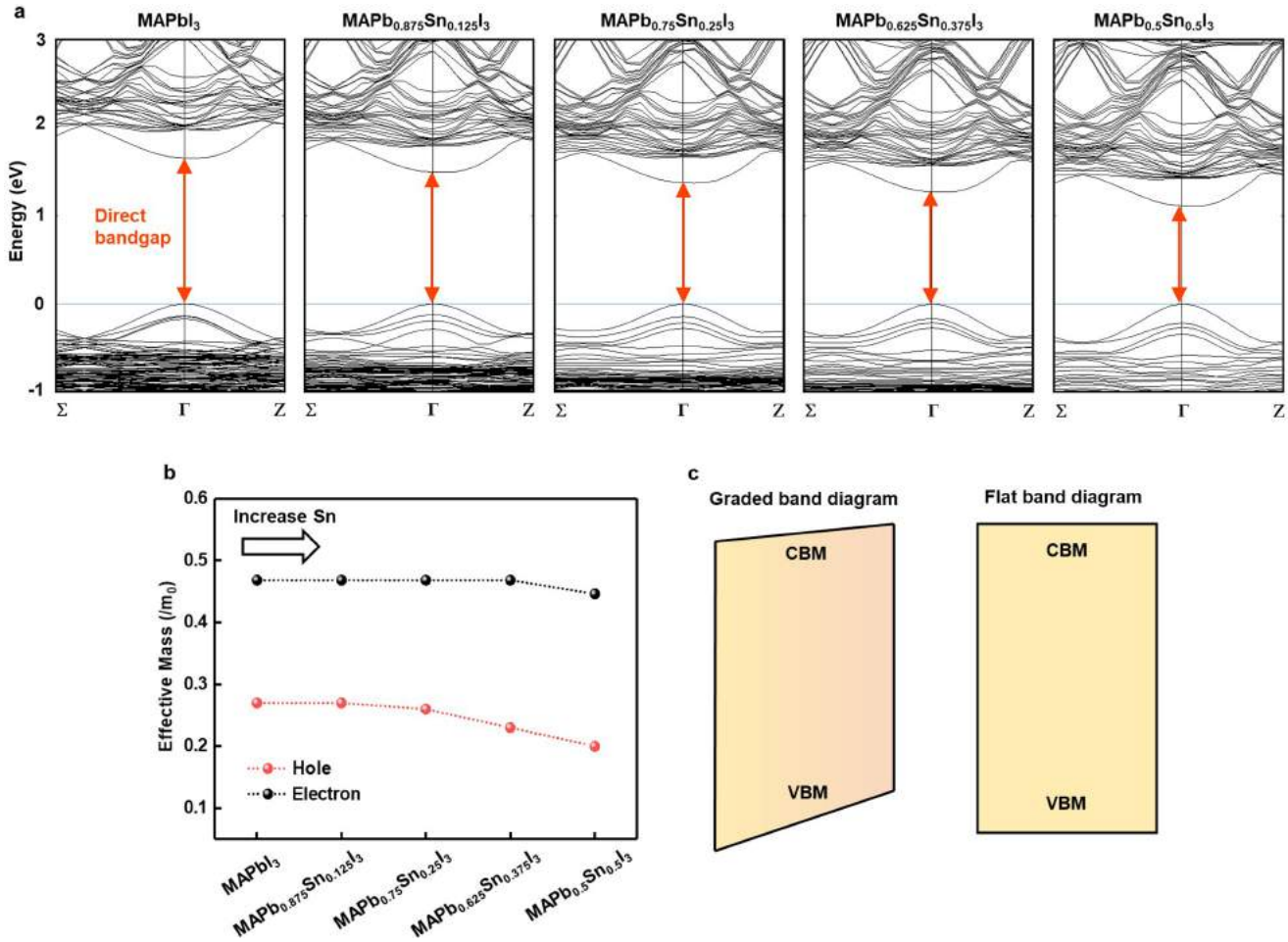

Extended Data Fig. 7 | Density-functional theory simulations of the graded single-crystal perovskites. a, Calculation results showing electronic band structures of the graded single-crystal $MAPb_{0.5+x}Sn_{0.5-x}I_3$. All structures show direct bandgaps at the Γ point. The Fermi level is normalized to the VBM, to show the shrinking tendency of the bandgap. **b**, Calculated effective masses for electrons and holes in the graded single-crystal $MAPb_{0.5+x}Sn_{0.5-x}I_3$ with an increasing tin concentration. The decreasing effective masses indicate increasing mobilities of both electrons and holes. The enhancement for holes is more pronounced than for electrons. **c**, Graded single-crystal $MAPb_{0.5+x}Sn_{0.5-x}I_3$ (left) showing a graded bandgap in comparison with the flat bandgap of conventional $MAPbI_3$ (right).

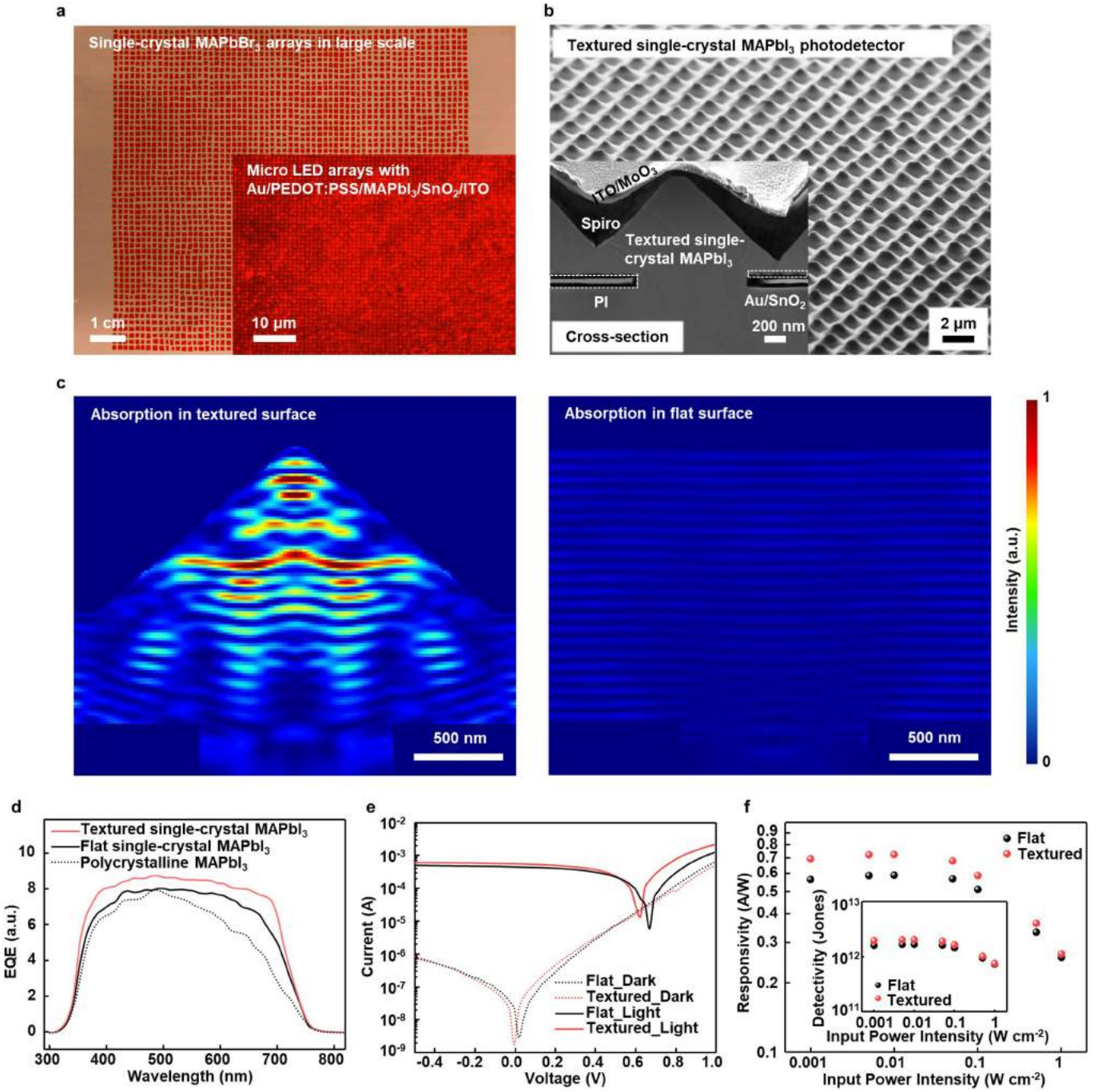

Extended Data Fig. 8 | Single-crystal perovskite thin-film light-emitting diodes and photodetectors fabricated using this growth-and-transfer method. a, Transferred single-crystal $MAPbBr_3$ arrays with each pixel about 100 μm by 100 μm. Inset: the transferred single-crystal $MAPbI_3$ micro light-emitting diode arrays with each pixel about 1 μm by 1 μm. **b**, SEM images showing the textured single-crystal $MAPbI_3$ thin film as a photodetector. Inset: a magnified SEM image of the cross-sectional structure of the device. PI, polyimide. **c**, Finite-difference time-domain optical simulation of the overall absorption by the textured structure (left) and the flat structure (right). The absorption by the textured thin film is much higher than that by the flat one because of the anti-reflective effect. **d**, EQE measurements of different device morphologies. The textured single-crystal film shows the highest quantum efficiency, which comes from the reduced surface reflections. **e**, Dark current measurements on both textured and flat single-crystal devices show that the current levels are similar, indicating the pinhole-free and high-quality thin films. The higher light current of the textured device reveals its higher absorption compared with the flat device. **f**, Responsivity results show that the textured devices are more sensitive to the input power. The inset shows that the textured devices exhibit a higher detectivity than the flat devices. The decreasing tendencies of the responsivity and detectivity at high input power may be due to the material degradation under strong light intensities.

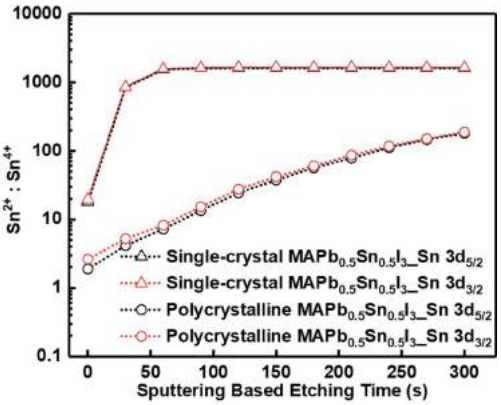

Extended Data Fig. 9 | In situ XPS depth profile studies of different crystal structures. In the single-crystal sample, only the surface areas are easy to be oxidized, indicating that the self-doping in deep areas away from the surface is relatively slow. In the polycrystalline sample, the oxidation is much faster in deep areas compared with the single-crystal samples, indicating that the grain boundaries facilitate the oxidation process.

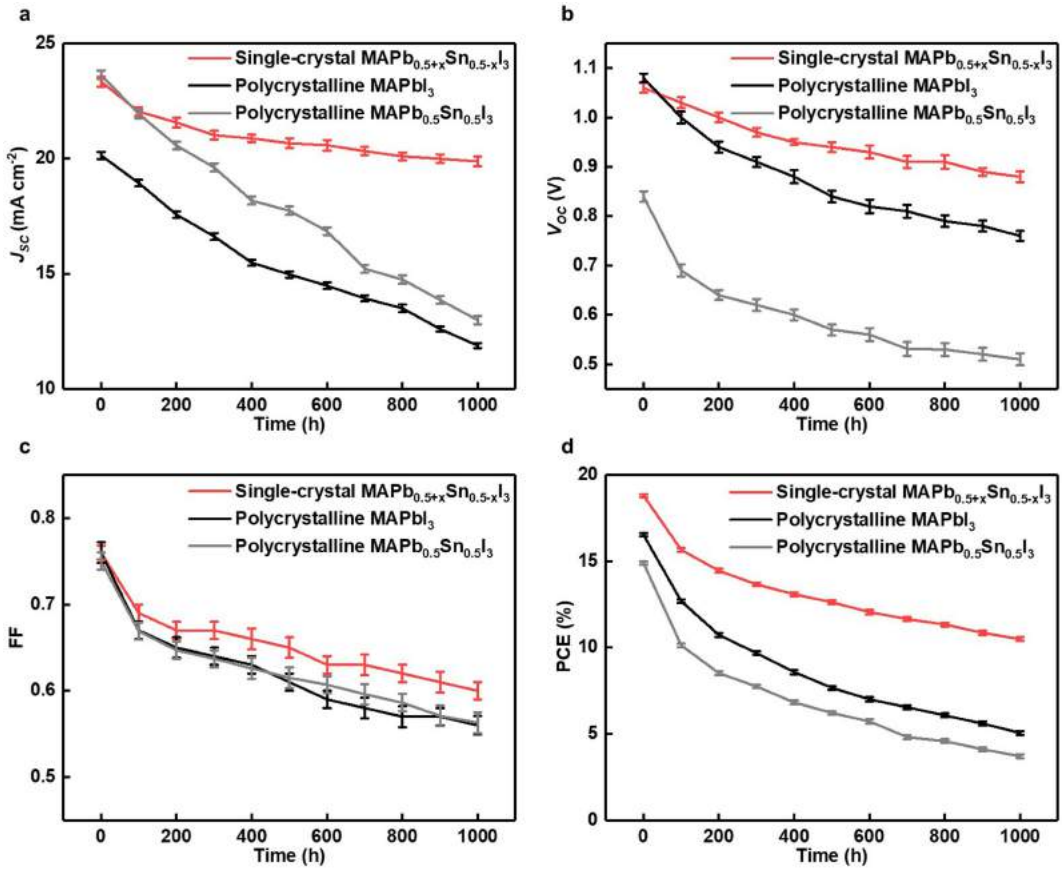

Extended Data Fig. 10 | Long-time continuous illumination stability tests. **a**–**d**, Summarized tracking results of J_{SC} (**a**), V_{OC} (**b**), FF (**c**) and PCE (**d**). The differences between single-crystal and polycrystalline devices are not as large as for the shelf-stability tests in Fig. 4f, which may be because of the poor thermal stability of the hole transport layer (spiro) used in all of these devices. In any case, relatively speaking, single-crystal devices show a better stability than polycrystalline devices.

nature

https://doi.org/10.1038/s41586-020-2526-z

Supplementary information

A fabrication process for flexible single-crystal perovskite devices

In the format provided by the authors and unedited

Yusheng Lei, Yimu Chen, Ruiqi Zhang, Yuheng Li, Qizhang Yan, Seunghyun Lee, Yugang Yu, Hsinhan Tsai, Woojin Choi, Kaiping Wang, Yanqi Luo, Yue Gu, Xinran Zheng, Chunfeng Wang, Chonghe Wang, Hongjie Hu, Yang Li, Baiyan Qi, Muyang Lin, Zhuorui Zhang, Shadi A. Dayeh, Matt Pharr, David P. Fenning, Yu-Hwa Lo, Jian Luo, Kesong Yang, Jinkyoung Yoo, Wanyi Nie & Sheng Xu ✉

Supplementary Information for:

A fabrication process for flexible single-crystal perovskite devices

Yusheng Lei[1*], Yimu Chen[1*], Ruiqi Zhang[1], Yuheng Li[1], Qizhang Yan[1], Seunghyun Lee[2], Yugang Yu[3], Hsinhan Tsai[4], Woojin Choi[5], Kaiping Wang[3], Yanqi Luo[1], Yue Gu[3], Xinran Zheng[6], Chunfeng Wang[7], Chonghe Wang[1], Hongjie Hu[1], Yang Li[1], Baiyan Qi[3], Muyang Lin[1], Zhuorui Zhang[1], Shadi A. Dayeh[1,3,5], Matt Pharr[2], David P. Fenning[1], Yu-Hwa Lo[3,5], Jian Luo[1,3], Kesong Yang[1], Jinkyoung Yoo[4], Wanyi Nie[4], Sheng Xu[1,3,5,8#]

[1]Department of Nanoengineering, University of Californian San Diego, La Jolla, CA 92093-0448, USA

[2]Department of Mechanical Engineering, Texas A&M University, College Station, TX 77843, USA

[3]Material Science and Engineering Program, University of Californian San Diego, La Jolla, CA 92093-0418, USA

[4]Los Alamos National Laboratory, Los Alamos, NM 87545, USA

[5]Department of Electrical and Computer Engineering, University of Californian San Diego, La Jolla, CA 92093-0407 USA

[6]Department of Physics, Tsinghua University, Beijing 100084, P.R. China

[7]College of Physics and Optoelectronic Engineering, Shenzhen University, Shenzhen 518060, P.R. China

[8]Department of Bioengineering, University of Californian San Diego, La Jolla, CA 92093-0412, USA

[*]These authors contributed equally to this work.

[#]Email: shengxu@ucsd.edu

Supplementary Discussion 1: The lithography-assisted-epitaxial-growth-and-transfer method.

With a set of unique optoelectronic properties[1-4], organic-inorganic hybrid perovskites have become an important material family for photovoltaics. Compared to their well-studied polycrystalline counterpart[5], single-crystal perovskites have shown higher carrier transport efficiency and stability due to lower defect concentrations[6-8]. Besides, their uniform orientations provide possible approaches to understand the orientation-dependent carrier behaviors[9-11], where the variations are ascribed to anisotropically distribute trap densities. Highly oriented near-single-crystal polycrystalline perovskite photovoltaics with the enhanced performance have been reported[12,13], indicating an exquisite control of crystal orientation can be an effective strategy to boost the photovoltaic efficiency[9,11], which is impossible to achieve in polycrystalline photovoltaics due to the random grain.

However, challenges for single-crystal perovskite photovoltaics remain in terms of material growth: no growth method has demonstrated simultaneous control over material thickness and area, or growth of a single crystal with a composition gradient[6,14], yet these are closely tied to photovoltaic performance. For optimal charge carrier collection efficiency in hybrid perovskite devices, a film needs to be sufficiently thin[15]; for practical device integration, the thin film needs to be grown over a reasonably large area.

So far, several attempts have been reported to control the crystal dimensions, such as mechanical cutting, roll-imprinting, and space confinement. However, those methods either lack precisely control in both the thickness and area or have strict substrate condition requirements. Single-crystal $MAPbI_3$-based photovoltaics was reported with 21% efficiency by the space confinement method[16]. However, clamping growth solutions between two holders for the crystal

growth into the nano/micro scale in a controllable way is challenging. Crystallization will always happen at the interface with the air by solvent evaporation, which disturbs the following thin crystal growth. Any solvent residues can result in serious interface hydration formation and dissolve the charge transport layers assembled during the thin film growth process[16]. The roll-imprinting method for fabricating single-crystal $MAPbI_3$ photovoltaics was reported with 4% efficiency[8]. Even though the thickness of as-fabricated single-crystal $MAPbI_3$ can reach 500 nm, the requirements on the printing substrate restrict the device structure to be lateral, which limits the performance of subsequent devices. Thin single-crystal $MAPbI_3$ films could also be fabricated by mechanical cutting and etching[17]. However, the thickness is still not considered to be sufficiently thin, and the wet chemical etching may damage the perovskites as well. More importantly, none of the existing crystal growth methods has achieved the material composition gradient, and thus the graded bandgap in hybrid perovskite crystals[18], despite its potential ability to maximize light absorption and enhance carrier collection efficiency.

To overcome those challenges, we report a solution-based lithograph-assisted-epitaxial-growth-and-transfer method. The general process of the growth/transfer method is presented in Fig. 1a and Supplementary Fig. 1a. Here, parylene (or polyimide, PI) is used as the transfer layer[19], and no metal or other electron transport layer/hole transport layer (ETL/HTL) layers are needed during the growth/transfer process. We fix the pattern geometry to be 1 μm by 1 μm, the thickness of parylene (or PI) can vary from 2 μm to 10 μm. One of the single-crystal perovskite substrates is placed into a polydimethylsiloxane (PDMS) growth mold and covered by a patterned parylene (or PI) layer. Before the growth, a freshly prepared $MAPbI_3$ gamma-butyrolactone (GBL) (1M) solution is evaporated under 80 ºC for 6 hours to achieve a near-saturated condition, which is used as the growth solution. Otherwise, because of the high

solubility of $MAPbI_3$ in GBL solvent, the growth solution will immediately dissolve parts of the single-crystal substrates and destroy the pattern.

For epitaxial single-crystal perovskite thin films growth, the as-prepared growth solution is heated up to a preset temperature. The growth mold is then placed into the pre-heated growth solution for a particular amount of growth time. Precise thickness, area, and shape control of the epitaxial single-crystal thin films can be achieved by adjusting the growth temperature, time, and the lithography layout. The design of the growth mask serves as the mechanism for controlling the thickness of the epitaxial layer.

During the growth process, the epitaxial single-crystal perovskites (e.g., $MAPbI_3$ or $MAPbBr_3$) grow three-dimensionally under the natural behaviors of this kind of material. No additional capping agents or physical covers are used to control its growth behavior. Initially, small crystals nucleate on patterned growth sites, each having an epitaxial relationship with the substrate. As growth continues, the small crystals gradually expand and merge, forming a monolithic single-crystal film. The overall growth process can be divided into four steps (Extended Data Fig. 1a). In step 1, photolithography has been applied to generate masks on the single-crystal perovskite substrate. The schematic cross-section shows that the width of the pattern (L_p) and the distance between the patterns (L_d) are about the same (L_p=L_d). If L_p is too large, it is impossible to peel off the epitaxial film because the connection between the epitaxial layer and the substrate is too strong. In step 2, the growth starts. The epitaxial crystals fill the pattern openings, until the horizontal level of epitaxial crystals and the top surface of the mask are about the same. In step 3, the epitaxial crystals are growing out of the pattern openings, where the growth rate in *x*-*y* directions ($r_{x\text{-}y}$), in principle, equals the rate in the *z* direction (r_z, $r_{x\text{-}y}$=r_z). Therefore, the grown lengths in all directions ($L_{x\text{-}y}$, L_z) are considered to be the same ($L_{x\text{-}}$

97 $_y$=L_z). As the growth continues, adjacent crystals will start to merge. The thickness of such a
98 merged thin film L_z is only half of the L_d. The smaller the designed L_d, the thinner the epitaxial
99 film. In step 4, the epitaxial crystals fully merge into a continuous thin film and grow only in
100 thickness.

101 Because the epitaxial nature of the growth process, all crystals grown from the individual
102 exposed area have the same lattice structure, morphology, and orientation, which are all
103 determined by the substrate[20]. When two adjacent epitaxial crystals are growing large enough to
104 contact with each other, there will be no tilting or twisting of the lattice at the interface.
105 Therefore, no grain boundaries will be formed when adjacent crystals are merging with each
106 other.

107 The different stages during the growth/transfer growth process can be revealed by scanning
108 electron microscope (SEM) images, which may better illustrate the merging of the epitaxial
109 crystals (Extended Data Fig. 1b). Also, the high-resolution transmission electron microscope
110 (TEM) image in Figure 1c can clearly reveal the chemical epitaxial relationship between the
111 substrate and the as-grown thin film. X-ray diffraction (XRD) measurements in Figure 1d also
112 serve as additional evidence that the epitaxial crystals have the same orientation as the substrate.

113 Additionally, it has also been found that the growth rate in different directions can be
114 effectively tuned by using different growth temperatures and precursor concentrations (Extended
115 Data Fig. 1c). At a low growth temperature, the growth rates in all directions are low because of
116 the temperature-reversal growth behavior. The growth rate would be surface reaction controlled.
117 Then the precursor molecules have sufficient time to diffuse and adsorb at the most energetically
118 favorable locations. The tri-phase interface between the single-crystal perovskite, substrate
119 surface, and the growth solution is more favorable for nucleation and growth than the bi-phase

120 interface between the single-crystal perovskite and the growth solution. Therefore, the precursor
121 molecules would prefer to adsorb at the tri-phase boundary, which contributes to the growth in
122 the *x*-*y* directions. This is also why in the literature, almost none of the freestanding bulk single
123 crystals has perfect cubic shapes. The footprint of these bulk single crystals on the substrate is
124 always larger than their heights[14,21,22]. The same analysis applies to the scenario when the growth
125 rate is low at a low precursor concentration. With the same pattern design, high growth
126 temperature and precursor concentration lead to vertically standing rods. Because of the high
127 growth rate under the high temperature and concentration, the crystals would quickly consume
128 the precursor molecules in their vicinity. The growth rate is diffusion controlled. Precursor
129 molecules would be depleted in between the crystals, and therefore the growth along the *x*-*y*
130 directions is slowed down due to the internal competition for precursor molecules. The growth
131 rate would be dependent on the precursor diffusion from the bulk solution, which is from the *z*
132 direction of the crystals. Fresh precursor molecules would first arrive at the top surface of the
133 crystals and thus contribute to the fast growth along the *z*-direction of the crystals.

134 After epitaxial growth, an in-plane rotation of the parylene (or PI) together with the top
135 epitaxial thin film is necessary to break the connected single-crystal micro-rods between the
136 epitaxial single-crystal layer and the single-crystal substrate; otherwise, directly lifting up the
137 epitaxial layer will break the epitaxial single-crystal layer.

138 The whole process can be divided in six steps (see Supplementary Fig. 1a for detailed
139 schematics). In step 1, a single-crystal perovskite substrate is placed into a PDMS growth mold
140 for epitaxial growth. The height of the substrate does not need to be the same as the depth of the
141 pattern in the mold. If the surface of the substrate is lower than the surface of the PDMS mold,
142 the epitaxial crystals will fill the gap first and then grow out. If the surface of the substrate is

143 higher than the surface of the PDMS mold, the attached soft mask can tightly cover the substrate.
144 In step 2, a soft pre-patterned parylene (or PI) film is fixed with two glass holders on the two
145 ends as a mechanical handle. Then, the mask is attached to the PDMS mold. In step 3, the growth
146 solution is introduced to the growth mold for the epitaxial growth, with controlled temperature,
147 time, and precursors. In step 4, the epitaxial single-crystal films can grow out of the mask with
148 different thicknesses, morphologies, and compositions, depending on the growth conditions. In
149 step 5, the top parts (i.e., the epitaxial film and the parylene or PI mask) need to be partially
150 lifted up to separate the glass holder and the PDMS substrate. The rotational movement of the
151 substrate is still restricted by the PDMS holder. In step 6, the parylene or PI-glass holder will be
152 rotated to break the connection. The substrate will be detached from the growth mask.

153 Optical images in Supplementary Fig. 1b show the top (left) and the bottom (right) sides of
154 the single-crystal $MAPbI_3$ after the in-plane rotation. The broken single-crystal micro-rods can
155 be clearly seen in the soft transfer mask. XRD ω scan and photoluminescence (PL)
156 measurements (Supplementary Fig. 1c and 1d) have also been used to further study the crystal
157 quality before and after the in-plane rotation. From the XRD results, no obvious change can be
158 found, indicating the crystal quality before and after the in-plane rotation is similar. PL
159 measurements exhibit a comparable result, where the full-width-at-half-maximum (FWHM)
160 values do not have a noticeable change before and after the in-plane rotation. Note that the PL
161 measurements give narrower peaks from the bottom side compared with the top side, because the
162 bottom surfaces are freshly broken from the bulky parts, whose defect levels are found to be
163 much lower than the existing surfaces that have been treated by solvents[22,23].

164 After the in-plane rotation step, the following re-adhesion process can be divided into two
165 types. For the simple transferring purpose, diethyl ether can be used as an assistant antisolvent

166 for transferring onto arbitrary substrates. It is worth to point out that the antisolvent for single-
167 crystal perovskite transfer in this work is fundamentally different from that in depositing the
168 polycrystalline perovskite, where the antisolvent is used to quickly wash the precursor solvent
169 (e.g., dimethylformamide, DMF, and dimethyl sulfoxide, DMSO) to uniformly and rapidly
170 crystallize the polycrystalline perovskite. In this work, the anti-solvent is to facilitate the transfer
171 process in a more convenient way when no strong interfacial adhesion force is needed. The weak
172 adhesion provided by the antisolvent is sufficient for experiments such as taking SEM images,
173 measuring thickness-dependent properties, and characterizing the crystal quality of the
174 transferred single-crystal film. As a commonly used anti-solvent in polycrystalline perovskite
175 thin film deposition, diethyl ether has strong volatility and does not dissolve the perovskite.
176 Therefore, diethyl ether can be used as a re-adhesion solvent.

177 The adhesion force between the perovskite single crystals and the substrates has been
178 measured (Supplementary Fig. 2). It is clear to see that the simply attached single-crystal
179 perovskite shows no adhesion at all (Supplementary Fig. 2b), indicating the Van der Waals
180 contact and possible micro-gaps between two solids. Also, different antisolvents have similar
181 adhesion forces (Supplementary Fig. 2c).

182 However, for device fabrication, a strong interfacial contact is critical. Therefore, it is
183 necessary to spin coat a very thin layer of supersaturated growth solution onto the target
184 substrate first, followed by transferring the single-crystal thin film onto the substrate and baking
185 it under 80 ºC for 1 hour. The thin solution layer between the single-crystal thin film and the
186 substrate will introduce a secondary re-growth process: the supersaturated solution will be
187 gradually dried under heating, while new perovskites will be crystallized from the solution. The
188 transferred single crystal film will serve as an epitaxial substrate for growing the new single

189 crystals. As the growth is going on, the new single-crystal perovskite can not only fill any micro-
190 gaps between the two solids but also achieve strong adhesion with the substrate, in a similar way
191 to the spin-coating process. The bonding introduced by the crystal growth has been proved to be
192 able to exhibit a good adhesion with the substrate[24], and the measured strong adhesion force
193 confirmed our analysis (Supplementary Fig. 2d).

194 Finally, the parylene (or PI) can be removed by dry etching or direct peeling off, depending
195 on the thickness of the parylene (or PI) mask. For the dry etching of the parylene (or PI), O_2 (or
196 Cl_2 and Argon) plasma serves as the etchant, which has been reported to damage perovskite by
197 introducing a series of decomposition reactions[25]. Even though accurate etching power and time
198 are needed to remove the polymer mask and minimize the plasma damage, surface
199 decomposition after dry etching is inevitable. The surface after dry etching has to be cleaned to
200 remove any decomposition residues. Here, a supersaturated $MAPbI_3$ GBL solution will be used
201 to clean the surface by dynamic spin coating followed by 80 ºC baking for 1 min. Detailed
202 changes in this step are presented in Supplementary Fig. 3. After the dry etching, periodic
203 features can be seen from the SEM image (Supplementary Fig. 3a). The zoomed-in SEM image
204 shows very rough morphology, which should be resulted from the plasma damage.

205 After washing the perovskite surface with the saturated GBL solution, the rough surface
206 becomes very smooth without any noticeable particles or residues. By using the saturated
207 solution, the perovskite will be minimally dissolved, but the non-perovskite materials can be
208 quickly washed away by the GBL. atomic force microscopy (AFM) measurements confirm the
209 observations by the SEM (Supplementary Fig. 3b). XRD ω scan and PL measurements also
210 confirm the dramatic changes before and after washing the perovskite film with the saturated
211 GBL solution (Supplementary Fig. 3c and 3d). Before the washing, the FWHM of the XRD

212 peaks is around 0.065, and the PL signals are very weak, indicating that the crystal quality has
213 been degraded a lot by forming non-crystalline residues. However, the FWHM of the same
214 sample after washing can be effectively reduced to be around 0.03, and the PL signals are much
215 enhanced, showing that surface defects induced recombination has been largely reduced after
216 washing.

217 A continuous growth system plays a critical role in realizing the graded single crystals.
218 Otherwise, there will be clear structural interfaces of heterojunctions, which will serve as carrier
219 recombination centers, decreasing the device performance[26]. The continuous growth system is
220 realized by setting two pumping systems to the growth solution: one injects new precursors while
221 the other extracts supernatant precursors (Extended Data Fig. 6a). A 20 mL container with an
222 open hole is used to hold the growth solution. The open hole can drain unneeded precursors for
223 realizing the continuously changed compositions in the growth solution. A single-crystal
224 perovskite substrate in a PDMS holder is placed into the glass container. Then, perovskite
225 precursor 1 is added into the container, where the top of the solution is at the same level as the
226 bottom of the hole to make sure that the solution can be timely and effectively washed out. After
227 that, a glass tube is inserted to the bottom of the container to serve as the feeding source of a
228 different perovskite precursor 2 for changing the growth solution composition. The feeding
229 speed is dependent on the growth speed (e.g., growth temperature, precursor concentration) and
230 the container volume, and can change with different setups.

231 Here we are sharing our recipes as a reference: if a ~5 mm thick graded crystal needs 2
232 hours to grow at certain conditions, the whole solution (precursor 1) needs to be fully exchanged
233 in 2 hours. With a container volume of 5 mL, the pumping speed should be 41.67 μl min^{-1}. If a
234 high temperature/concentration and a smaller container are used, the growth time for 5 mm

235 thickness may be reduced to 1 hour. Using a volume of 3 mL, the pumping speed should be 50 μl
236 min^{-1}. For very small thickness growth, the growth time is much shorter. If 0.5 mL 1 M solution
237 is used under 80 ℃, then the pumping speed is 1 ml min^{-1} for growing a 2 μm thick film.
238 It is important to note that the injected new precursor (precursor 2) needs to be pre-heated to
239 the same temperature as the growth condition. Otherwise, the freshly mixed solution during the
240 precursor exchanging will not be able to reach the preset temperature, which makes it difficult to
241 identify the real growth temperature. The lukewarm solution may also dissolve the already
242 grown epitaxial single-crystal thin crystals/films. We can design different pumping speed to
243 grow different gradient profiles. This method is applicable to general hybrid perovskites. Graded
244 single-crystal perovskites can be grown with different ion combinations and ratios of cations and
245 anions (Extended Data Fig. 6b).
246
247 **Supplementary Discussion 2: Interfacial quality studies in the growth/transfer process.**
248 The interfacial adhesion between different layers of materials in single-crystal perovskite
249 electronic devices is one of the major challenges. In particular, the interface between single-
250 crystal perovskite and other functional layers (e.g., ETL, HTL) can substantially determine the
251 charge transfer and the device performance. Therefore, it is important to understand the
252 interfacial quality in the growth/transfer process. In the growth/transfer process, there are two
253 steps that involve the usage of solvents to treat the interface of the single-crystal perovskite thin
254 films. The first is to do the re-adhesion/re-growth in the transfer process. The second is to wash
255 the single-crystal perovskite surface after dry etching.
256 1. Re-adhesion/re-growth process.

257 In the re-adhesion/re-growth step, the supersaturated growth solution is firstly spin-coated
258 onto the target substrate. Then, the peeled-off single-crystal $MAPbI_3$ thin film is attached to the
259 supersaturated growth solution on the substrate. Finally, the entire system is placed onto a
260 hotplate until full growth of new single crystals from the spin-coated supersaturated growth
261 solution. In this whole process, the substrates are only playing as inert "holders" to mechanically
262 support the spin-coated growth solution and are not chemically involved in the growth process.
263 The substrates do not react with the solution or the perovskite materials. Therefore, the growth
264 behaviors, crystal structures, and interface properties of single-crystal perovskite should not be
265 influenced by the substrates. To clearly reveal the quality at the interface, systematic studies
266 include TEM, XRD, optical topography, PL, temperature-dependent Hall mobility, time-resolved
267 PL, trap density, transient photovoltage (TPV), transient photocurrent (TPC), adhesion force, and
268 contact angle have been performed. Besides, different kinds of substrates have also been studied
269 to qualify substrate independence. The detailed discussions can be seen below.

270 Different from the case of preparing polycrystalline perovskite films, the perovskite solution
271 is spin-coated onto a substrate, followed by annealing, where the crystal quality has been proven
272 to be substrate-dependent. The major reason is that those interfacial properties of the substrate
273 can largely influence nucleation, growth, and formation of the perovskite and may cause an
274 incomplete conversion from the precursor to crystals during the rapid deposition process[27-30].
275 However, the mechanism of preparing single crystals in this study is totally different. Unlike the
276 rapid crystallization process in the spin-coating method, the process in this study is epitaxial
277 growth, where the transferred single crystal thin film is serving as the real epitaxial substrate for
278 interfacial crystal growth. The nominal substrate at the bottom is only providing the mechanical

support for the growth process. Therefore, the substrate properties should have minimal influences on the quality of interfacial crystals.

The overall crystal quality of the transferred single-crystal $MAPbI_3$ after the re-adhesion/re-growth process on different substrates has been studied by XRD and PL. XRD ω scan has been performed for the transferred single-crystal $MAPbI_3$ on different substrates (Supplementary Fig. 8a), whose FWHM is commonly used to evaluate the crystal quality[31-33]. It can be seen that the FWHM of the XRD peaks does not show noticeable changes with different kinds of substrates. PL measurements (Supplementary Fig. 8b) also exhibit similar results, where both the intensities and the FWHM of the peaks do not change with different substrates, indicating that the possibility of radiative recombination and the crystal quality are similar to each other[34].

However, substrates with different wetting behavior of the precursor solution will influence the adhesion force between the crystals and the substrate. If wetting is poor, even though the re-growth can still happen, the bonding between the single crystal and the substrate will be weak. Adhesion forces have been measured under good and poor wetting conditions on different substrates. Usually, the wetting is considered to be poor if the contact angle is between 90° and 180°, and good if the contact angle is less than 90° (Supplementary Fig. 9). The contact angle can be roughly controlled by adjusting the time for treating the substrate surface using ultraviolet light ozone (UV-ozone) or oxygen plasma. As long as the time of substrate treatment is enough, all substrates used in this study produce similarly high adhesion force of the single-crystal perovskite. For example, even though the PDMS surface is one of the most difficult substrates for achieving good wetting with the precursor solution, we found 10-min UV-ozone treatment to be enough to achieve good wetting. A good wetting condition can always result in a strong

301 adhesion force, regardless of the substrates. Good adhesion between the single-crystal perovskite
302 and the substrate is necessary for achieving high-performance photovoltaic devices.

303 To reveal the interfacial crystallinity at the interface, interfacial cross-section of the crystals
304 on different substrates has been studied by high-resolution TEM. Specifically, Au, glass, and
305 PDMS substrates are chosen to represent metals, oxides, and polymers. The results can be seen
306 in Extended Data Fig. 2. All of those high-resolution TEM results show distinct boundaries
307 between the single-crystal thin film and the substrate, where no noticeable polycrystalline or
308 amorphous structures can be found in the single-crystal $MAPbI_3$, indicating that the re-
309 adhesion/re-growth process maintains the high-quality lattice structure of $MAPbI_3$. The reason is
310 that the re-adhesion process is also an epitaxial growth process: during the re-adhesion process,
311 the transferred single-crystal $MAPbI_3$ thin film actually serves as the real "substrate" to guide the
312 epitaxial growth. The transferred single-crystal $MAPbI_3$ thin film, which will not be dissolved in
313 the supersaturated solution, can be considered as a huge "seed crystal" to guide the epitaxial
314 growth. At a relatively slow growth rate of the chemical growth compared with the rapid
315 dynamic spin coating, it is favorable to form epitaxial single crystal from the supersaturated
316 solution. Therefore, the re-growth process will always follow the epitaxy and maintain a high-
317 quality lattice structure.

318 Additionally, hybrid perovskite includes organic and inorganic components. The results
319 from the high-resolution TEM show only the inorganic framework. It is worthwhile to
320 quantitatively investigate the influence of the sensitive organic component[35] on the trap and
321 defect states.

322 (1) Thickness-dependent PL studies.

323 Thickness-dependent PL has been studied to investigate the interfacial crystal quality.
324 Supplementary Fig. 4a shows the schematic setup: a transparent substrate (glass) has been used
325 to perform the re-adhesion/re-growth process so that the confocal laser beam is able to access the
326 interfacial area. A control device with a simple physical contact to the glass substrate has also
327 been measured. With different focal levels, as shown in Supplementary Fig. 4b, the PL intensity
328 decreases because of the self-absorption from deeper focal levels in the single-crystal perovskite.
329 The corresponding FWHM of the PL peaks at different focal levels show that the interfacial
330 regions in both devices have the largest FWHM (Supplementary Fig. 4c), indicating relatively
331 lower crystal quality at the interface compared with those in the bulk. Such a relatively lower
332 crystal quality at the interface can also be revealed from the thickness-dependent carrier lifetime,
333 carrier mobility, crystallinity, and trap density (Extended Data Fig. 4b and 4c, and
334 Supplementary Fig. 13).

335 The re-adhesion/re-growth device exhibits a slightly larger FWHM value than the control
336 device near the interface, which means the re-adhesion/re-growth step reasonably degrades the
337 interfacial crystal quality in comparison with naturally grown single crystals. The mechanisms
338 are discussed in the following paragraphs.

339 (2) Hall mobility studies.

340 Hall mobility has been used to provide additional evidence for evaluating the interfacial
341 crystal quality. In general, interfaces formed under different conditions can significantly
342 influence the charge dynamics. Supplementary Fig. 5a shows the schematics of the measurement
343 setup. A control device is fabricated by depositing four Au electrodes using E-beam evaporation
344 on top of one surface of a single-crystal perovskite. The results in Supplementary Fig. 5b show

that the interfacial Hall mobility in the growth/transfer device exhibits a moderate loss and a slightly larger variation compared with the control device.

To understand the mechanism of the interfacial mobility loss, temperature-dependent Hall measurements have been used to study the interfacial scattering. In theory, the main factor for determining the carrier mobility is the scattering: impurity scattering and phonon scattering, which can be described by the Matthiessen's Rule[36,37]:

$$\frac{1}{\mu} = \frac{1}{\mu_{impurities}} + \frac{1}{\mu_{lattice}}$$

where μ is the actual mobility, $\mu_{impurities}$ is the mobility of the material if impurity is the only source of scattering, and $\mu_{lattice}$ is the mobility of the material if phonon is the only source of scattering. Normally, with an increasing temperature, phonon concentration increases and starts to dominate the scattering. Theoretical calculations have already revealed that the mobility in perovskite is dominated by phonon interaction at room temperature[38-41], where the relationship between the mobility and the temperature is expected to be described by an inverse power-law with $\mu \propto T^{-3/2}$. The effect of impurity scattering, however, decreases with increasing temperature because the average thermal speeds of the carriers are increased. These two effects operate simultaneously on the carriers through Matthiessen's rule: at lower temperatures, impurity scattering dominates; while at higher temperatures, phonon scattering dominates.

From the measurements, all devices exhibit an inverse power-law temperature dependence (Supplementary Fig. 5c). In the high temperature tetragonal phase, the power exponents are fitted to be -1.46 and -1.44 for the control device and the growth/transfer device, respectively. The power exponents being very close to -3/2 suggests that phonon scattering (in the form of a deformation potential scattering) is dominating the charge transport in both tetragonal phases,

367 and the difference between the two devices is negligible. However, as the temperature decreases
368 to around 150 K, the crystal undergoes a transition from the tetragonal phase to the orthorhombic
369 phase with a relatively abrupt changing of mobility. After that, even though the mobility
370 continues to increase with cooling, power exponents become smaller, around -0.47 and -0.33 for
371 the control device and the growth/transfer device, respectively. The change of the power
372 exponents associated with the phase transition suggests that the carrier scattering in the
373 tetragonal and orthorhombic phases are governed by different mechanisms. The smaller power
374 exponent obtained suggests an enhanced weight of impurity scattering, where such a
375 phenomenon is more noticeable in the growth/transfer device, indicating an increased impurity
376 scattering.

377 (3) Interfacial trap density studies.

378 Interfacial trap densities of a similar device setup have been measured to confirm the Hall
379 mobility studies. The results are seen in Supplementary Fig. 6. Here, the SiO_2 layer is deposited
380 by sputtering to control the measurement heights in the thickness direction of the single-crystal
381 perovskite. The thicker the SiO_2 layer, the further the measured region is away from the interface.
382 The results also show a similar trend to the Hall mobility studies, confirming that the re-growth
383 step can slightly degrade the interfacial crystal quality, which is reflected by a higher trap density
384 of the growth/transfer device.

385 Additionally, we measured the overall carrier lifetime and carrier mobility using TPV and
386 TPC to estimate how the interfacial quality can influence the overall crystal properties.
387 Supplementary Fig. 15b and 15c show the measurement results. The growth/transfer process can
388 decrease the carrier mobility and lifetime by ~4-5%, which is considered to be insignificant. The

interfacial quality can be improved by surface/interface passivation to enhance the device performance.

Based on all studies above, we conclude that in the growth/transfer process, the substrates do not play a role more than a mechanical support. The as-transferred single-crystal $MAPbI_3$ thin film serves as the real "substrate" to guide the epitaxial growth. As long as the transferred single-crystal $MAPbI_3$ is not dissolved in the supersaturated solution, the subsequent re-growth/re-adhesion process will always result in the single-crystal structure rather than the polycrystalline structure at the interface. Although the interfacial crystal quality shows slight degradation because of a higher level of impurity scattering as evidenced by the temperature-dependent Hall mobility measurements, the physical lattice structure and the crystallinity near the interface of the growth/transfer device do not change. The measured electronic dynamics of the growth/transfer device are on par with those of the bulk single crystals.

2. The GBL solution washing process

In the GBL solution washing process after dry etching, the non-crystalline residues on the surface of the single-crystal film can be effectively removed (Supplementary Fig. 3). SEM and AFM studies confirm the dramatic change of morphologies. XRD ω scan and PL measurements confirm the dramatic change of crystal quality before and after washing the perovskite film with the saturated GBL solution. Detailed discussions can be seen in the Supplementary Discussion 1.

Supplementary Discussion 3: The scaled growth/transfer process.

The size of the single-crystal perovskite thin films can be scaled up by multiple transfer/fabrication. Additionally, refining the growth/transfer process can be effective in scaling up the thin film size. Basically, the growth/transfer process can be divided into three stages: 1.

412 Epitaxial growth; 2. Peeling off; 3. Transferring. The scale can be further increased by
413 addressing the following aspects.

414 For the first stage of epitaxial growth, the larger size of the growth substrate and the
415 patterned mask, the larger area of the epitaxial single-crystal perovskite film. The large size of
416 the substrate can be achieved by enlarging the crystal growth time[42]. The single-crystal
417 perovskite wafer of size 120 mm × 70 mm × 52 mm has been demonstrated[43]. The size of the
418 parylene (or PI) patterned mask can be as large as what the stranded lithography process allows.

419 For the second stage of peeling off, the most critical thing is to avoid breaking the epitaxial
420 single-crystal perovskite film. The larger the single-crystal thin film, the higher the possibility of
421 forming cracks. When the single-crystal thin film is larger, the size of the connected micro-rods
422 and the mask are also larger. Therefore, it will be more difficult to avoid bending during the in-
423 plane rotation. In this study, the transfer yield is found to be lower with larger single-crystal thin
424 films, because the larger single-crystal thin films are easier to be broken during the in-plane
425 rotation process. Even though increasing the thickness of the mask layer can help, the size with
426 acceptable yield is still within ~2 cm × 2 cm. To solve this problem, replacing the soft mask with
427 a more rigid mask (e.g., Cu foil) is found to be effective. A patterned Cu foil (20 μm thickness,
428 by laser drilling, Extended Data Fig. 3b) is used, which can realize ~5.5 cm × 5.5 cm single-
429 crystal perovskite film. The rigid Cu mask can largely avoid bending during the in-plane rotation,
430 which significantly reduces the possibility of breaking the epitaxial single-crystal perovskite.

431 Finally, for the stage of transferring, the only concern is that the mask should be able to be
432 etched without damaging the perovskite. Soft masks such as parylene (or PI) can be easily dry-
433 etched, which has minimal influence on the device performance, as discussed in the manuscript.

For rigid masks, e.g., the 20 μm Cu foil, the mask can be liftoff from the perovskite thin film after the transfer.

Besides, the scaled fabrication of single-crystal perovskite microstructure arrays is also feasible. Single-crystal perovskite-based light emitting diode (LED) devices have been fabricated (Extended Data Fig. 8a). The pixel size can be anywhere from 1 μm to 100 μm, with potential applications for flexible single-crystal perovskite LED displays with tunable color, high resolution, high stability, and high quantum efficiency.

Supplementary Discussion 4: Crystal quality after the growth/transfer method.

XRD, optical topography, and PL have been used to study the epitaxial single-crystal thin film fabricated by the growth/transfer method. During the growth/transfer process, there are two major factors that will influence the quality of the as-prepared single-crystal thin films: epitaxial growth and transfer/re-adhesion.

1. Epitaxial growth:

Because of the high solubility of perovskite in their growth solutions, the concentration/growth temperature of the solution used in the growth/transfer method is important. Too high concentrations/growth temperature will cause an inhomogeneous merging and result in an inhomogeneous monolithic surface, which is reflected as a wide FWHM in the XRD (Supplementary Fig. 11a-11c). In homo-epitaxial growth where there is no interfacial strain, such XRD peak broadening can be due to the small crystalline size, as explained by the Scherrer equation[44]:

$$\tau = \frac{K\lambda}{\beta cos\,\theta}$$

where τ is the mean domain size, K is the shape factor, λ is the wavelength of the X-ray, β is the

457 broadening at the FWHM, and θ is the Bragg angle. In a particular material, the domain size τ is
458 inversely proportional to the β. Even though the sub-micrometer particles or crystallites in the
459 inhomogeneous monolithic thin films show the same orientation, they represent small domains
460 and result in the XRD peak broadening.

461 After optimizing the growth concentration/growth temperature, FWHM values in the XRD
462 ω scan are studied to evaluate the mosaicity of the as-grown single-crystal perovskite thin films[45].
463 Comparable FWHM values from the as-grown single-crystal thin films with the corresponding
464 bulk single crystals demonstrate their similar crystal qualities (Fig. 1d), which mean the
465 growth/transfer process will not sacrifice the quality of the as-grown epitaxial single-crystal thin
466 films. The growth/transfer method can potentially be applied to a general perovskite in the
467 perovskite family with very different growth temperatures and crystallization conditions.

468 2. Transfer/re-adhesion:

469 Even though the growth process can be well-controlled, the single-crystal thin film quality
470 can still largely degrade if a suitable transfer/re-adhesion process is not followed (Supplementary
471 Fig. 11d-11f).

472 During the in-plane rotation, directly peeling off the epitaxial single-crystal films from one
473 side will break it into many pieces (Supplementary Fig. 11e top). This is because of the unique
474 growth process of the growth/transfer method: the epitaxial single crystals need to fill the pattern
475 first before growing out of the parylene (or PI) mask layer to merge into a thin film. Therefore,
476 the pattern in the mask layer is filled with single-crystal micro-rods that serve as the connection
477 between the epitaxial thin film and the substrate. Such a connection is strong and needs to be
478 broken before the transfer. Otherwise, the brittle single-crystal thin film can get easily broken.
479 Therefore, the in-plane rotation is critical to break those micro-rods and avoid breaking the

480 epitaxial single-crystal during the transfer.

481 During the re-adhesion process, the concentration of the growth solution must be
482 supersaturated. Otherwise, the growth solution will etch the single-crystal thin films quickly and
483 may dissolve them partially, which lowers their crystallinity (Supplementary Fig. 11f).

484 The overall crystal quality fabricated by the growth/transfer is studied using PL with an
485 excitation wavelength of 533 nm. A well-controlled single-crystal thin film can not only exhibit
486 a similar PL spectrum, but also show an I_{PL}/I_E (PL intensity/laser emission intensity) that is close
487 to the bulk crystals (Fig. 1e). However, a degraded single-crystal thin film shows a PL peak
488 broadening and an unstable I_{PL}/I_E, similar to the polycrystalline thin film (Supplementary Fig.
489 12).

490

491 **Supplementary Discussion 5: Diffusion length calculations.**

492 The optimal thickness for the photovoltaic material needs to strike a balance between the
493 photogenerated carrier diffusion length and optical light absorption length. To ensure efficient
494 charge collection, polycrystalline perovskite films are usually made sufficiently thin. The
495 existence of crystallographic structural defects within the grain and at grain boundaries, where
496 defects serve as trap states causing serious charge recombination, can heavily limit the charge
497 carrier diffusion length to be typically less than 1 μm[46,47]. Prior studies have demonstrated that
498 this balance in spin-coated polycrystalline perovskite is attained for a material thickness of ~500
499 nm[48]. Recently, with an advanced non-solvent method to produce low-defect polycrystalline
500 perovskite films, high-efficiency solar cells with thickness ~1.1 μm have been reported, where
501 the thick films are found to be more efficient on light conversion[49]. On the other hand, it has
502 been concluded that the incoming light should be mostly absorbed by the polycrystalline

perovskite with a thickness around 2 μm[50], indicating polycrystalline perovskite solar cells with a thickness 0.6~1 μm can efficiently collect the free carriers but do not make the best use of light.

As the single-crystal carrier dynamics and light absorption behavior are different from the polycrystalline[6], it is necessary to re-investigate the best thickness for an single-crystal absorber. According to the literature, the carrier diffusion length L_D can be calculated by[46]:

$$L_D = \sqrt{\frac{K_B \cdot T \cdot \mu \cdot \tau}{e}}$$

where K_B is the Boltzmann's constant, T is the temperature, μ is the carrier mobility, τ is the carrier lifetime, and e is the electron charge.

To calculate L_D for estimating a rough single-crystal perovskite thickness, the carrier mobility and lifetime are measured by time of flight (ToF) and time-resolved PL under 1-Sun intensity, respectively (Extended Data Fig. 4b and 4c). For the ToF measurement, all devices share the same Au/single-crystal perovskite/indium tin oxide (ITO) structure fabricated by e-beam evaporation and sputtering. By controlling the same deposition conditions for the ITO layer (power, time, and gas flow), possible plasma damage to the sample is controlled to be similar to each other.

The carrier mobility μ can be calculated from the carrier transit time by[22]:

$$\mu = \frac{d^2}{Vt}$$

where d is the thickness of the target region, V is the applied voltage, and t is the measured carrier transit time. The average carrier lifetime of the single crystals is measured by time-resolved PL[21].

523 Measured results show that both the carrier mobility and carrier lifetime are thickness-
524 related and exhibit saturating tendencies, which indicate a "maximum" L_D if the film thickness
525 increases to a certain level (Extended Data Fig. 4a). Usually, mobility will not change with
526 different thickness. However, unlike well-established solvent engineering in polycrystalline
527 perovskite thin film preparation, current perovskite single crystals grown by wet chemical
528 methods are found to have high surface defect centers[22,23,51], which are orders of higher than
529 those in polycrystalline films[52]. Additionally, thinner single-crystal films have a relatively higher
530 surface-to-volume ratio, indicating that the surface can play an important role, especially when
531 the surface properties are dominating. The reduced surface-to-volume ratio in thicker single-
532 crystal films will result in a better overall crystal quality with higher carrier mobility and lifetime
533 (Extended Data Fig. 4b and 4c).

534 To clearly exhibit such a property, thickness-dependent XRD, PL, and trap density[21] have
535 been studied to quantitatively evaluate the crystalline quality of the epitaxial thin films
536 (Supplementary Fig. 13). The FWHM values from both XRD and PL decrease with increasing
537 the film thickness, indicating thicker films exhibit better crystal qualities. However, such
538 changes seem to plateau from ~20 μm, where there is almost no change with further increasing
539 the crystal thickness. To study the trap density, P-type devices have been fabricated with two Au
540 electrodes by e-beam evaporation. Devices with different single-crystal thicknesses are measured.
541 All samples are scanned under forward bias only with the same scan condition to avoid any
542 influence of hysteresis, and all samples are disconnected for 6 hours to avoid the polarization
543 influence from the previous scan to the next one[53]. The results also exhibit lower trap densities in
544 thicker devices, which correspond to an overall better crystal quality. Therefore, the calculated
545 carrier diffusion length shows a thickness-dependent phenomenon, which results from the

546 saturated carrier mobility and carrier lifetime because of the better crystal quality in thicker
547 single-crystal thin films.
548
549 **Supplementary Discussion 6: The in situ fabricated devices.**
550 Different from the spin coating technique for preparing polycrystalline perovskite thin films,
551 lithography steps have been carried in the growth/transfer process, so the nano/micro fabrication
552 process needs to be considered as an influencing factor on the device performance. Generally
553 speaking, the shape of the current density-voltage (*J-V*) curve can roughly tell the cell
554 performance. Large series resistance can influence the short circuit current density (J_{SC}), but in
555 that case, the shape of the curve is normally s-shaped. If the fill factor (FF) is moderate, the
556 series resistance should be acceptable. However, the FF and open circuit voltage (V_{OC}) do not
557 have a strong correlation. Relatively speaking, an FF greater than 75% can still have a low V_{OC}.
558 The V_{OC} is highly related to the bandgap and interfacial recombination. While the bandgap is the
559 same for all samples in this case, the interfacial recombination is sensitive to the surface defect
560 states.
561 Perovskite single crystals grown by wet chemical methods are found to have high surface
562 defect centers[22,23], which are orders of magnitude higher than those in polycrystalline films[52].
563 These surface defect states will mainly influence the *Voc*[54-61]. Even though many approaches
564 have been established to passivate the surface/interface defects in polycrystalline perovskite[62-65],
565 there is still a lack of strategy to passive single-crystal perovskites. Also, thinner devices have a
566 higher surface-to-volume ratio than thicker devices, and are thus more prone to operational errors
567 and easier to be influenced by the re-adhesion/re-growth and solution treatment (e.g., washed by
568 the GBL saturated solution). Evidence can be seen in Supplementary Fig. 15b and 15c, where

569 TPC and TPV measurements are used to qualify the carrier lifetime and mobility changes after
570 washing the single-crystal perovskite with different thicknesses by the GBL saturated solution. It
571 is clear that the crystal quality in a thinner film is more easily influenced by surface treatments.

572 Therefore, to isolate the influence of fabrication steps on the quality of the crystal
573 surface/interface and thus the V_{OC}, particularly of the thinner films, devices based on the single-
574 crystal perovskite film without transferring (i.e., delamination, re-adhesion, or GBL washing)
575 have been fabricated. These in situ fabricated devices are used to characterize the V_{OC}, which are
576 shown in the inset of Figure 2b. The configurations of these in situ fabricated devices are kept
577 the same as Au/poly(bis(4-phenyl)(2,4,6-trimethylphenyl)amine) (PTAA)/single-crystal
578 perovskite/TiO_2/ITO, where PTAA is the hole transport layer patterned by photolithography and
579 etching, TiO_2 is the electron transport layer deposited by atomic layer deposition, and Au and
580 ITO are both electrodes deposited by sputtering (Extended Data Fig. 3). In such a structure
581 where no solvent treatment is applied, the influence of the fabrication steps on the V_{OC} is
582 minimized. Also, because there is only one surface (top surface) that experiences the solution
583 treatment, the V_{OC} values resulted from the in situ fabricated devices are more accurate and
584 revealing. So, we can study the dependence of V_{OC} on the single-crystal perovskite thickness in a
585 more accurate way and exclude the influence of other confounding factors from fabrication steps.

586 In the *J-V* curves of Figure 2b, the increase of V_{OC} from ~0.6 to ~2 μm is considered to be
587 because thicker films have better crystal qualities and are more immune to the fabrication steps
588 induced degradation in crystal quality. The decrease of V_{OC} beyond 2 μm can be explained by the
589 inset of Figure 2b. Without extra re-growth and solvent treatments, the single-crystal thin film
590 can keep its original best surface quality. A thicker film leads to a lower V_{OC}, which is due to the
591 interfacial charge accumulation caused by the weaker build-in field in the thicker films. Note that

592 even though in situ devices use a different structure from the growth/transfer devices, as long as
593 the structure of all in situ devices is the same, the conclusion of studying the thickness-dependent
594 V_{OC} is valid.
595
596 **Supplementary Discussion 7: The neutral mechanical plane (NMP) design and mechanical**
597 **simulations.**
598 The NMP is defined as a conceptual plane within a beam or cantilever. When loaded by a
599 bending force, the beam bends so that the inner surface is in compression and the outer surface is
600 in tension. The NMP is the surface within the beam between these zones, where the material of
601 the beam is not under stress, either compression or tension. Therefore, if a critical material (layer)
602 of interest is sufficiently thin and can be located in/near the NMP, the generated strain in the
603 material will be diminishingly small. As such, this approach provides a means of rendering the
604 nominally brittle single-crystal perovskite as flexible (Extended Data Fig. 5a left).
605 To design such a structure, a result from a simple one-dimension (1D) bending is first
606 implemented to provide insights into this system (Extended Data Fig. 5a right)[66]:

607 $$h = \frac{d_1E_1A_1 + d_2E_2A_2 + d_3E_3A_3}{E_1A_1 + E_2A_2 + E_3A_3}$$

608 where h is the distance from the bottom of the system to the neutral plane, d is the distance from
609 the bottom of the system to the middle plane of each individual layer, E is the Young's modulus
610 of the given layer, and A is the cross-sectional area.
611 In this study, the thickness of the middle single-crystal $MAPbI_3$ is 2 μm, and the modulus is
612 14 GPa; the thickness of the bottom polyethylene terephthalate (PET)/ITO is 70 μm, and the
613 modulus is 2 GPa. Other device component materials, including ITO, SnO_2, and Spiro-MeOTAD
614 are not discussed here to simplify the model. In addition to these layers, we first design a top

615 layer with a suitable modulus and thickness to locate the NMP at the middle of the single-crystal
616 $MAPbI_3$ layer. For flexible or wearable devices, an overall small thickness is preferred for better
617 conformability with nonplanar surfaces and a smaller form factor. Therefore, a thin top layer in
618 the NMP structure is highly desired, which suggests that the top layer should have a modulus
619 similar to or larger than that of the PET/ITO. Here, we use a mixture of PDMS and 1-methoxy-2-
620 propanol acetate (SU8) to form such a top layer. The purpose of mixing SU8 into the PDMS is to
621 increase modulus of the top layer. The resultant modulus of the SU8/PDMS is measured to be
622 around 2.5 GPa.

623 Based on these values and using the above equation, to locate the NMP at the center of the
624 perovskite layer ($h = d_2$) requires a thickness of 62 μm for the top SU8/PDMS layer. Also, for the
625 entire structure (PET/ITO/SnO_2/single-crystal perovskite/Spiro-MeoTAD/Au/SU8-PMDS),
626 because of the small thicknesses and generally symmetric positions of other additional layers, the
627 calculated NMP is still near the center of the perovskite layer, which indicates the simplified
628 structure is reasonable. This model provides a quick and simple approach to the initial design of
629 the multilayer stacks, as to place the critical components (i.e., the single-crystal $MAPbI_3$ layer)
630 near the neutral axis, thereby reducing the levels of strain it experiences during bending.

631 Still, discrepancies may arise between experimental observations and predictions from the
632 1D model, due to Poisson effects and large deformations of the system not accounted for in this
633 simple 1D bending equation. As such, to better design the system, we analyzed the full three-
634 dimension (3D) mechanical response of this system.

635 The commercial software package ABAQUS enables simulating the full 3D mechanical
636 response of the single-crystal perovskite devices. The composite layer (SU8/PDMS, single-
637 crystal perovskite, and PET) consists of 8-node linear brick elements (C3D8H). The simulation

implements values of the elastic modulus of SU8/PDMS, single-crystal perovskite, and PET of 2.5 GPa, 14 GPa, and 2 GPa, respectively. The simulation also implements linear elastic constitutive models for each material but includes non-linear geometric effects (finite deformation) to enable large out of plane deformation. In the simulations, the largest value of the maximum principal strain is found to be near the edge of the single-crystal perovskite layer due to 3D and Poisson effects. Computing this maximum value of strain at the critical radius of curvature from the experiments (the one that induces fracture) allows for an estimation of the failure strain of perovskite materials[67] (Supplementary Fig. 17). For our tested/simulated system, this corresponds to a critical failure strain of ~0.36% for single-crystal perovskite layer, which suggests this layer itself is quite brittle. Again, however, the overall system exhibits good flexibility (maintaining mechanical integrity down to a bending radius of 2.5 mm) due to the NMP design.

Finally, we should note, that in using these simulations, a few assumptions are made that may not always be correct, depending largely on details of the fabrication process and the experimental testing procedure:

1. Boundary conditions: In the 3D simulations, all layers are ideally attached, i.e., no slip or de-bonding occurs. However, slip or de-bonding may occur during the experiments, e.g., if the fabrication procedure does not lead to strong bonding between layers.

2. Input force (moment): Unlike in the experiments, a moment is applied to the device in the simulation. As such, the resulting deformation in the simulation does not have a constant bending radius of curvature along the length of the specimen.

3. Material parameters: The fabricated device may exhibit different material properties than are used in the simulation (e.g., modulus of the perovskite). Likewise, the critical strain to cause

661 fracture may be different from what is reported (e.g., in the literature) and the actual material
662 used in the experiments.

663 The results in Figure 4c do exhibit a discrepancy between the NMP structure and the
664 completed device structure. Different from a bending radius of $r \sim 2.5$ mm in the NMP structure,
665 the entire photovoltaic device exhibits a noticeable efficiency decrease at $r \sim 3$ mm. This
666 difference in bending radius should be due to the influences introduced by the additional layers
667 in the photovoltaic device, including ITO, SnO_2, Spiro-MeOTAD, and Au, even though those
668 layers do not change much the overall NMP position of the single-crystal hybrid perovskite.

669

670 **Supplementary Discussion 8: Bandgap measurements and calculations.**

671 Ultraviolet photoelectron spectroscopy (UPS) measurements are carried out on graded
672 single crystals with different growth time. Because the graded single crystal growth is under
673 continuous solution exchanging, different growth time can result in different thicknesses and
674 surface compositions. Thus, the surface bandgap at different growth time can represent the
675 bandgap at different distances from the substrate interface of the graded bandgap single-crystal
676 thin film.

677 In the UPS measurements, He I (21.22 eV) is used as the radiation source. The position of
678 the electron affinity (Fermi level) *versus* vacuum is the difference between the high binding
679 energy cutoff (Fig. 3b inset) and the He I radiation energy (21.22 eV). The position of VBM is
680 the difference between the Fermi level and the low binding energy cutoff (Fig. 3b). Therefore,
681 the location of the valence band maximum (VBM) can be calculated from the UPS
682 measurements. Semi-log scale has also been plotted to double-check the cutting off positions[68,69],
683 which can be seen in Supplementary Fig. 23. In the semi-log scale, there are no noticeable small

intensities either, suggesting that the determination of the onset should be accurate. Additionally, we carefully measure the onset again to get accurate calculations of the VBM in the semi-log scale. We also compare the difference between the linear-scale and semi-log scale, and the difference between them in this case is negligible.

To obtain the full band structure, the bandgap value also needs to be measured for calculating the conduction band minimum (CBM). The bandgap values are measured via ultraviolet–visible spectroscopy (UV–vis) in the reflection mode (Fig. 3c) and PL (Supplementary Fig. 20a). Since the UV-vis light will penetrate deeper into the crystal than the He-I, the UV-vis measurement represents an averaged bandgap of the different compositions within the penetration depth. To precisely measure the bandgap of a single composition in the graded structure, we use the growth solution, with the same composition as the surface of the crystal at a particular growth time, to grow a single composition epitaxial single-crystal thin film. The calculated entire band structure is presented in Fig. 3c.

Supplementary Discussion 9: First-principles density functional theory (DFT) calculations.

Structural and electronic properties of $MAPb_{0.5+x}Sn_{0.5-x}I_3$ are calculated using first-principles density functional theory (DFT). A 2 × 2 × 2 supercell of tetragonal $MAPbI_3$ are built to model Sn-doped $MAPbI_3$, which contains a total number of 384 atoms with 32 Pb atoms. The Pb atoms are substituted by Sn to build the $MAPb_{0.5+x}Sn_{0.5-x}I_3$ supercells with x decreasing from $x = 0.5$ to $x = 0$ in 0.125 decrements. This yields a total number of five structures. These structures are fully optimized and used to calculate the density of states (DOS) and electronic band structures.

DFT calculations are carried out using the Vienna Ab Initio Simulation Package (VASP)[70].

The core-valence interaction is described by the Projector-Augmented Wave (PAW) pseudopotential. The electron-electron exchange-correlation function is treated using the Generalized Gradient Approximation (GGA) parametrized by Perdew, Burke, and Ernzerhof (PBE)[71]. The wave functions are expanded in a plane-wave basis set with a cutoff energy of 400 eV. All structures are fully optimized until all components of the residual forces are smaller than 0.03 eV/Å. The convergence threshold for self-consistent-field iteration is set at 10^{-5} eV. The Brillouin zone of the 384-atom supercells is sampled by the Γ point for optimization. A denser *k*-point mesh of 2 × 2 × 1 is used for the static run. Electronic band structures are calculated along with the high-symmetrical points of body-centered tetragonal lattice[72].

With the Sn substitution, the Sn-I bonds are obviously shorter than the original Pb-I bonds. Therefore, the cell volume shrinks as Sn concentration increases. Extended Data Fig. 7a shows the calculated electronic band structures for $MAPb_{0.5+x}Sn_{0.5-x}I_3$ with increasing the Sn composition. The VBM for each structure is normalized to zero point. All structures show direct bandgaps at the Γ point. The bandgap energies calculated with GGA decreases as the Sn composition increases. Although GGA is well-known to underestimate the bandgap energy, it correctly shows a trend (relative energy) among models with similar crystal structures and chemical compositions. Electron and hole effective masses are fitted near the band edges by:

$$\frac{1}{m_e^*} = \frac{1}{\hbar^2}\frac{\partial^2 E_C}{\partial k^2}$$

$$\frac{1}{m_h^*} = \frac{1}{\hbar^2}\frac{\partial^2 E_V}{\partial k^2}$$

where m_e^* is the electron effective mass, m_h^* is the hole effective mass, $\hbar$ is the reduced Planck constant, E_C is the conduction band energy, E_V is the valence band energy, and k is the wavevector. As shown in Extended Data Fig. 7b, m_e^* barely changes, while m_h^* decreases as the

Sn concentration increases. This trend is obvious where the valence band becomes more dispersive from x = 0.5 to x = 0. The results indicate a smaller hole mobility as the Sn concentration increases in $MAPb_{0.5+x}Sn_{0.5-x}I_3$.

Further, to analyze the changes of band edges as a function of the Sn composition, we align DOS for the five $MAPb_{0.5+x}Sn_{0.5-x}I_3$ structures to Hydrogen 1s state in MA molecules. Because the discrete energy level of the hydrogen atom in MA molecules is highly independent on the band edge-derived states, the Hydrogen 1s state in MA molecules can be used as an energy reference to determine relative positions of band edges. In this case, the VBM continuously increases while the CBM barely changes as the Sn concentration increases (Extended Data Fig. 7c). This trend is in good agreement with our experimental results and indicates that the decrease of the bandgap as the Sn concentration increases is mainly induced by the increase of VBM.

Supplementary Discussion 10: Improved performance by the graded band structure.

To explain possible reasons for the enhanced performance in bandgap-graded single-crystal $MAPb_{0.5+x}Sn_{0.5-x}I_3$ photovoltaics, several experiments have been designed. The main reasons are found to be the enhanced J_{SC} and relatively high V_{OC}.

For the J_{SC}, it is due to the Sn doping, which results in reduced bandgap and exciton binding energy in comparison with the $MAPbI_3$[73,74]. Both the light absorption range and the excited carrier concentration in the $MAPb_{0.5+x}Sn_{0.5-x}I_3$ get enhanced, which leads to an enhanced output current. This phenomenon is reflected by the electron-beam-induced current (EBIC) and external quantum efficiency spectra (EQE) measurements. From the EBIC results, uniform current intensities exist in the $MAPbI_3$ and $MAPb_{0.5}Sn_{0.5}I_3$ while a gradient current intensity is measured in the $MAPb_{0.5+x}Sn_{0.5-x}I_3$. The reduced current in the Pb area is due to a broader bandgap and a

752 higher exciton binding energy. The uniform current intensity distribution in the single-crystal
753 $MAPbI_3$ and compositionally uniform $MAPb_{0.5}Sn_{0.5}I_3$ also serves as additional evidence for the
754 absence of twins or small angle grain boundaries during the expanding/merging growth process.
755 From the EQE measurements, the larger absorption range and higher current density of the
756 $MAPb_{0.5+x}Sn_{0.5-x}I_3$ than the $MAPbI_3$ indicate that the Sn doping decreases the bandgap and
757 therefore enhances the EQE.

758 For the V_{OC}, it is related to the bandgap and the recombination in a particular photovoltaic
759 structure[75-77]. Sn doping normally largely decreases the V_{OC} of the photovoltaics because of the
760 decreased absorber bandgap[73,78]. However, the V_{OC} in the $MAPb_{0.5+x}Sn_{0.5-x}I_3$ photovoltaics is
761 only slightly decreased from that of the $MAPbI_3$. To investigate the possible reason of the high
762 V_{OC} of $MAPb_{0.5+x}Sn_{0.5-x}I_3$, the carrier mobility and lifetime have been studied by ToF and TPV,
763 respectively. For the carrier mobility, it's clear to see that the mobility of the $MAPb_{0.5+x}Sn_{0.5-x}I_3$
764 has been improved to as high as that of the $MAPb_{0.5}Sn_{0.5}I_3$ (Fig. 3f inset), which is because of the
765 high intrinsic mobility in Sn-based hybrid perovskite[78]. For the carrier lifetime, even though
766 doping the Sn to Pb perovskite in a uniform composition single crystal normally largely
767 decreases the lifetime, the graded Pb-Sn single crystal exhibits a relatively long lifetime among
768 the three single crystals (Fig. 3f). Given the same (Au/single-crystal perovskite/ITO) device
769 structure in the measurements, such a large carrier lifetime in the $MAPb_{0.5+x}Sn_{0.5-x}I_3$ is because of
770 the graded bandgap of the $MAPb_{0.5+x}Sn_{0.5-x}I_3$. In the EBIC mapping in Fig. 3d, the interfacial
771 region of graded $MAPb_{0.5+x}Sn_{0.5-x}I_3$ (within ~20 nm from the interface with the substrate, whose
772 composition is very close to $MAPb_{0.5}Sn_{0.5}I_3$, see Supplementary Figure 27) always gives a higher
773 current signal than the compositionally uniform $MAPb_{0.5}Sn_{0.5}I_3$, which also suggest a lower local
774 recombination rate.

775 Compared with the typical absorber band structure, the graded band structure can have a
776 positive influence on the carrier transport: we can divide the graded bandgap into innumerable
777 individual bandgaps of an innumerable series of heterojunctions connected back to back. Each
778 individual junction serves two functions: a light absorber and an ETL/HTL for its neighboring
779 junctions. The latter function is absent in a typical single composition absorber. The
780 recombination possibility of as-generated charge carriers in the absorber is largely
781 suppressed[79,80], which leads to a relatively high V_{OC} in the $MAPb_{0.5+x}Sn_{0.5-x}I_3$ photovoltaics.
782

783 **Supplementary Discussion 11: Improved bending stability of the single-crystal**
784 **photovoltaics.**

785 Researches have already studied the mechanical properties of perovskite in both
786 polycrystalline and single-crystal structures[67,81-85]. Even though both are considered to be brittle,
787 the modulus in the polycrystalline perovskite is founded to be slightly higher than that in the
788 single-crystal perovskite[86], which may be because of the anisotropic mechanical properties in
789 single crystals[87,88]. Therefore, single-crystals perovskite with smaller modulus promises better
790 integration with the human body for wearable applications.

791 So far, the stability issue has been considered to be the most critical factor in hindering
792 applications of perovskite devices[89-91]. Different from the polycrystalline structure in most of the
793 current perovskite devices, the single-crystal structure has proved to have much better stabilities.
794 In polycrystalline perovskite, O_2 and moisture can easily go through the entire thickness of the
795 layer from the innumerable grain boundaries to react with the perovskite and degrade the device
796 performance[92,93]. Polycrystalline perovskite devices have been widely studied for years, but their
797 intrinsic stability problems are still not solved. Grain boundaries also contribute to a higher

defect density, a stronger carrier recombination, and an easier ion migration[94-100]. In flexible devices, multiple-time bending can inevitably deteriorate the grain boundaries, potentially increasing the charge transfer barrier and carrier recombination rates, and accelerating material degradation[97,99,101-103]. However, grain boundaries are absent in single-crystal perovskites, suggesting that flexible devices made of single-crystal perovskites may exhibit enhanced device lifetime and stability.

This hypothesis is tested and confirmed by experimental data. Polycrystalline photovoltaics show significant performance degradation under the same cyclic bending tests (Supplementary Fig. 31), which may be caused by fast material and device degradation at the grain boundaries during bending. Single-crystal devices of the same device configuration exhibit much better stabilities under cyclic bending tests, indicating noticeable advantages of flexible devices based on single-crystal perovskites.

To further prove this conclusion, cycling-dependent material properties have been studied by using XRD ω scan and lateral current -voltage (I-V) characterizations (Supplementary Fig. 32). The size of polycrystalline and single-crystal films, and the two Au electrodes deposited by e-beam evaporation, are fixed to be the same for all devices. Lateral conductivity of the polycrystalline film after 300-time bending at a radius of 5 mm decreases to be only 31.1% of the intact one. In contrast, lateral conductivity of the single-crystal film still maintains 83.7% of the intact one, indicating a lower charge transfer barrier in the single-crystal film generated by the cyclic bending. XRD ω scan results support this conclusion. The FWHM of the polycrystalline film after bending becomes larger while the peaks from the single-crystal film does not change noticeably, which evidently indicates that single-crystal thin films are more resistant to fatigue. Consider the same operational conditions, such a difference is attributed to the deteriorated grain

821 boundaries (increased series resistance) and the degraded materials (e.g., impurities, ion
822 migration, and decomposition) in the polycrystalline thin film in comparison to the single-crystal
823 film.

824 Considering the high intrinsic structural defects and the instability issue of polycrystalline
825 perovskite, replacing polycrystalline films with single-crystal films for flexible devices may
826 provide a way for better device performance and longer device lifetime.

827

828 **Supplementary Discussion 12: Photovoltaic device performance tests.**

829 Each single-crystal photovoltaic device (0.5 cm × 0.5 cm) in the array is individually
830 measured with a shadow mask. If not specified, all tests are using one $MAPb_{0.5+x}Sn_{0.5-x}I_3$ single-
831 crystal photovoltaic device in the array without bending. The device in the center of 5 by 5 array
832 is selected to do all of the measurements. The polycrystalline photovoltaic devices are also
833 coated with SU8/PDMS top layers for fair comparisons. All tests (except the stress stability tests)
834 are under constant 1-Sun from a standard solar simulator source with air mass 1.5 global filters.
835 A 10 min light soaking is applied to all of the measurements. A small desktop fan is used to
836 dissipate the heat generated by illumination.

837 In the stability comparison tests between the single-crystal and polycrystalline photovoltaics
838 (Fig. 4d-4f), two compositionally uniform polycrystalline films (i.e., $MAPbI_3$ and
839 $MAPb_{0.5}Sn_{0.5}I_3$), and a graded Pb-Sn single-crystal film are used, because there is currently no
840 method to deposit graded polycrystalline films. We adopt the same HTL/ETL contact interfaces
841 for the polycrystalline photovoltaics as the graded single-crystal photovoltaics, because the
842 interfaces are paramount in photovoltaic device performance and stability[30,104]. For the thermal
843 stability, the devices are all completed with PET and PDMS encapsulation. Then, the devices are

844 placed into an oven for aging. Because all devices are encapsulated, the humidity condition
845 should not be an influential factor. The aging time for the thermal tests is two hours. For the
846 humidity tests, the devices are not encapsulated, and the aging time is 30 mins because otherwise
847 the oxidation of Sn^{2+} can rapidly dominate the degradation mechanism.

848 The humidity control can be realized by calculation from the water vapor pressure
849 according to the thermodynamic equilibrium with condensed states, which can be controlled by
850 adjusting the amount of water in the air in a sealed space. The saturated water vapor pressure
851 look-up table is used to calculate the needed amount of water for different humidity at a certain
852 temperature, which can be applied to control the relative humidity. A glass box is used as the
853 confined space, where different amounts of water are added. Then, the box is placed into an oven
854 to keep the temperature to be 30℃ until the water is fully evaporated. In this way, the relative
855 humidity in the glass box can be designed accurately at different levels. For example, from the
856 look-up table, the saturated vapor pressure of water under 30 ℃ can be found to be 0.0042 MPa,
857 which means that at 30 ℃, 100% relative humidity refers to a partial pressure of water vapor of
858 0.0042 MPa. Therefore, the volume ratio of water vapor is 4.2%. If the relative humidity is 70%,
859 the total volume of water vapor in a container of 1 m^3 size will be 4.2% × 70% × 1000 = 29.4 L,
860 which is 21.0 g (according to the condition at 30 ℃). In our study, we need to add 0.00265 g
861 water (2.62 μl) into a 125 cm^3 glass box to achieve a 70% humidity. Similarly, if the relative
862 humidity is 30%, the total volume of water in 1 m^3 container will be 4.2% × 30% × 1000 = 12.6
863 L, which is 9.0 g (according to the condition at 30 ℃), and the amount of the water we need to
864 add to a 125 cm^3 glass box will be 0.00114 g (1.12 μl). In the experiments, to avoid additional
865 background humidity from the natural environment before the experiment, the glass box will be

placed into an oven at 100 ℃ for overnight to create a dry environment. A portable commercial humidity sensor is attached to the internal wall of the glass box for calibration purposes.

For the long-time stability tests, all of the devices are stored in a dark dry box for monthly measurements.

Supplementary Discussion 13: Stability of the single-crystal photovoltaics in continuous JV measurements.

Maximum power point tracking under continuous 1-sun illumination has been performed to study the device stability. A small desktop fan is used to dissipate the heat generated by illumination. The results are summarized in Extended Data Fig. 10.

From the measurement results, all devices show a relatively rapid degradation during the first 100 hours, followed by steady degradation rates. In contrast to the shelf-stability in the Figure 4f, where the single-crystal devices are much more stable than the polycrystalline devices, continuous illumination tests show similar degradation rates among these devices, even though the single-crystal structure has better material stability against moisture, heat, O_2, and strong light intensity (Figure 4d, 4e, Extended Data Fig. 9, and Supplementary Figs. 34, 35, 41). Additionally, continuous illumination tests can easily degrade the device performance even within a short time by comparing it with the shelf-stability test (Figure 4f). Therefore, the major degradation mechanism under continuous illumination may not be from the perovskite material, but from the Spiro HTL layer. Even though a small fan is used, the continuous illumination tests can still generate a lot of heat, which accelerates the degradation of the Spiro molecules with thermal and light instability[105-107]. The Spiro material becomes the bottleneck for the device stability, rather than the perovskites.

Therefore, the Spiro has been replaced with PTAA for the continuous illumination tests again. Device performance using PTAA is not comparable with that using Spiro. Although the V_{OC} is moderate (average ~1.01 V), the FF (average ~0.68) and the current density (average ~19-20 mA cm^{-2}) of PTAA based devices are always lower than those of Spiro based devices. Normalized power conversion efficiency (PCE) shows a fair comparison among these PTAA based devices (Supplementary Fig. 36). After replacing the Spiro with PTAA, the differences among those curves are more pronounced, because the HTL becomes less of a bottleneck for the device stability. The single-crystal devices exhibit a much slower degradation rate than those of the polycrystalline devices, indicating that the single-crystal structure has a better stability than the polycrystalline structure. Given the same device structure and the same ETL/HTL, such differences in the stability between single-crystal and polycrystalline devices are considered to be from the reduced ion migration in single crystals[108]. Unlike conventional photovoltaic materials, perovskites are appreciable ionic solids, which can be directly reflected by continuous *I-V* or *J-V* measurements. The ion migration has been shown to contribute to the degradation of perovskite photovoltaics[109], even though the exact mechanisms are still debatable[110]. For example, reactions between HTL/ETL layers and migrating I^- can cause barriers for carrier injection that quickly decreases the device performance[111]. The ion migration can also lead to the formation of a local electric field in the perovskite material to deprotonate the organic cations[112]. Theoretical calculations predict activation energies of between 0.08 and 0.58 eV for the migration of I^-, between 0.46 and 1.12 eV for MA^+, and between 0.8 and 2.31 eV for Pb^{2+}, respectively[113-115]. Both anions (I^-) and cations (MA^+, Pb^{2+}) can migrate due to the presence of vacancies, interstitials, and anti-site substitutions[116]. However, because levers of those defects

are lower in the single-crystal perovskite than the polycrystalline perovskite, such ion migration and thus device degradation are largely suppressed[95].

Supplementary Discussion 14: Stability differences between single-crystal Pb-Sn photovoltaics and polycrystalline Pb-Sn photovoltaics.

Usually, excessive Sn in Pb-Sn perovskite can significantly lower the V_{OC}[117], switch the Sn^{2+} oxidation routes[118], and decrease the decomposition enthalpies to accelerate the material degradation. The oxidative tendency of Sn^{2+} to Sn^{4+} in Sn-based perovskite can rapidly degrade the device as typically seen in the polycrystalline $MAPb_{0.5}Sn_{0.5}I_3$ devices. In this work, the single-crystal $MAPb_{0.5+x}Sn_{0.5-x}I_3$ devices show much better stability than the polycrystalline devices. Several possible reasons for the slower oxidation rate from Sn^{2+} to Sn^{4+} in the single crystal are discussed below.

1. Encapsulation

The device is fully encapsulated in the glove box by both top and bottom polymer layers (PET and PDMS/SU8). Those polymers serve as not only strain releasing layers for enhancing the flexibility, but also as encapsulation layers for keeping the material away from O_2 and moisture. The encapsulation may be the most important reason for inhibiting the Sn^{2+} oxidation.

2. Mixed Pb-Sn system

In contrast to the pure Sn-based perovskite photovoltaics, replacing Sn with 50−85% of Pb produces PCEs ranging from 12 to 17% and moderate stability[118-123]. Even though the exact mechanism is still not very clear, one possible explanation has recently been proposed: the oxidation mechanism in the Pb-Sn system is different from that in the pure Sn system[118,123-125]. In pure Sn-based perovskites, the main oxidation product is SnO_2 and SnI_4. However, by

934 incorporating Pb into Sn-based perovskites, the oxidation proceeds in a different route, and the
935 main I-containing product becomes I_2 rather than SnI_4 in the case of the pure Sn system.

936 The formation of SnI_4 and SnO_2 involves the cooperative action of several Sn-I octahedra,
937 where the I ions bonded to one Sn cation can be transferred onto adjacent Sn cations with which
938 the I was shared. Pb, however, cannot be easily oxidized to Pb^{4+} and is unlikely to form PbI_4.
939 Hence, if many of the Sn sites are occupied by Pb, the cooperative mechanism is far less
940 favorable. Instead, I_2 is formed, and this requires three times as many Sn−I bonds to be broken,
941 which can be expected to be slow. Therefore, the surrounding Pb atoms can stabilize Sn^{2+} and
942 slow down its oxidation. Such an effect will be more pronounced when the percentage of Pb
943 atoms is higher.

944 Both experimental and theoretical studies have been carried out to further understand the
945 improved stability in Pb-Sn single-crystal perovskites. Absorption measurements on Pb-Sn based
946 single-crystals and purely Sn-based single-crystals after one-day stress aging under 100 ℃ are
947 used to understand the oxidation product as well as the chemical degradation route. The samples
948 are dissolved into the GBL solution. The results are in Supplementary Fig. 38. The degradation
949 products for $MASnI_3$ and $MAPb_{0.5}Sn_{0.5}I_3$ are very different: the compound for purely Sn-based
950 perovskite is SnI_4, while that of the lead-containing compound is I_2. The measured different
951 oxidation products in those two perovskite systems can be explained by different oxidation
952 reaction routes[118]:

953 $$MA(Pb:Sn)I_3 + (n_1)O_2 = (n_2)MAI[g] + (n_3)SnO_2 + (n_4)PbI_2 + (n_5)I_2[g] \quad (1)$$

954 $$MA(Pb:Sn)I_3 + (n_1)O_2 = (n_2)MAI[g] + (n_3)SnI_4[g] + (n_4)SnO_2 + (n_5)PbI_2 \quad (2)$$

955 In the purely Sn-based perovskite, because of the strong SnI_4 signal in the absorption
956 spectrum, the oxidation mechanism is more likely to be the reaction (2). The reaction (1) is
957 considered to be the mechanism for the Pb-Sn perovskite.

958 To double confirm this conclusion, we also calculate the decomposition enthalpies in both
959 reactions with different Pb to Sn ratios. From the calculation results (Supplementary Fig. 39),
960 reaction (1) is energetically more favorable than reaction (2) for the Pb-Sn perovskite at any Pb
961 to Sn ratios, indicating that the Sn^{2+} oxidation naturally prefers to happen through reaction (1),
962 where all of the Sn-I bonds need to be broken. Therefore, compared with the purely Sn
963 perovskite, the breaking of Sn-I bonds in the Pb-Sn perovskite is much slower, suggesting that
964 the Pb inclusion can make Sn^{2+} oxidation slower in the perovskite.

965 To triple confirm the conclusion, x-ray photoelectron spectroscopy (XPS) measurements
966 have been used to study the Sn^{2+} to Sn^{4+} ratio in perovskites to qualify the oxidation speed of
967 Sn^{2+} (Supplementary Fig. 40). Increasing Pb can dramatically inhibit the oxidation speed of Sn^{2+}
968 in the single-crystal perovskites, which serves as additional evidence for supporting the different
969 oxidation mechanisms between purely Sn and Pb-Sn based perovskites. What's more, we
970 dissolve $MAPb_{0.5+x}Sn_{0.5-x}I_3$ single crystals in GBL and use the solution to prepare the
971 polycrystalline thin film to reveal its composition. By studying the Sn^{2+} to Sn^{4+} ratio using XPS,
972 the Sn ratio should be between 0.2 to 0.3, where the oxidation speed is considered to be much
973 slower than the purely Sn-based perovskite.

974 3. Single crystal.

975 The single-crystal structure is also a major reason for the improved stability, which has been
976 widely proved to have much better stability in solar cells and photodetectors[16,23,126-128]. First,
977 single-crystal perovskites have much lower defect densities than their polycrystalline structures.

978 I_2 is believed to be the most critical by-product and will cause self-degradation[129]. The formation
979 of I_2 requires ion migration facilitated by structural defects. The well-align lattice structure of
980 single crystals provide much lower possibilities for the formation of I_2.

981 Second, there is no grain boundary in single crystals, which indicates that the reaction
982 routes are heavily inhibited. For the Sn-based polycrystalline perovskite, O_2 can relatively easily
983 go through the entire layer via the innumerable grain boundaries. The degradation routes can not
984 only come from the self-doping of Sn^{4+}, but also from the grain boundaries facilitated Sn^{2+}
985 oxidation in the entire layer. However, in the single-crystal structure, the O_2 can only react with
986 the single crystal surface, and only the formed Sn^{4+} and other impurities can further drive the
987 degradation by self-doping from the surface to the bulk parts. Comparing these two oxidation
988 approaches, we think the self-doping oxidation will be much slower than the direct reaction with
989 O_2. Due to the cutoff of the O_2 oxidation route, the degradation rate in single-crystals is highly
990 inhibited.

991 To test this hypothesis, both single-crystal $MAPb_{0.5}Sn_{0.5}I_3$ and polycrystalline
992 $MAPb_{0.5}Sn_{0.5}I_3$ have been measured by XPS. The samples are all prepared in a glove box and are
993 aged under the same environment outside the glove box. The measured results show that the
994 fresh polycrystalline $MAPb_{0.5}Sn_{0.5}I_3$ exhibits strong Sn^{4+} peaks (Supplementary Fig. 41).
995 Oxidation may have happened during sample transfer and loading. On the other side, the single-
996 crystal $MAPb_{0.5}Sn_{0.5}I_3$ sample shows negligible Sn^{4+} peaks, indicating that the oxidation speed in
997 the single-crystal sample is much slower than that in the polycrystalline. Therefore, the
998 innumerable grain boundaries in the polycrystalline provide direct pathways for the O_2 to react
999 with the Sn^{2+}. However, in the single-crystal, only the surface part can be oxidized by the O_2,

1000 and further oxidation of the bulk parts more depends on self-doping, which is much slower than
1001 the direct O_2 oxidation.

1002 What's more, *in-situ* XPS depth profile studies by ion milling have also been carried out to
1003 further understand the difference between single-crystal $MAPb_{0.5}Sn_{0.5}I_3$ and polycrystalline
1004 $MAPb_{0.5}Sn_{0.5}I_3$ (Extended Data Fig. 9). In the single-crystal sample, the Sn^{4+} is mainly formed at
1005 the surface of the single crystal, and the deeper bulk parts still keep Sn^{2+}. However, in the
1006 polycrystalline, even though the Sn^{4+} ratio in deeper bulk parts is reducing, the oxidation speed is
1007 much higher than that in the single-crystal.

1008 To summarize, the rapid oxidation of Sn^{2+} in polycrystalline perovskites is because of the
1009 existence of grain boundaries, which provide a direct pathway for the O_2 to diffuse through the
1010 entire material. Because of the high-quality crystal structure, single-crystal perovskites do not
1011 have those direct oxidation pathways, and the self-doping mechanism is determining the
1012 oxidation rate, which is much slower than reacting with the O_2.

1013

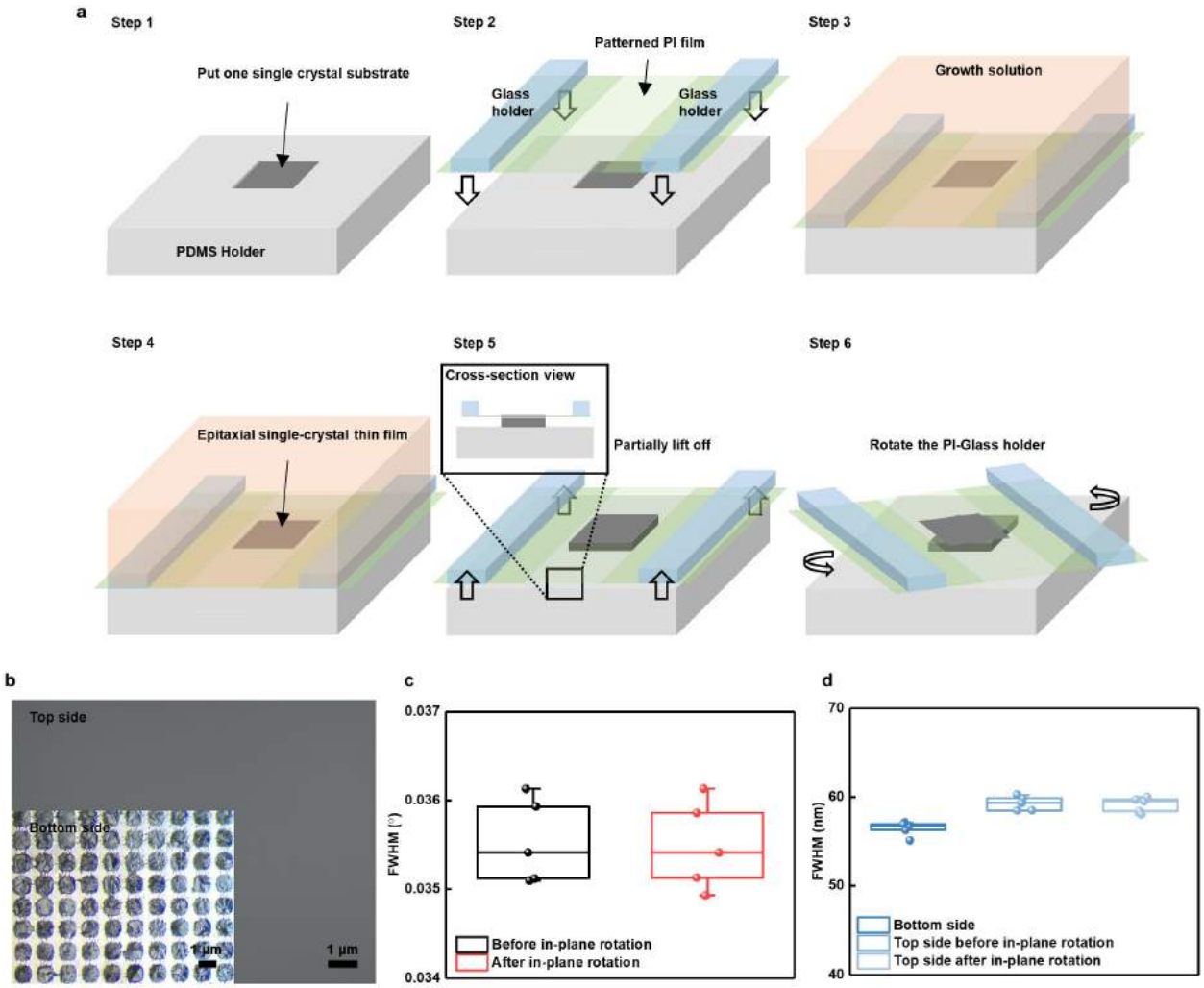

Supplementary Fig. 1 | The growth/transfer process and quality studies of detached single-crystal $MAPbI_3$ thin films. a, detailed schematics of the growth/transfer process. Critical components in each step are labelled. **b**, Optical images show the single-crystal $MAPbI_3$ after in-plane rotation. The inset image shows the bottom surface with the PI mask, where the broken micro-rods can be clearly seen. FWHM results from **c,** XRD ω scan and **d,** PL measurements of the single-crystal $MAPbI_3$ before and after in-plane rotation.

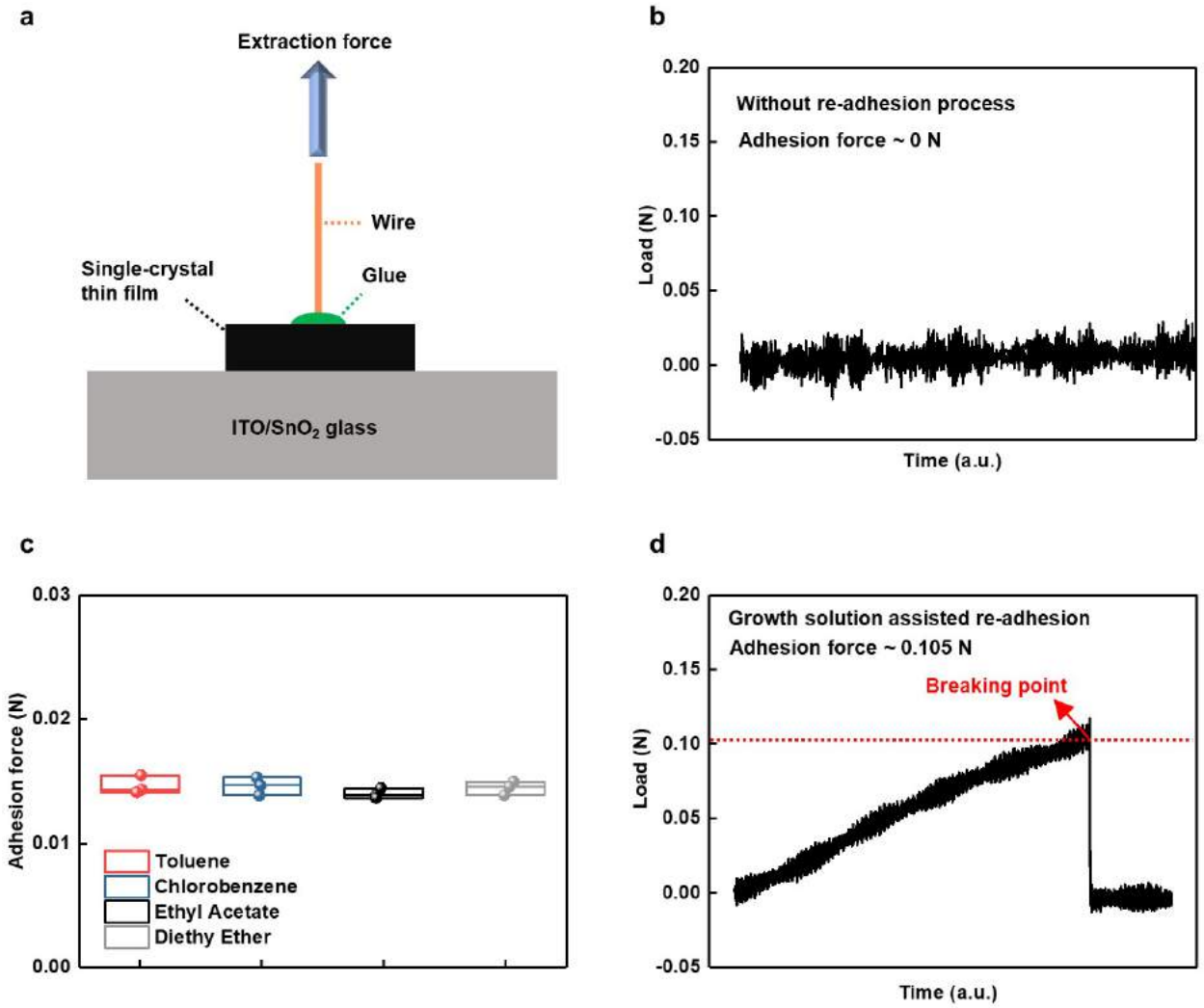

Supplementary Fig. 2 | The adhesion force measurement. a, The schematic testing setup for the adhesion force measurement. A Cu wire is fixed onto a single-crystal thin film for applying an external force. **b**, No adhesion force can be measured without a solvent-assisted re-adhesion process. **c**, Commonly used antisolvents for preparing hybrid perovskites are tested in the transferring process. No obvious difference in the adhesion force to the substrate can be observed, which are all relatively weak. **d**, For the growth solution assisted re-adhesion, delamination happens when the external load reaches ~0.105 N, which indicates good interfacial contact.

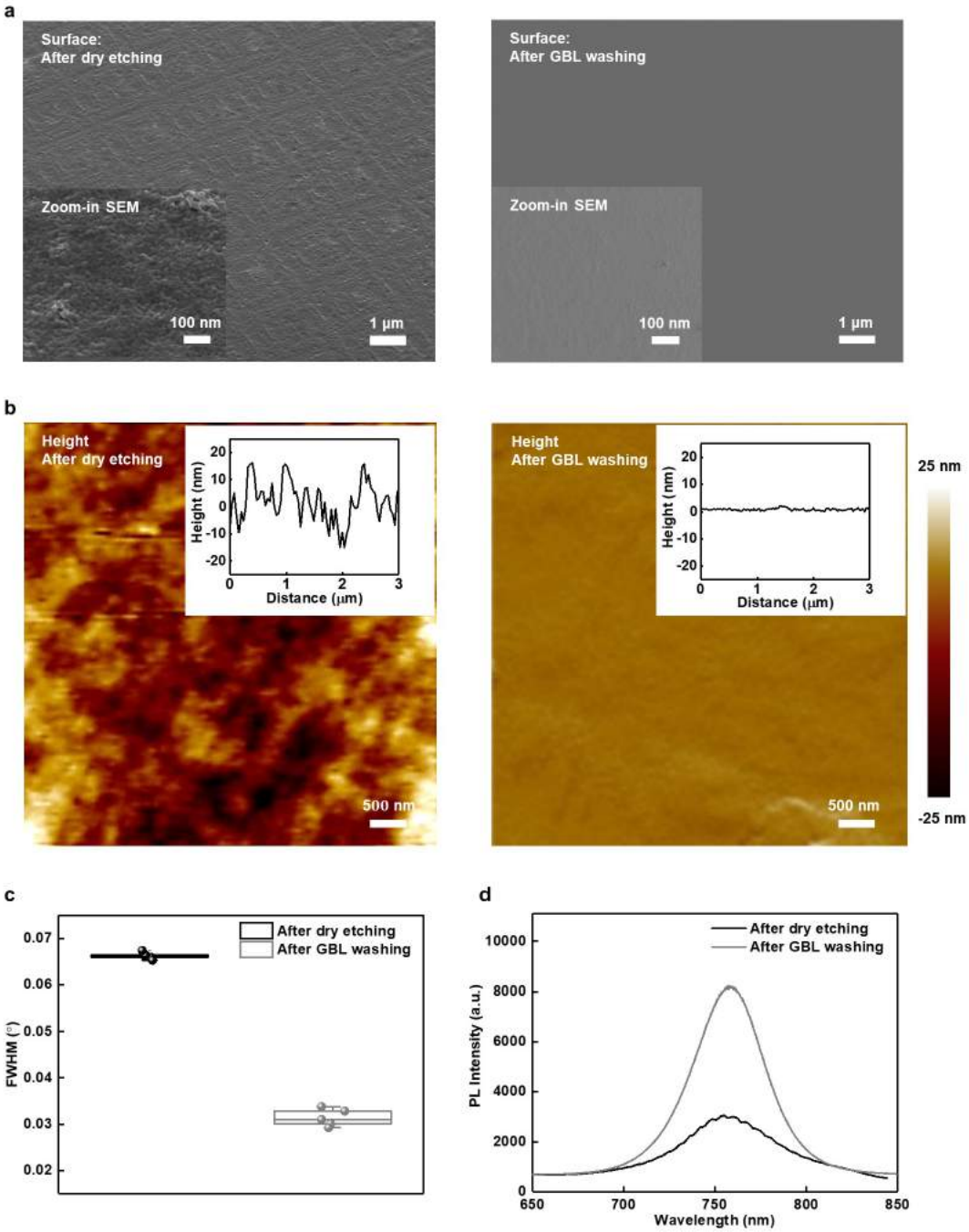

Supplementary Fig. 3 | Surface characterization of the crystals after etching and GBL washing. a, SEM images showing the crystal surface after dry etching and after GBL washing. The rough surface caused by dry etching can be fully removed by GBL washing. **b**, AFM measurement results of a transferred single-crystal $MAPbI_3$ surface before and after GBL washing. The rough surface caused by dry etching can be effectively smoothed by GBL washing. **c**, XRD ω scan measurements showing the huge difference before and after the washing, indicating that dry etching can cause serious damage to the crystal quality. **d,** PL measurements also reveal the same phenomenon, where the unwashed crystal shows a much weaker PL intensity and a broader peak.

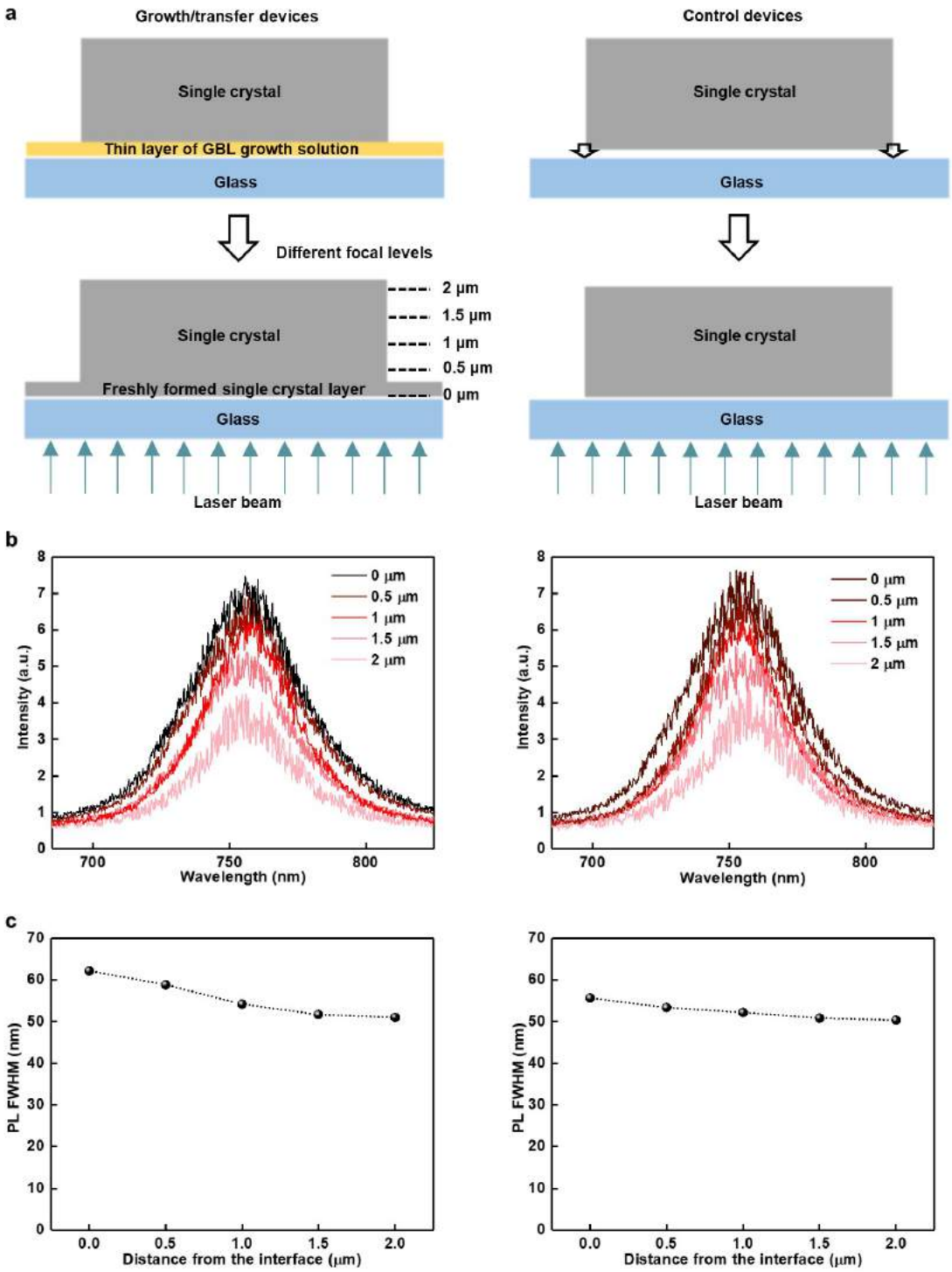

Supplementary Fig. 4 | Thickness-dependent PL measurements. a, Schematic setups of characterizing the growth/transfer and the control devices. **b**, The PL measurement results of the growth/transfer and control devices. **c**, The fitted FWHM results of both devices indicating that there is slight degradation of the crystallinity in the growth/transfer device because of the impurities and defects introduced during the re-growth process, which can potentially be improved by interfacial passivation.

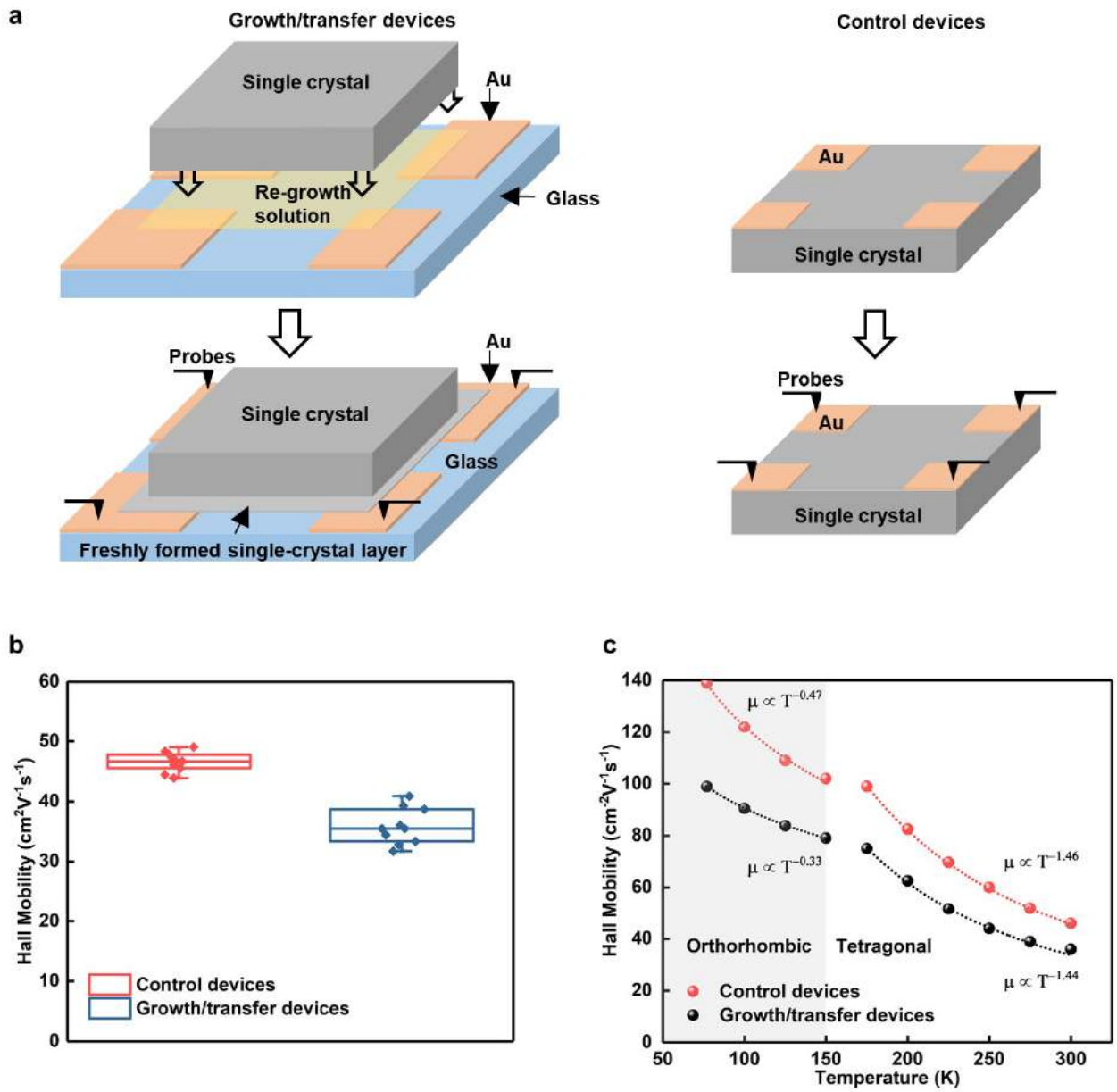

Supplementary Fig. 5 | Interfacial Hall mobility measurements. a, Schematic setups of the growth/transfer and control devices. **b**, Interfacial Hall mobility results showing that the growth/transfer devices have slightly lower mobilities and larger measurement variations compared with the control devices. **c**, Temperature-dependent interfacial Hall mobility measurement showing a noticeable difference in power exponents (~-0.33) for the growth/transfer devices compared with the control devices (~-0.47) under low temperatures, which can be attributed to the increased interfacial impurity scattering of the growth/transfer devices.

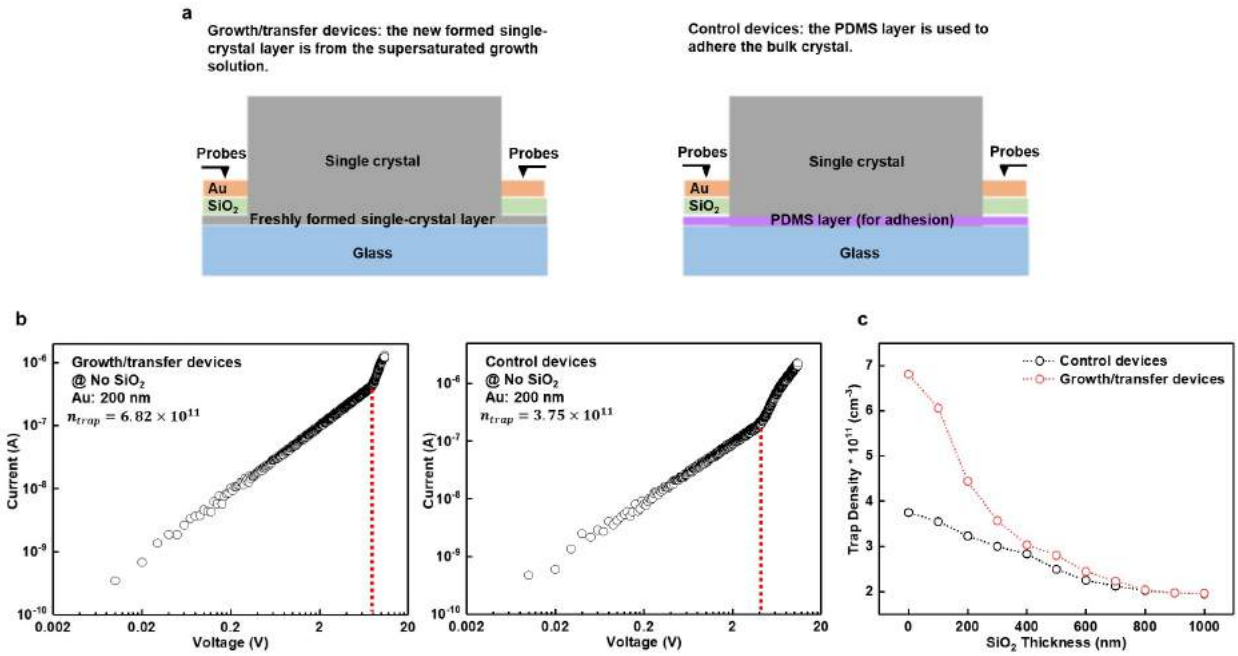

Supplementary Fig. 6 | Interfacial trap density measurements. a, Schematic setups. **b**, The calculated trap densities at the interfaces of the growth/transfer and control devices. **c**, Interfacial trap density results showing that the growth/transfer device has a higher trap density close to the interface than that distant from the interface.

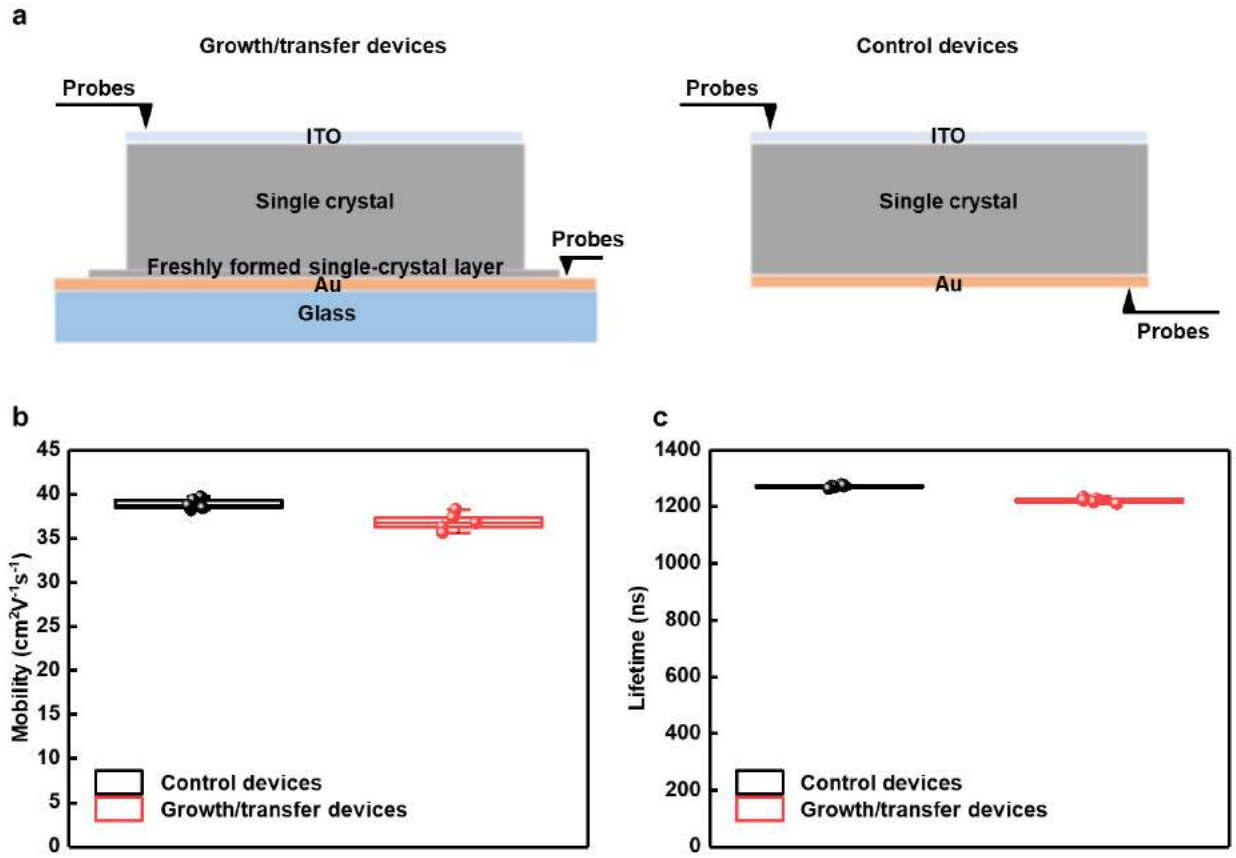

Supplementary Fig. 7 | TPC and TPV measurements. a, Schematic setups. **b**, TPC measurements showing that the growth/transfer devices have slightly lower mobilities compared with the control devices. **c,** TPV measurements showing that the growth/transfer devices have slightly shorter lifetimes compared with the control devices. Those results illustrate that the re-growth process can slightly decrease the electronic properties of the crystals (~4-5%).

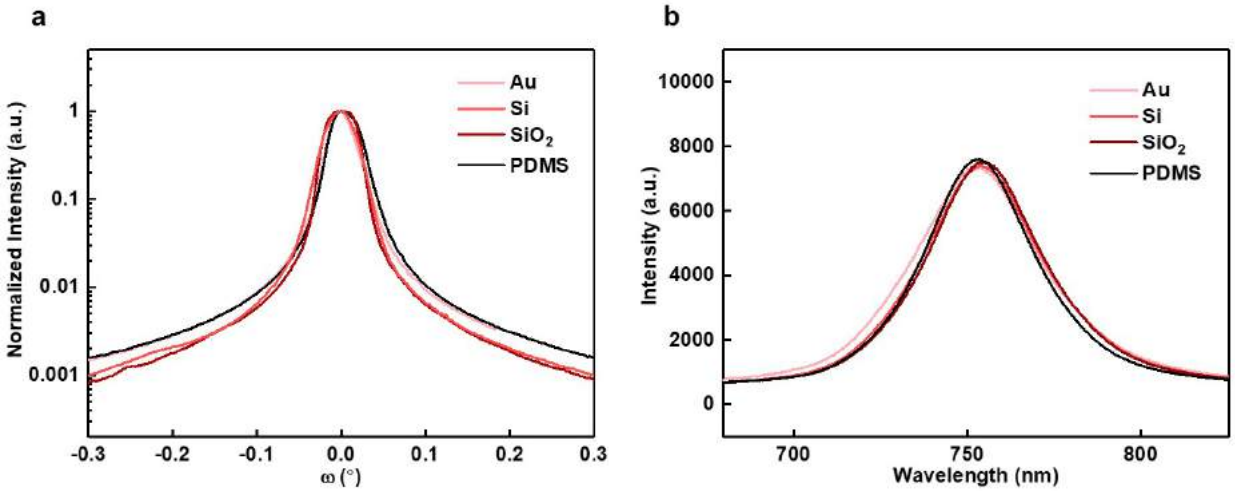

Supplementary Fig. 8 | Substrate-dependent interfacial crystal quality characterized by XRD and PL measurements. a, XRD ω scan with transferred single-crystal $MAPbI_3$ on different substrates. **b**, PL measurements with transferred single-crystal $MAPbI_3$ on different substrates. Both kinds of measurements do not show obvious difference among different substrates, indicating the crystal quality is substrate-independent.

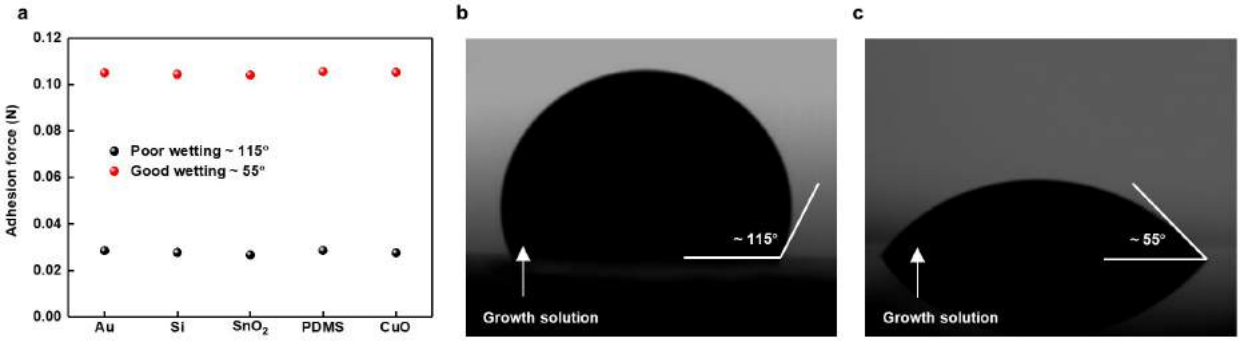

Supplementary Fig. 9 | Adhesion force and contact angle measurements. a, Measured adhesion force between the transferred single-crystal $MAPbI_3$ and different substrates with good and poor wetting conditions. Good wetting can always give a strong adhesion force regardless of the substrate. Contact angle measurements on an Au surface after being treated by UV-Ozone for **b**, 2 min and **c**, 10 min. By controlling the surface treatment, the wetting conditions and contact angles can be well controlled.

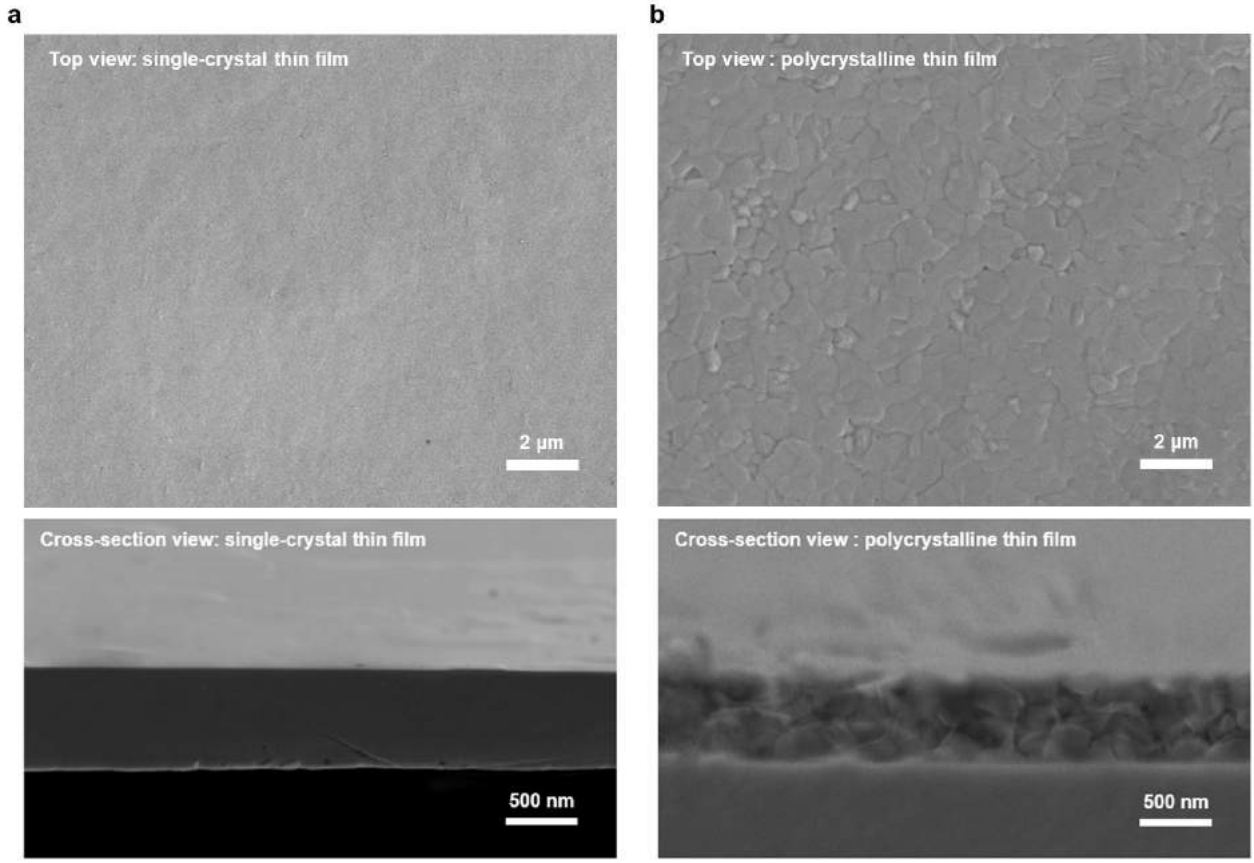

Supplementary Fig. 10 | Close-up views of the single-crystal and polycrystalline $MAPbI_3$. a, SEM images of the single-crystal $MAPbI_3$ thin film (top) from the top and (bottom) from the cross-section views, where no grain boundary can be seen, which is qualitatively different from the polycrystalline structure in **b**.

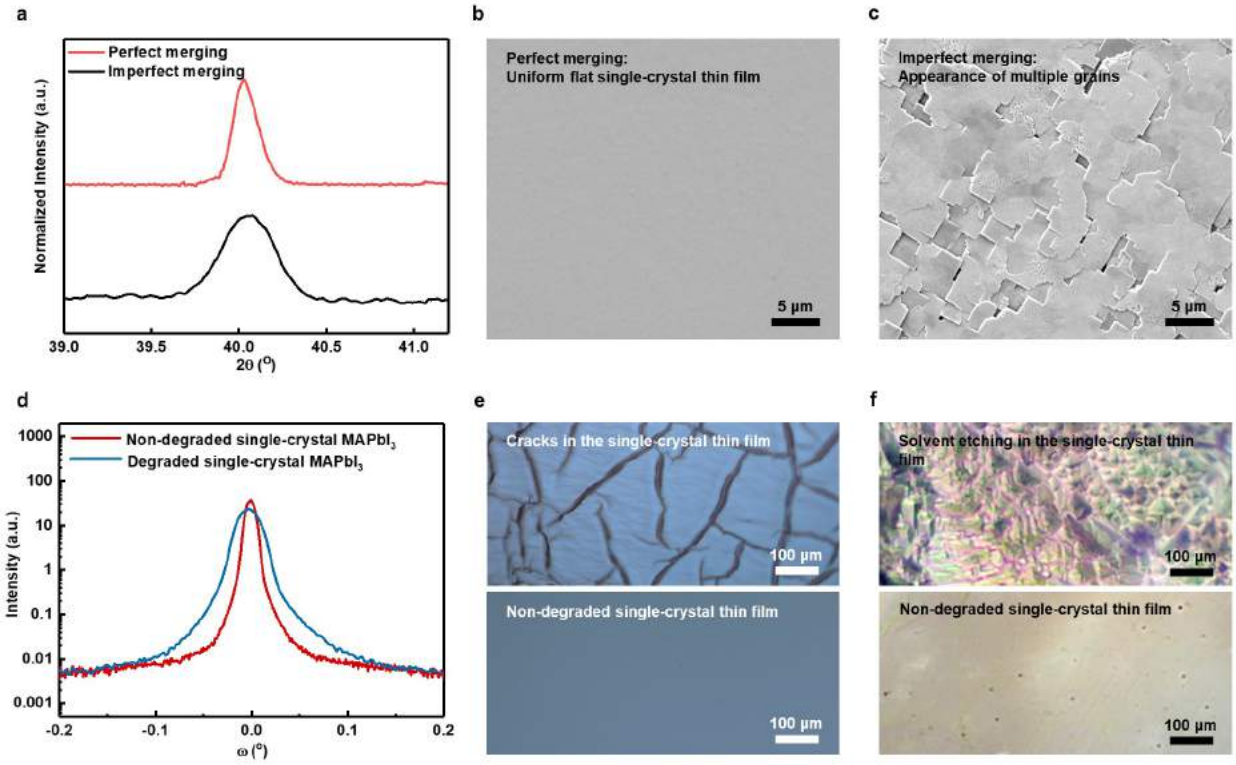

Supplementary Fig. 11 | Structural and morphological studies on the single-crystal thin film quality fabricated by the growth/transfer method. a, The (400) peaks in the XRD *θ-2θ* scan showing perfectly and imperfectly merged single-crystal thin films. The imperfect thin film shows a broad XRD peak due to the existence of small grains. SEM images show the top view of **b**, a perfect single-crystal thin film and **c**, an imperfect single-crystal thin film with multiple grains. **d**, XRD ω scans of a degraded and a non-degraded single-crystal $MAPbI_3$ thin films after the transfer and re-adhesion processes. The degraded single-crystal thin film exhibits a broad peak, which indicates a poor crystallinity. The degradations can come from either **e**, the improper lifting transfer process or **f**, improper use of the re-adhesion solvent.

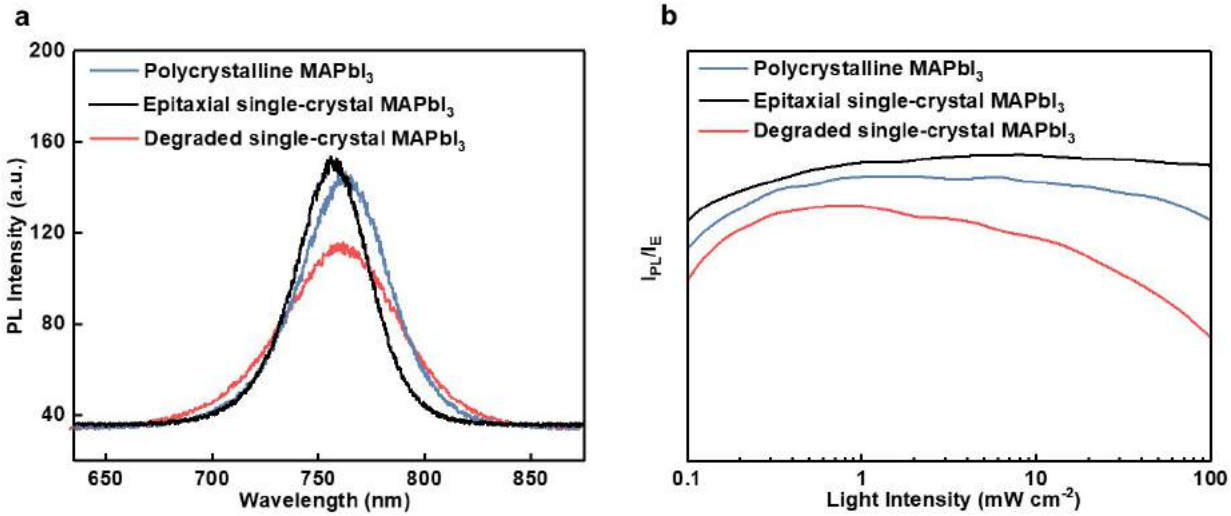

Supplementary Fig. 12 | PL studies on the quality of $MAPbI_3$ thin films. a, Three different types of $MAPbI_3$ thin films showing different PL measurement results. The polycrystalline thin film shows a little redshift compared with the single-crystal cases. The degraded single-crystal thin film shows a broad PL peak, which can be ascribed to a low crystal quality. **b**, I_{PL}/I_E comparisons showing that the polycrystalline and degraded single-crystal thin films exhibit a decreasing tendency with increasing light intensity, which provides additional evidence for their lower crystal qualities.

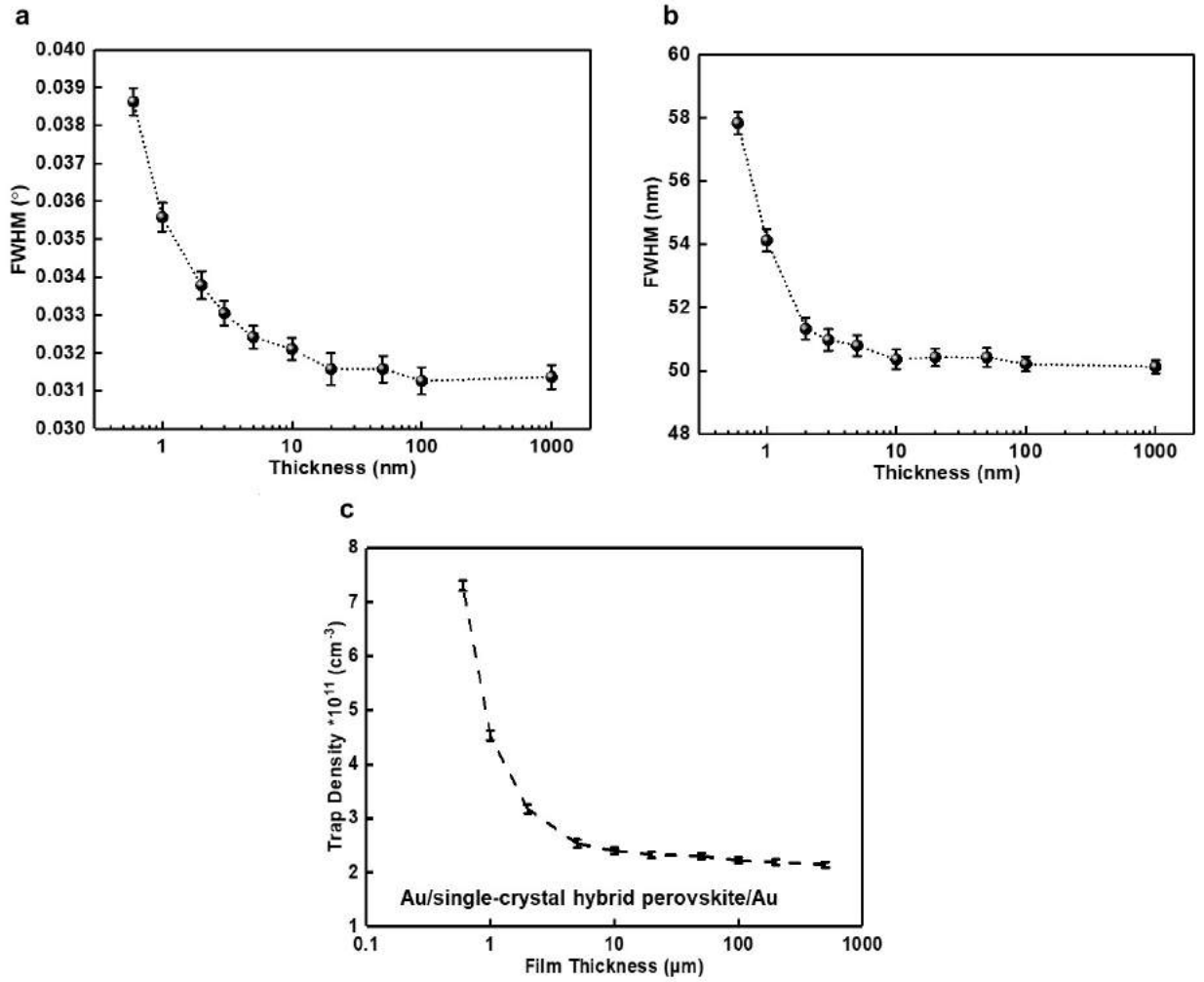

Supplementary Fig. 13 | Thickness dependent crystal qualities. a, XRD ω scan, **b**, PL measurements with different thicknesses of the crystals, and **c,** Trap density measurements. All measurements give the same trend that thicker crystals give better crystal qualities. Error bars come from three different measurements under the same scan condition.

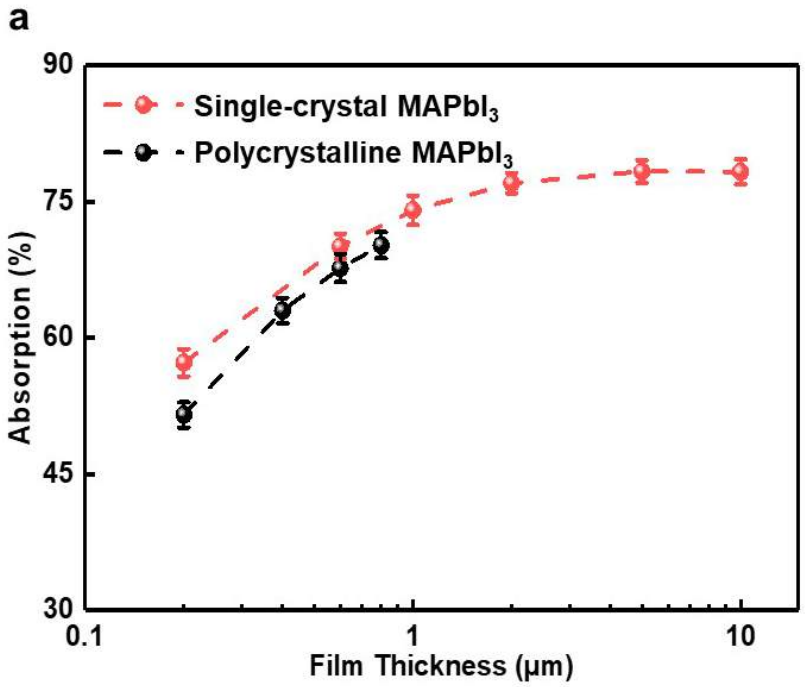

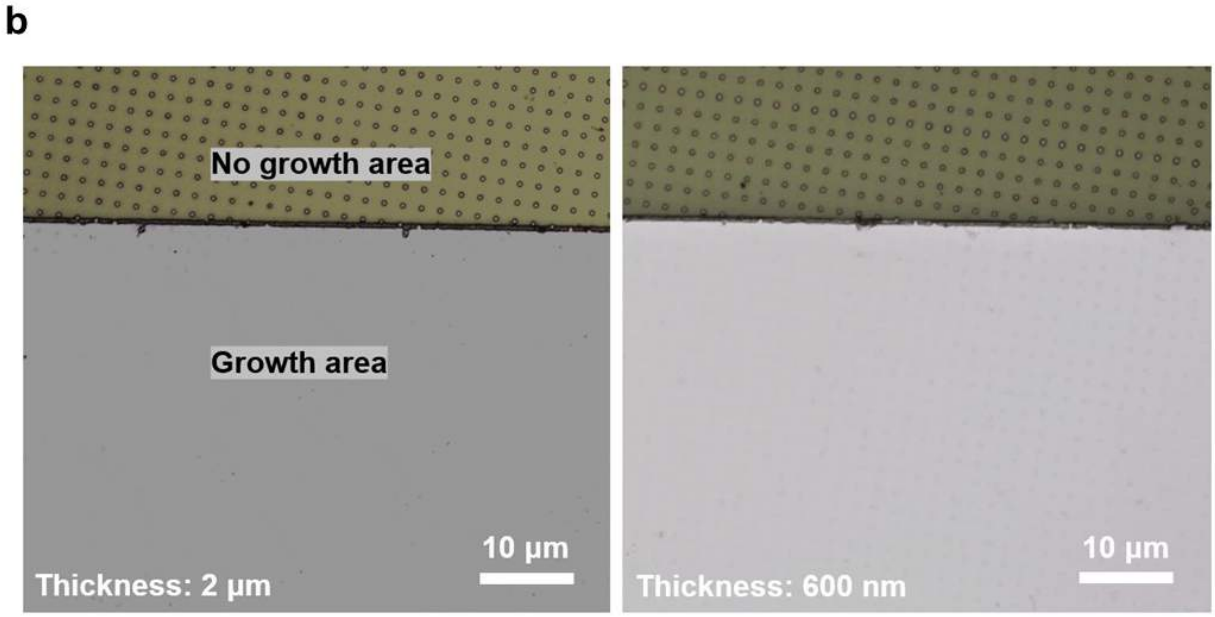

Supplementary Fig. 14 | Thickness dependent optical characterizations. a, UV-vis absorption measurements with different thicknesses for both single-crystal and polycrystalline $MAPbI_3$ thin films. **b**, Optical images showing a ~2 μm single-crystal film (left) and a ~600 nm single-crystal film (right) before transferring. The no growth area is achieved by applying a piece of tape to block growth on the patterned sites. The thickness comparison shows that a 600 nm thin film is insufficient to absorb all of the visible light.

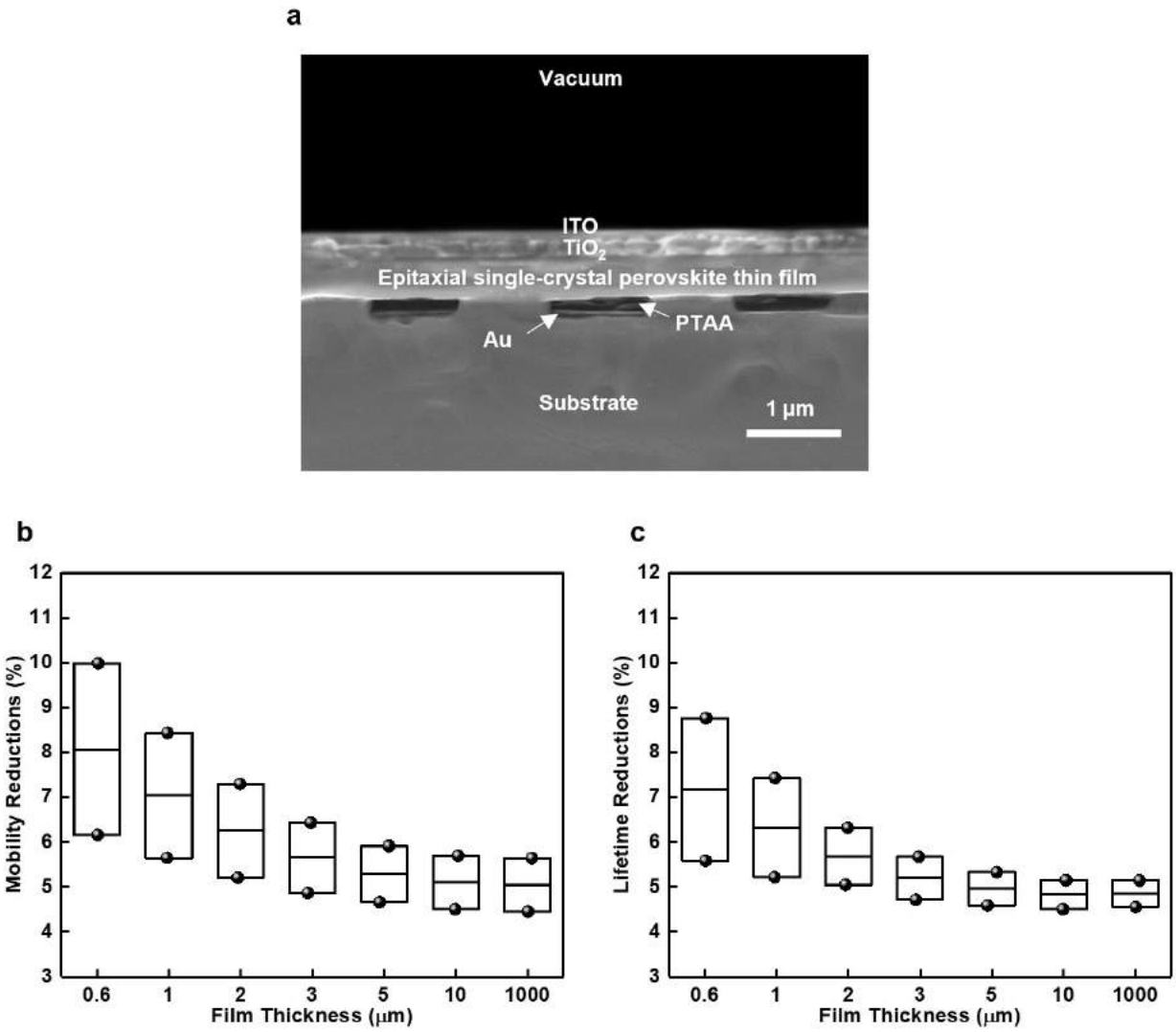

Supplementary Fig. 15 | The in situ fabricated devices and thickness-dependent carrier dynamics. a, The *in-situ* fabricated devices do not require additional peeling off the epitaxial single-crystal thin film. **b**, Mobility reductions in the $MAPbI_3$ single-crystal thin films with different thicknesses. Larger discrepancy exists in thinner films. **c**, Lifetime reductions in $MAPbI_3$ single-crystal thin films with different thicknesses. A similar tendency to the mobility reduction can be observed, indicating that the electrical measurements in thinner films are more easily to be influenced by solution treatments.

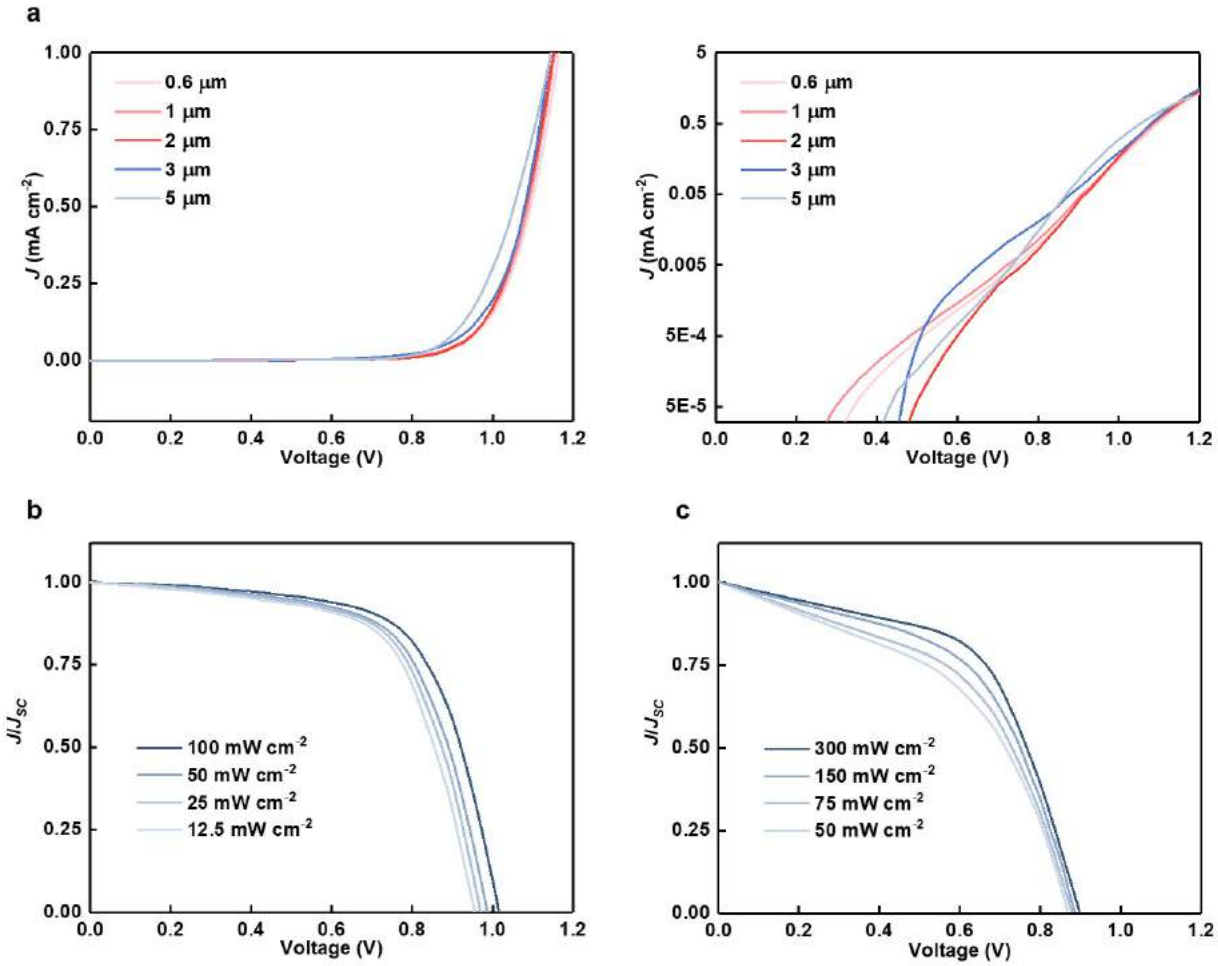

Supplementary Fig. 16 | Dark and light J-V curve measurements. a, Linear scale (left) and logarithm scale (right) dark *J-V* curves measured with different single-crystal perovskite thicknesses. The dark current is several orders of magnitude lower than the photocurrent in Figure 2b. **b**, Light *J-V* curves measured on a 600 nm thick single-crystal thin film with different light intensities. Even under the lowest 12.5 mW cm^{-2} intensity, the dark injection near the open circuit voltage condition is still insignificant, which means the shunt resistance is negligible even in the thinnest film. **c**, Light *J-V* curves measured on a 5 μm thick single-crystal thin film with different light intensities. The FF does not change significantly with an increasing light intensity, which means the series resistance does not contribute much to the *J-V* measurement results.

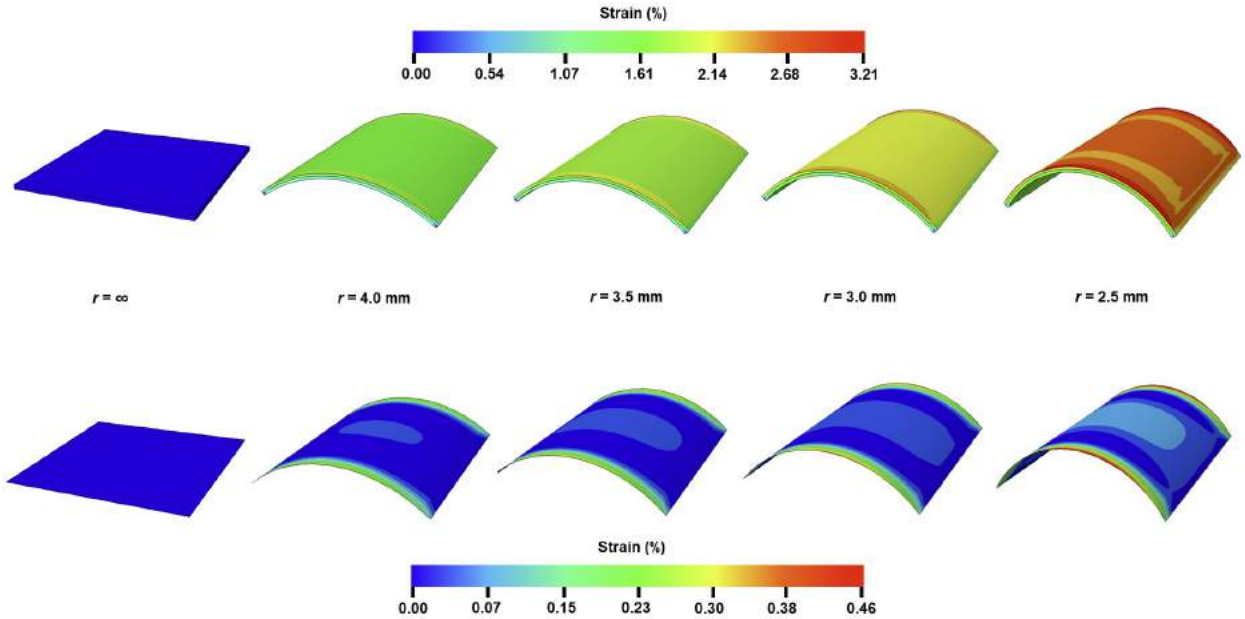

Supplementary Fig. 17 | Simulation of strain distribution in a flexible single-crystal perovskite device. Finite element analysis simulations are shown under different bending radii. The results in the top panels correspond to the entire sandwich structure, i.e., PET/single-crystal $MAPbI_3$/SU8-PDMS. The results in the bottom panels correspond to the extracted perovskite layer only (with the other layers hidden). At a bending radius of 2.5 mm, most parts of the perovskite layer have a principal strain of less than 0.25%. The edge areas show a principal strain of around 0.36%, which is close to the failure strain of this material.

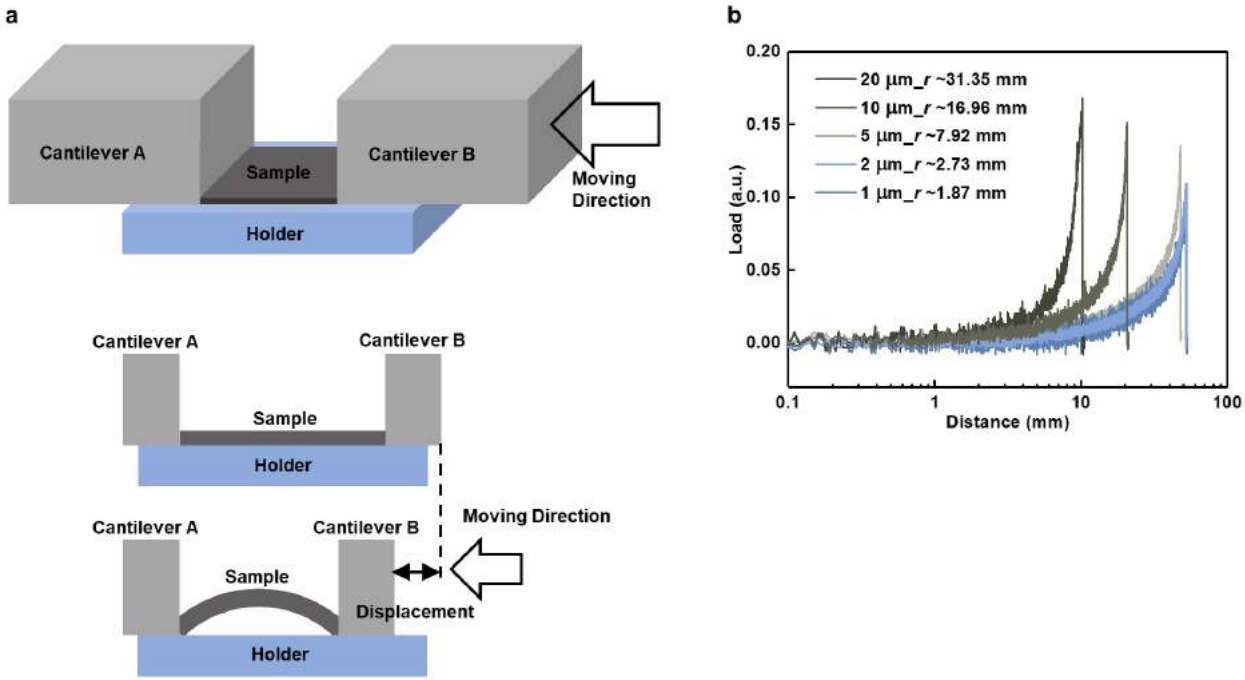

Supplementary Fig. 18 | Flexibility tests of the NMP design. a, Schematics of the measurement setup. A 5 cm by 5 cm sample is used to do the test, where the single-crystal perovskite crystal is at the NMP of the sample. The displacement is used to calculate the bending radius. **b**, Testing results showing remarkable flexibility of such brittle single-crystal perovskites. The thinner the perovskite crystal is, the smaller it can be bent.

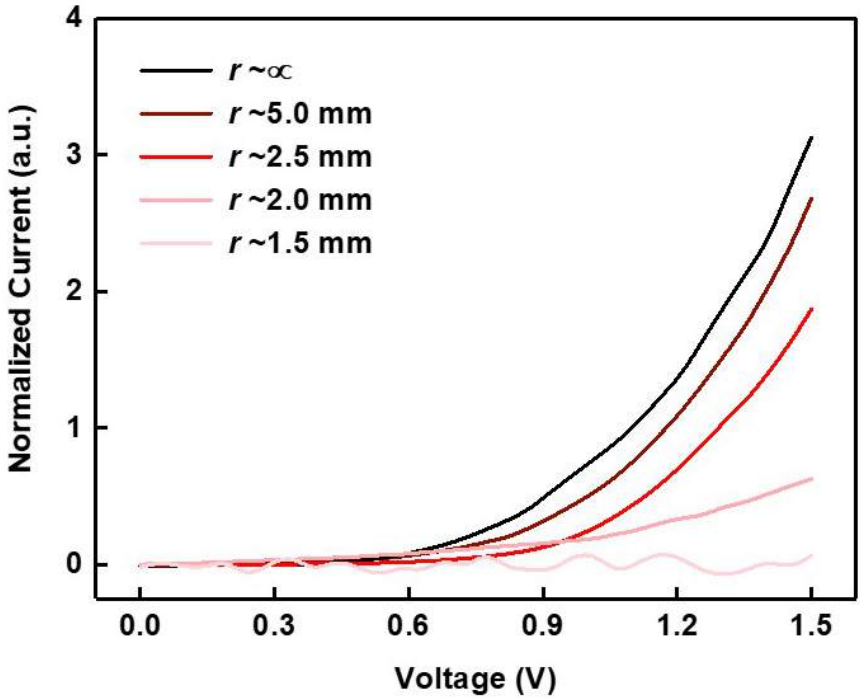

Supplementary Fig. 19 | IV measurements of the flexible single-crystal $MAPbI_3$ under different bending radii. The results show a significant reduction in the current when the device is bent at $r \sim 2$ mm.

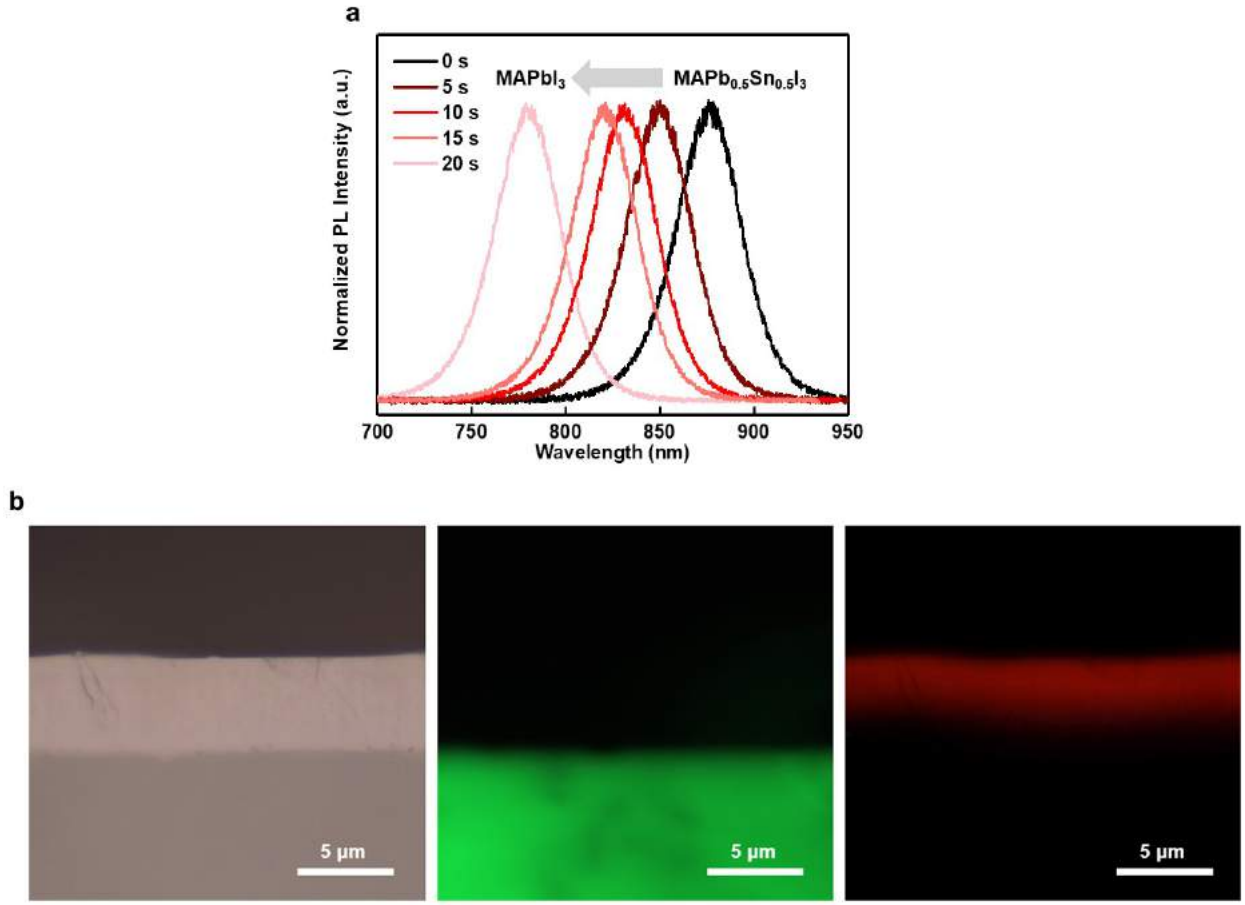

Supplementary Fig. 20 | PL measurements of graded single-crystal $MAPb_{0.5+x}Sn_{0.5-x}I_3$. a, PL measurements of graded single-crystal $MAPb_{0.5+x}Sn_{0.5-x}I_3$ at different growth time-stages. All samples are measured only at the top surface. A blue shift of the PL as time increases corresponds to an increased bandgap from the $MAPb_{0.5}Sn_{0.5}I_3$ side to the $MAPbI_3$ side. **b**, An optical image (left) shows the epitaxially grown graded single-crystal $MAPb_{0.5+x}Sn_{0.5-x}I_3$ on top of the single-crystal $MAPbBr_3$ substrate. The middle fluorescent image is from $MAPbBr_3$ while the right fluorescent image is from Pb rich part in the graded single-crystal $MAPb_{0.5+x}Sn_{0.5-x}I_3$.

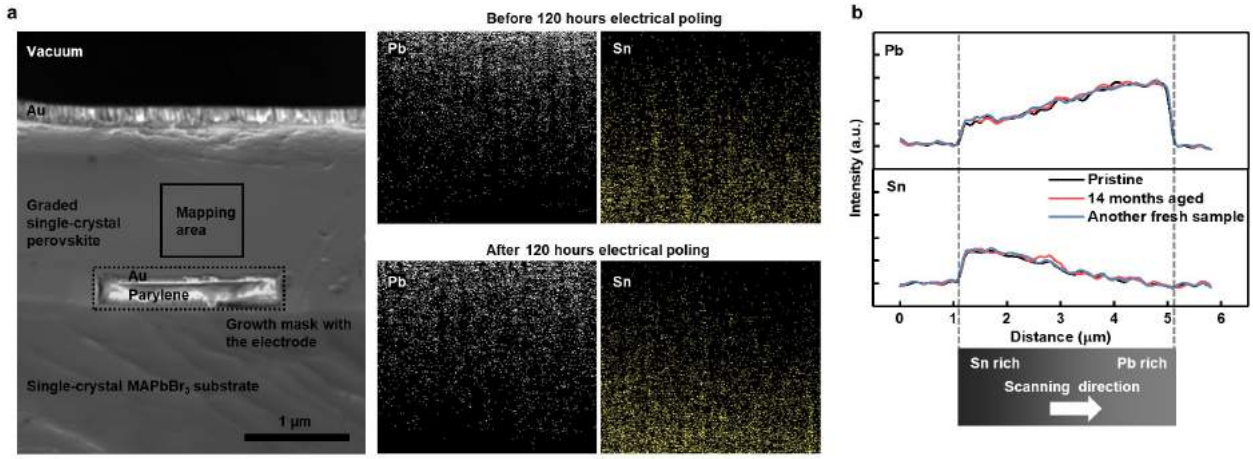

Supplementary Fig. 21 | Cross-sectional linear energy-dispersive x-ray spectroscopy (EDX) measurements. a, EDX mapping of the graded single-crystal $MAPb_{x+0.5}Sn_{x-0.5}I_3$. The patterned parylene/Au serves as the bottom electrode while the top Au electrode is evaporated by e-beam evaporation. The sample is kept in a dark dry box while a 1.2 V DC bias is applied. No noticeable Sn/Pb ion migration happens after 120 hours of electrical poling. **b,** EDX linear scans with gradient intensities of Sn and Pb along the scan direction, which confirms the gradually alloyed structure. A repeated measurement, after 14 months storage in the vacuum box, reveals the stability of the single-crystal $MAPb_{x+0.5}Sn_{x-0.5}I_3$.

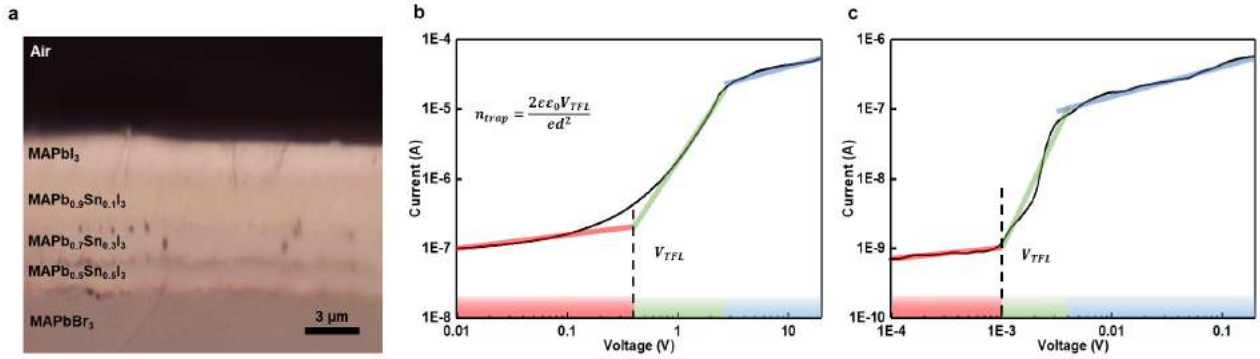

Supplementary Fig. 22 | A single-crystal perovskite structure with distinct heterojunctions. a, An optical image showing the multilayered single-crystal perovskite with clear heterojunction interfaces between adjacent layers. *I-V* measurements of the trap densities in **b**, a double-layered single-crystal $MAPbI_3$-$MAPb_{0.5}Sn_{0.5}I_3$ and **c**, a graded $MAPb_{0.5+x}Sn_{0.5-x}I_3$ structure. The heterojunction double-layer shows a higher trap density $n_{trap} = 1.77\times10^{14}\ cm^{-3}$ than $n_{trap} = 3.34\times10^{12}\ cm^{-3}$ of the graded structure. The single-crystal perovskite thickness is ~10 μm for both cases.

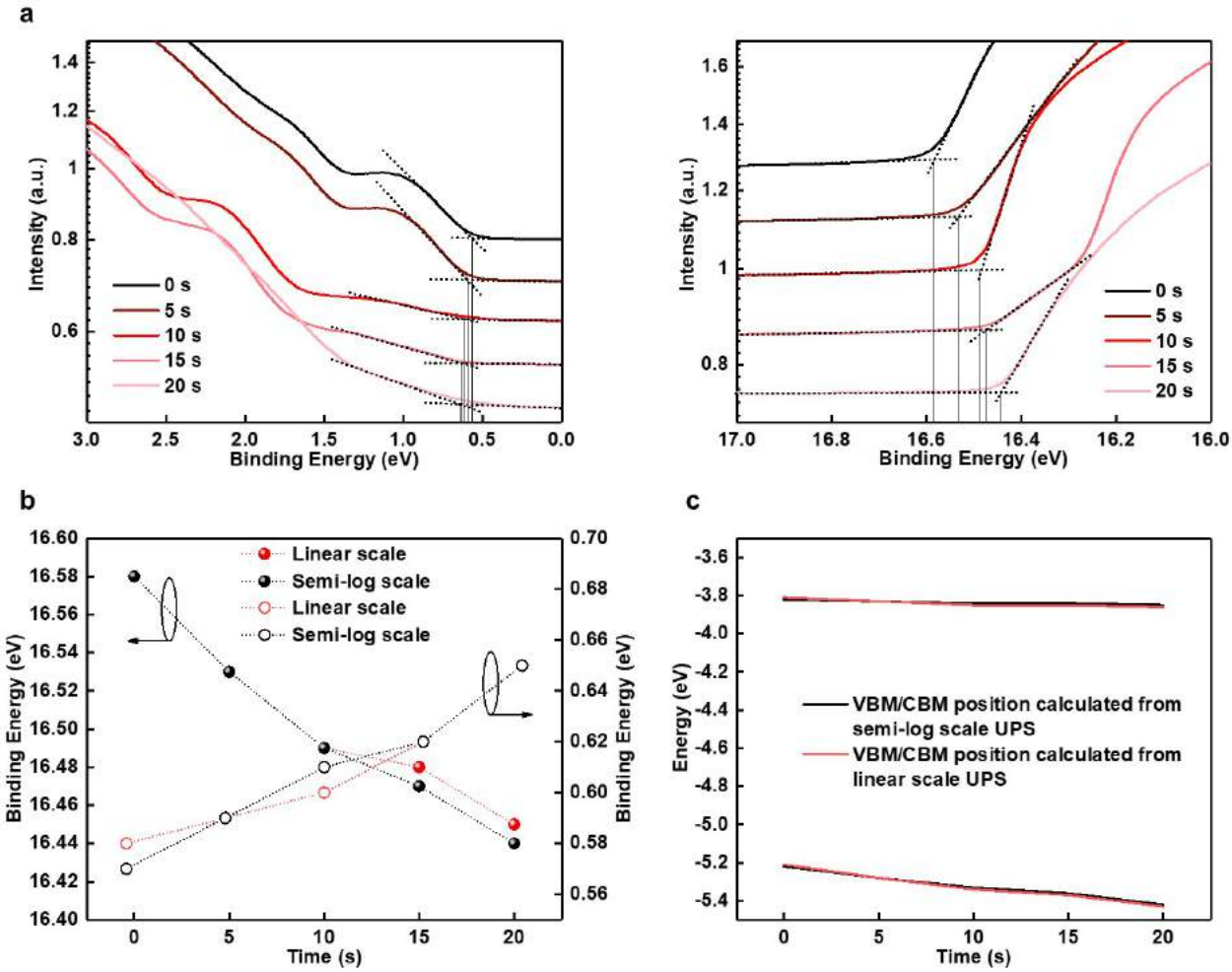

Supplementary Fig. 23 | UPS measurements of the graded epitaxial single-crystal $MAPb_{0.5+x}Sn_{0.5-x}I_3$. **a**, Semi-log plots are used to identify the VBM position from the low binding energy cutoff (left) and the high binding energy cutoff (right). **b**, Comparing binding energies from the linear scale plots and the semi-log scale plots, the difference is considered to be negligible in this case. **c**, Summarized band diagrams calculated from the UPS data in both linear scale and semi-log scale. No obvious difference can be found.

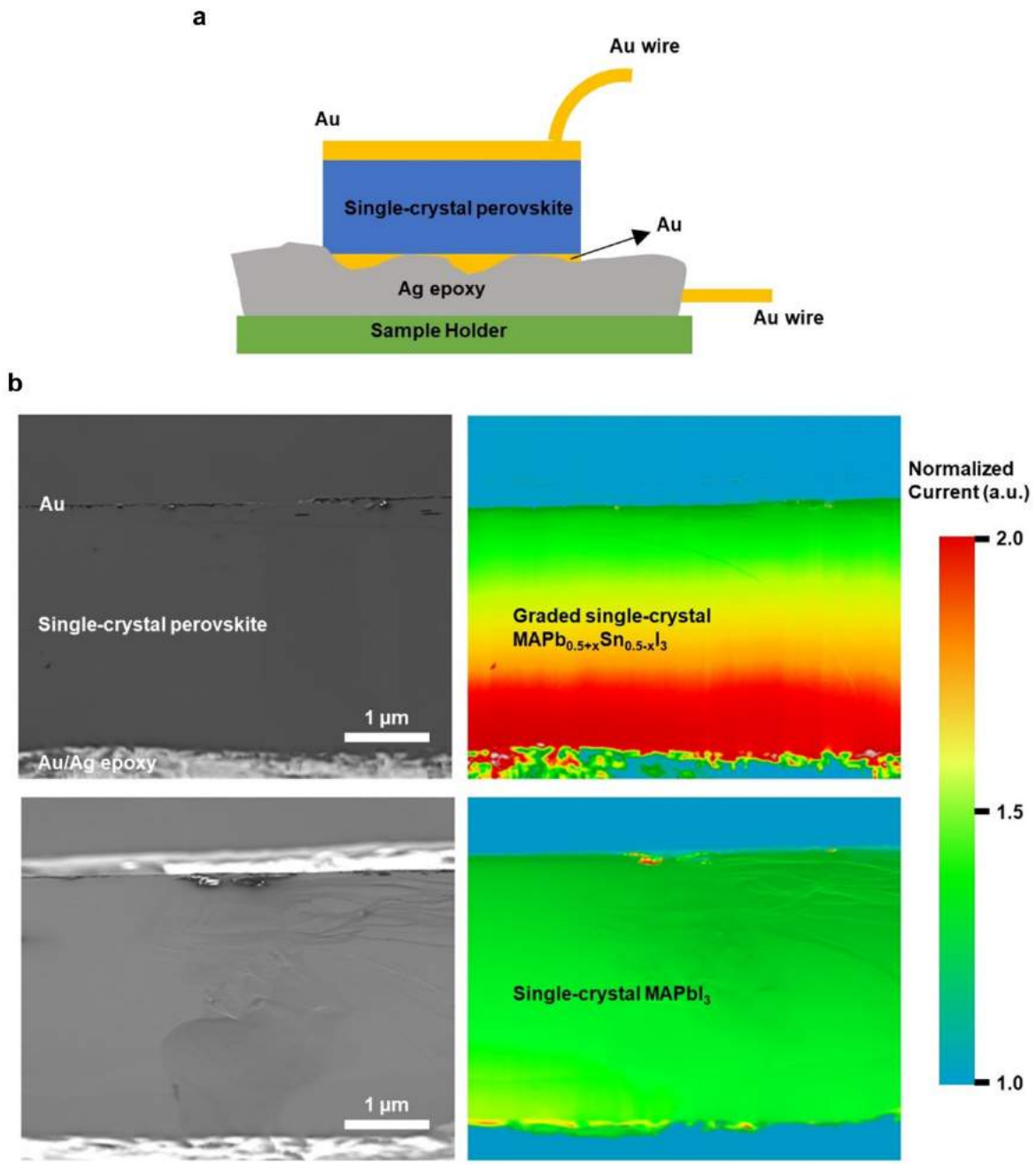

Supplementary Fig. 24 | EBIC mapping with symmetric electrodes. a, The schematic measurement setup. Same Au electrodes are used on both sides. **b**, The graded current output can only be observed in the graded single-crystal perovskite, which excludes the possible influence from the electrodes to the EBIC measurements.

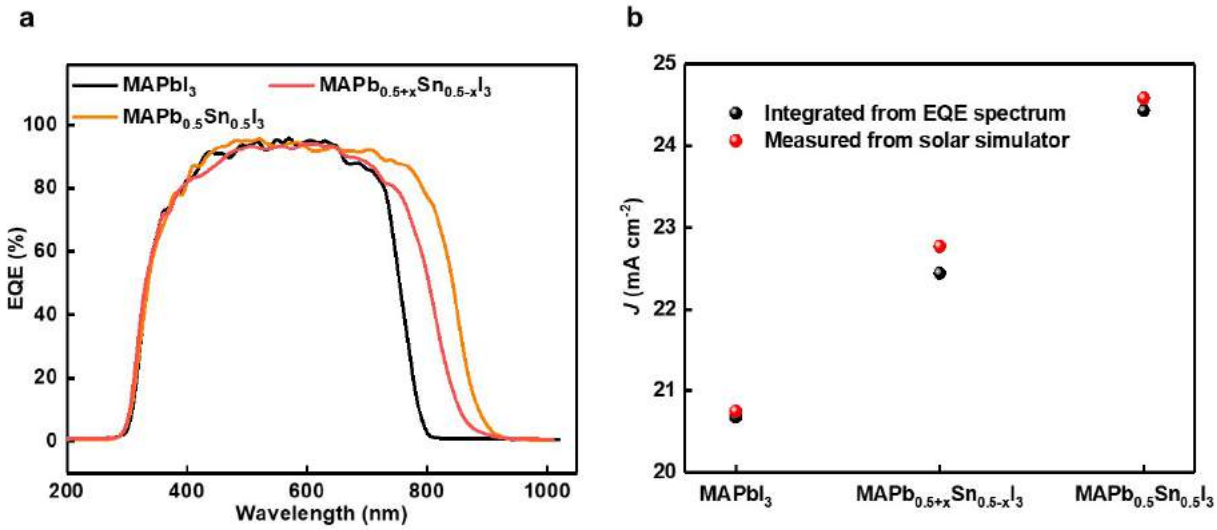

Supplementary Fig. 25 | EQE measurements with different absorbers. a, Bandgap-graded single-crystal $MAPb_{0.5+x}Sn_{0.5-x}I_3$ photovoltaic devices show a median averaged current density (integrated EQE) compared with single-crystal $MAPbI_3$ and compositionally uniform single-crystal $MAPb_{0.5}Sn_{0.5}I_3$. More Sn content leads to a lower bandgap and exciton dissociation energy, and thus a higher EQE. **b**, Current density from integrated EQE measurements, which matches the *J-V* results and confirms the higher current density is due to the Sn doping.

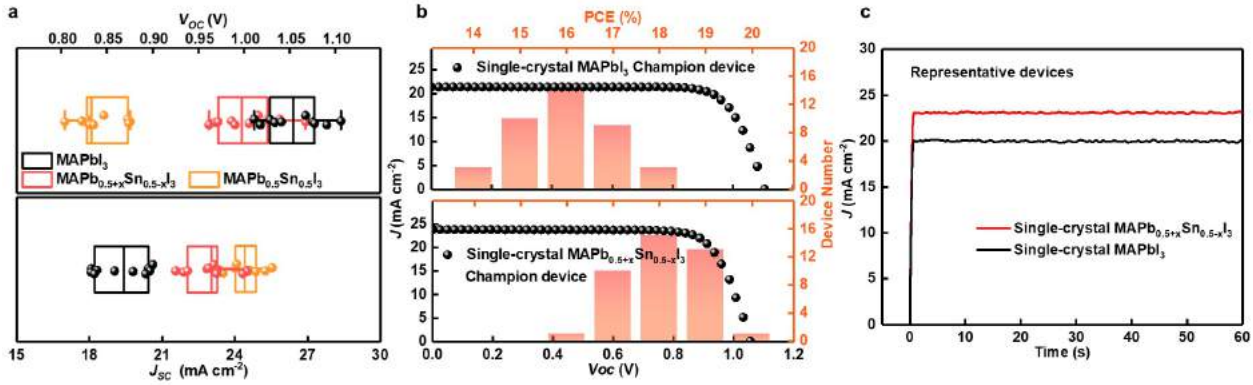

Supplementary Fig. 26 | The statistical device performance distributions. a, Bandgap-graded $MAPb_{0.5+x}Sn_{0.5-x}I_3$ showing a higher J_{SC} than $MAPbI_3$ and relatively maintained V_{OC}. **b**, PCE distributions for single-crystal $MAPbI_3$ (top) and graded single-crystal $MAPb_{0.5+x}Sn_{0.5-x}I_3$ (bottom) photovoltaic devices. The graded single-crystal photovoltaics show overall better performance (with the highest PCE ~ 20.04%) than the compositionally uniform single-crystal photovoltaics. **c**, Measured photocurrent at maximum power points for representative devices as a function of time.

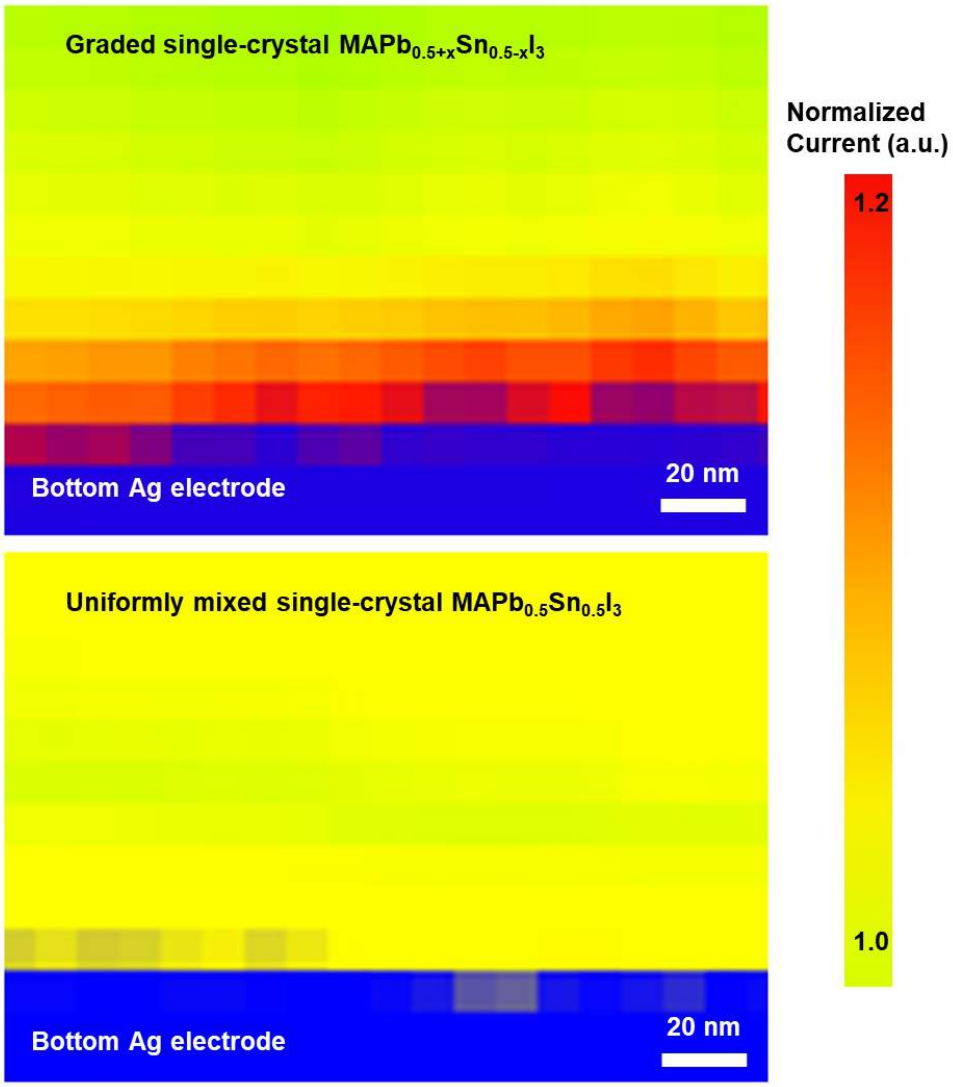

Supplementary Fig. 27 | Close-up EBIC mapping results at the interface. In the graded single-crystal $MAPb_{0.5+x}Sn_{0.5-x}I_3$, the interfacial region with the bottom electrode shows stronger current signals than regions away from the interface, which is because of the gradually mixed Pb and increased bandgap. The compositionally uniform single-crystal $MAPb_{0.5}Sn_{0.5}I_3$ shows uniform current signals. However, the interfacial region in the graded single-crystal $MAPb_{0.5+x}Sn_{0.5-x}I_3$ (where the composition is $MAPb_{0.5}Sn_{0.5}I_3$ at the interfacial region) always gives even stronger signals than the compositionally uniform single-crystal $MAPb_{0.5}Sn_{0.5}I_3$. The stronger signals are likely due to the easier exciton separation and carrier collection facilitated by the graded bandgap in the $MAPb_{0.5}Sn_{0.5}I_3$.

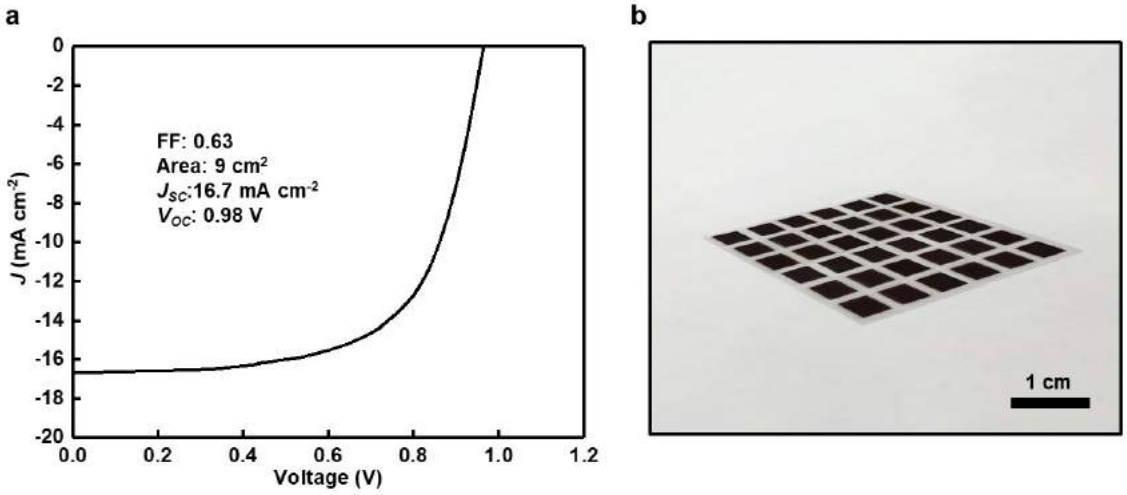

Supplementary Fig. 28 | Large-scale flexible single-crystal perovskite photovoltaics. a, The *J-V* measurement of the best large-scale flexible single-crystal perovskite photovoltaic device, which results in a PCE ~10.3% with a working area of around 9 cm^2. **b**, An optical image showing the island-bridge structure before depositing Spiro-MeOTAD and Au. Each black single-crystal perovskite is around 5 mm by 5 mm.

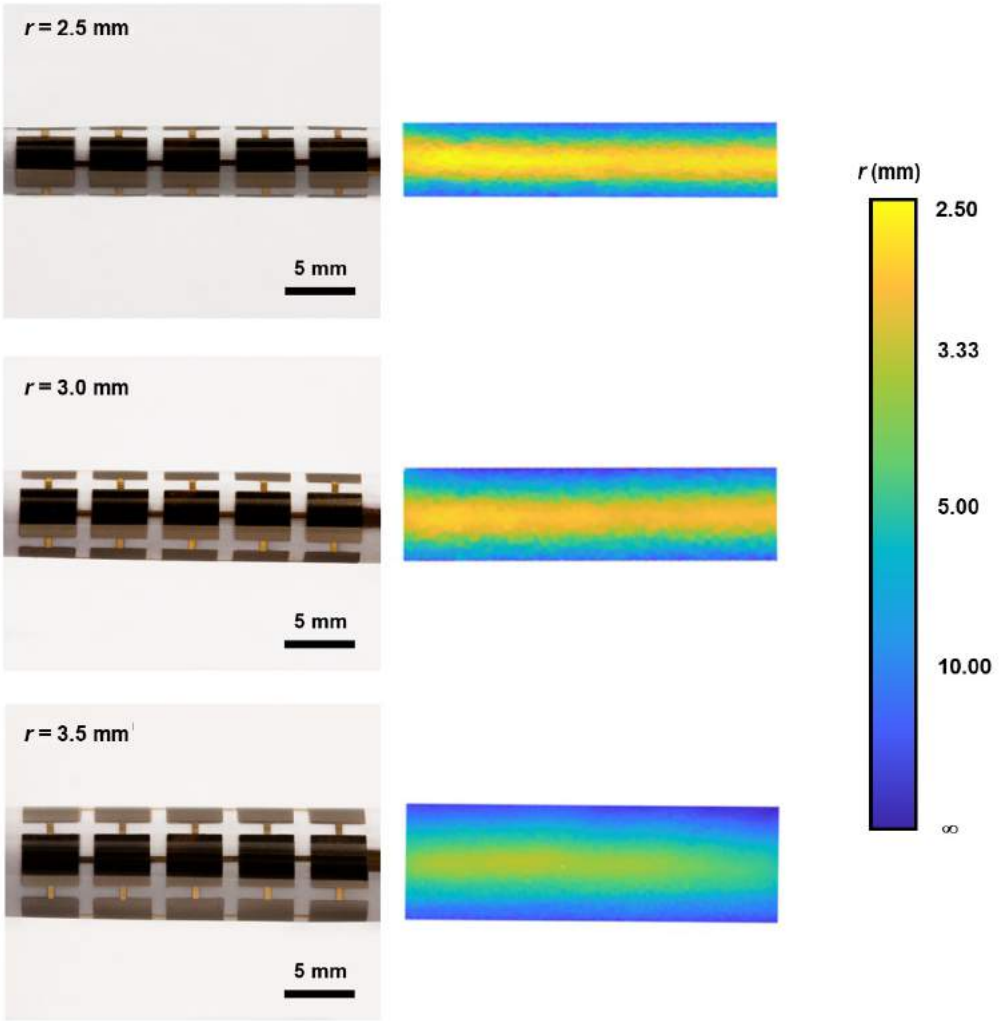

Supplementary Fig. 29 | Bending radius distribution mapping. The results show that the minimum bending radius occurs at the middle line of the device. Most parts of the device will not experience such extreme bending conditions.

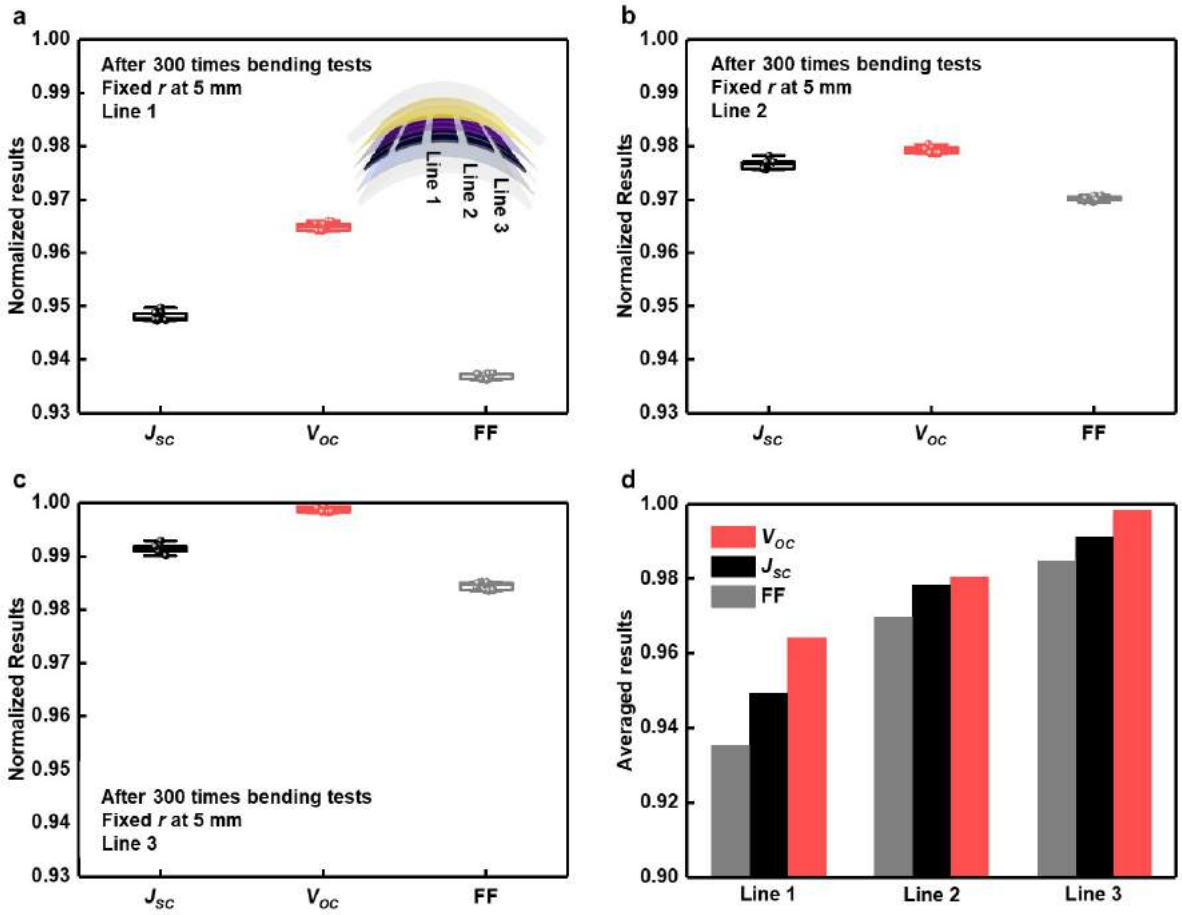

Supplementary Fig. 30 | Cyclic bending tests. The results for different pixels in line 1, line 2, and line 3 after cycling for 300 times are shown in **a**, **b**, and **c**, respectively. The inset schematics in **a** show the non-uniform bending conditions for different pixels. Line 1, line 2, and line 3 undergo different bending radii during the cycling. **d**, The comparison of V_{OC}, J_{SC}, and FF among different lines showing the impact of different bending curvatures on the device performance.

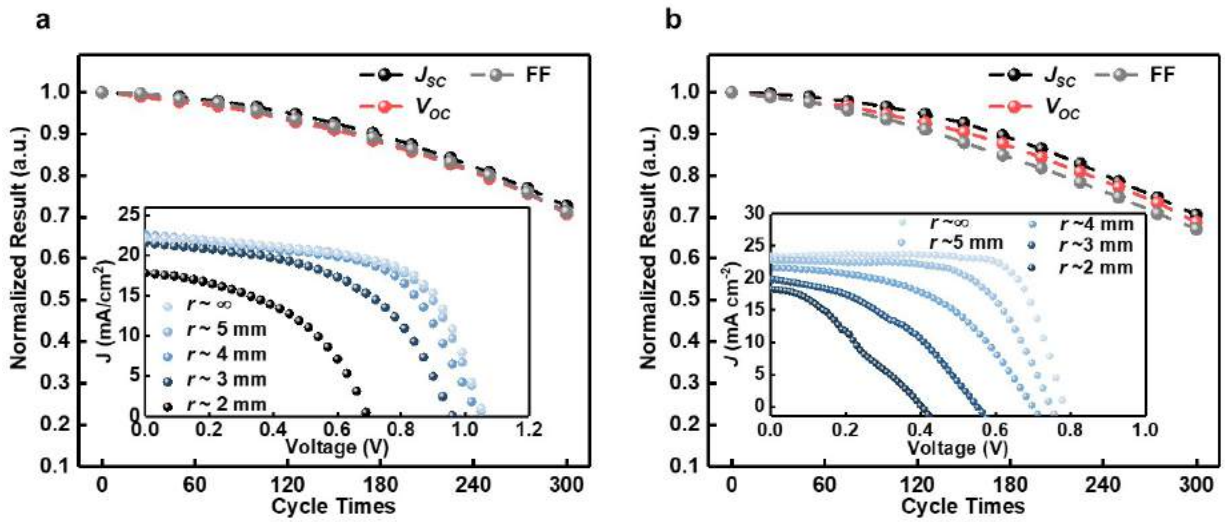

Supplementary Fig. 31 | Cyclic flexibility tests of polycrystalline structures. The test results are for **a**, polycrystalline $MAPbI_3$ and **b**, polycrystalline $MAPb_{0.5}Sn_{0.5}I_3$. The insets show *J-V* curves with different bending radii. All of these results demonstrate obvious degradation of the device performance, likely due to the grain boundary facilitated ion/molecule migration.

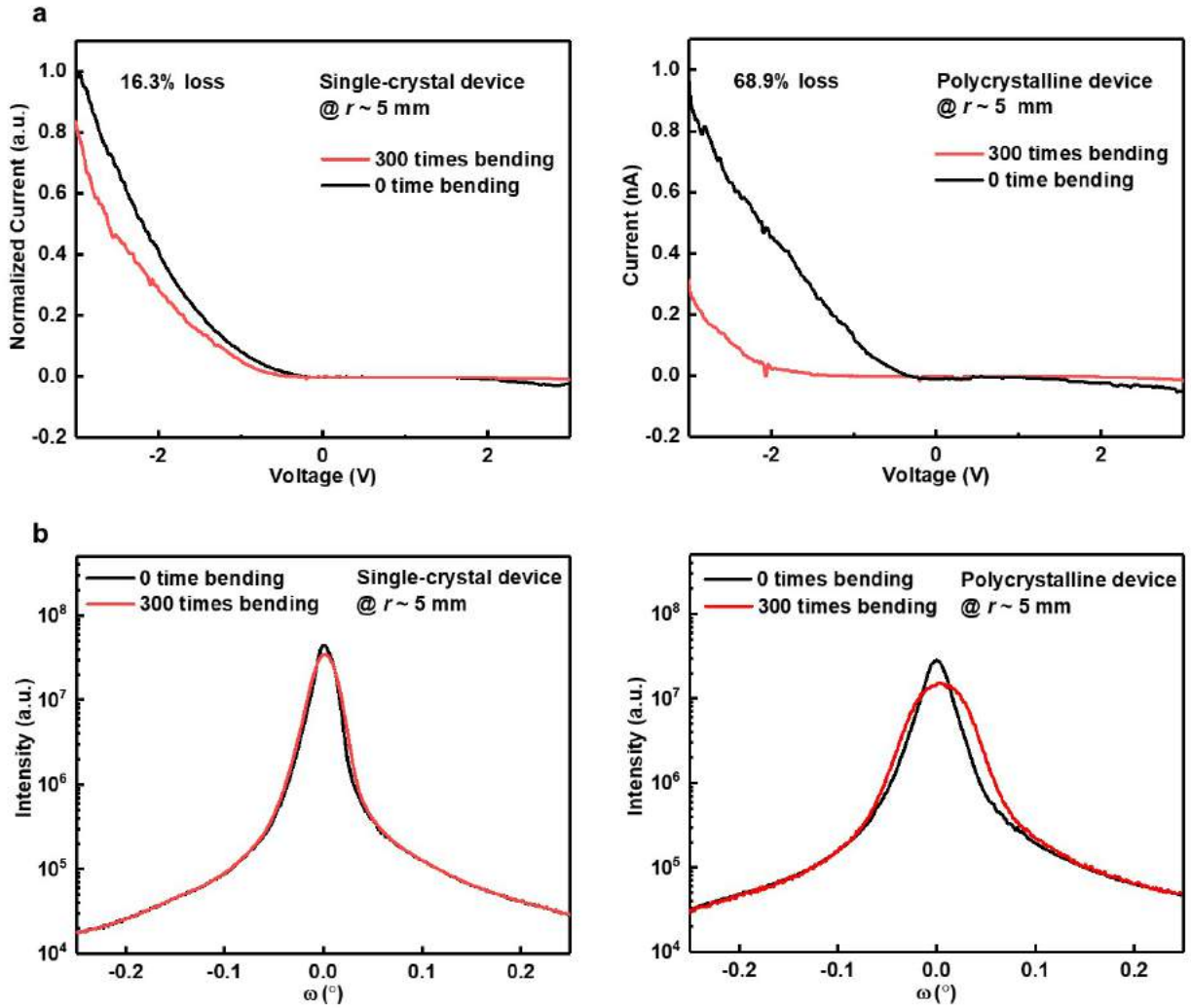

Supplementary Fig. 32 | Bending stability characterizations between single-crystal and polycrystalline structures. a, *I-V* measurement results of the single-crystal device (left) and the polycrystalline device (right). **b**, XRD ω scan measurement results of the single-crystal (left) and the polycrystalline (right). The single-crystal is more resistant to fatigue than the polycrystalline.

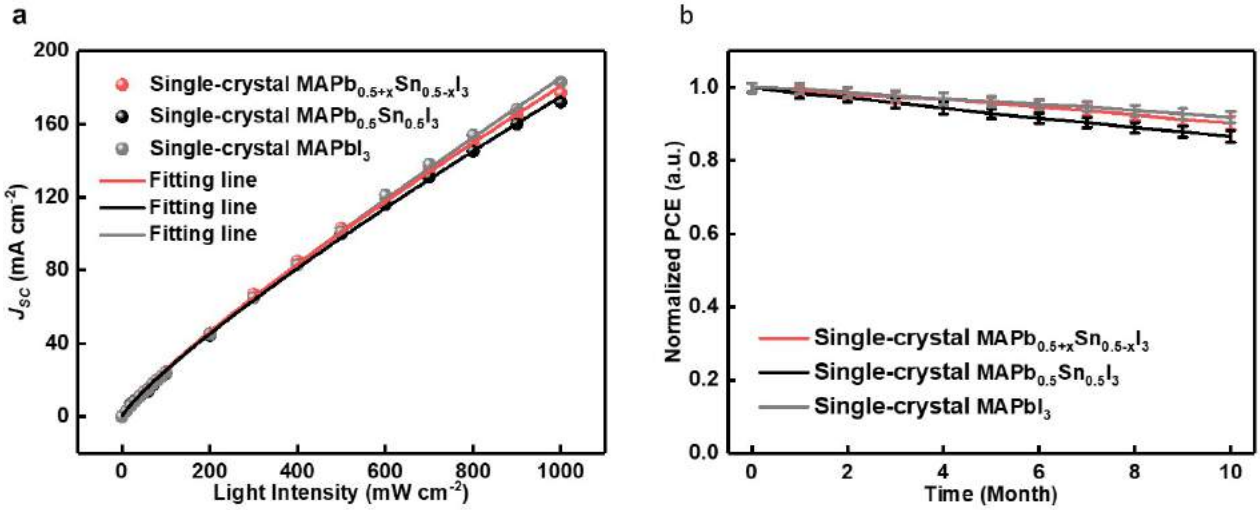

Supplementary Fig. 33 | Single-crystal photovoltaics stability measurements. a, Stress stability and **b**, long-term stability tests of three single-crystal photovoltaics with different compositions. The single-crystal devices show no obvious difference in stabilities. Error bars come from three different measurements with different aperture positions.

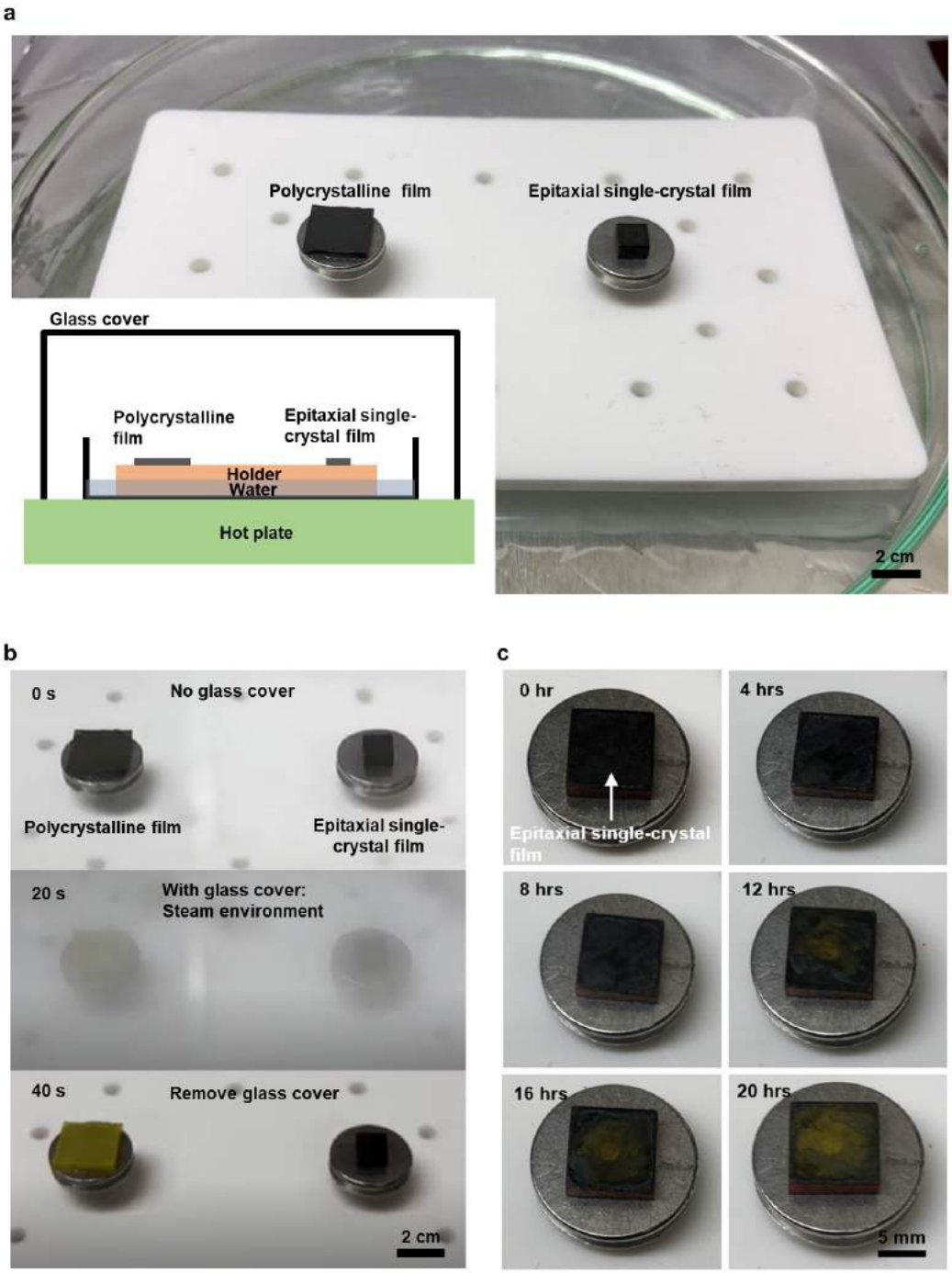

Supplementary Fig. 34 | Accelerated thermal and humidity tests. a, Experimental setups for thermal and humidity tests. The hot plate temperature is set to be 100 °C. Inset schematics show the entire setup, which gives a qualitative comparison between the polycrystalline $MAPb_{0.5}Sn_{0.5}I_3$ film and the single-crystal $MAPb_{0.5}Sn_{0.5}I_3$ film under hot and humid conditions. **b**, Polycrystalline $MAPb_{0.5}Sn_{0.5}I_3$ film exhibits rapid color change and phase transition while the single-crystal $MAPb_{0.5}Sn_{0.5}I_3$ film remains intact. **c**, Extended monitoring of the single-crystal $MAPb_{0.5}Sn_{0.5}I_3$ film under the same condition. The degradation rate of the single crystal is much slower than that of the procrystalline.

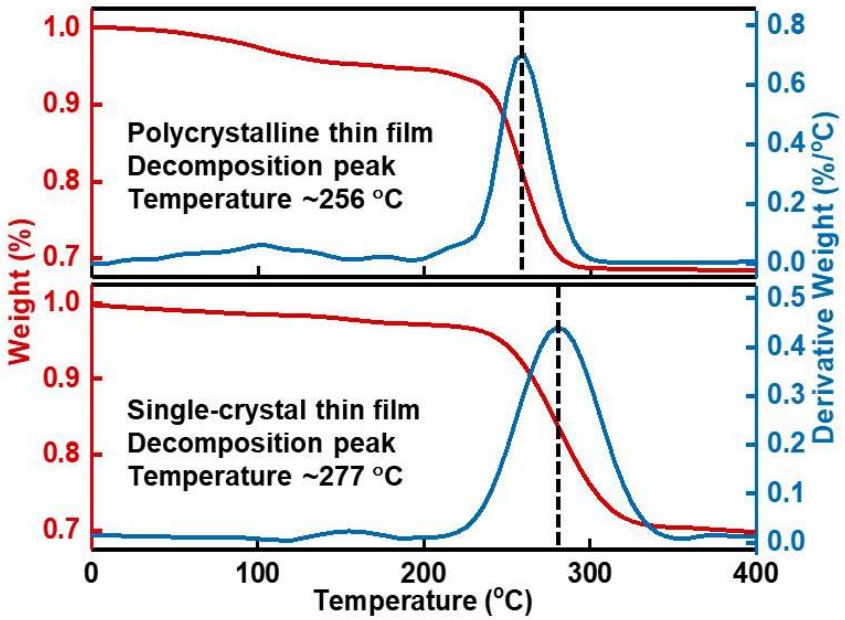

Supplementary Fig. 35 | Thermogravimetric analysis characterizations for the polycrystalline $MAPb_{0.5}Sn_{0.5}I_3$ and the graded single-crystal $MAPb_{0.5+x}Sn_{0.5-x}I_3$ films. The results show a faster degradation of the polycrystalline film at a lower decomposition temperature than the single-crystal film.

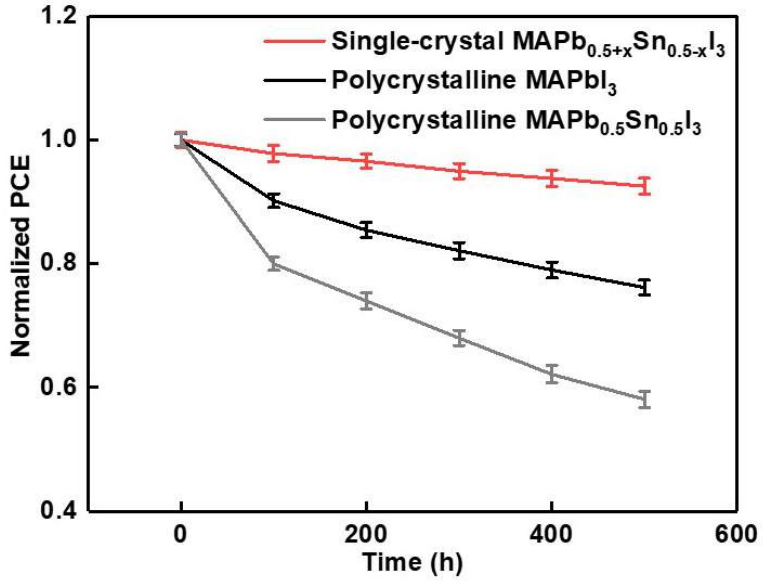

Supplementary Fig. 36 | Long-time continuous illumination stability tests with the PTAA as the HTL layer. The PTAA-based devices exhibit better thermal and light stability under the continuous illumination condition than the Spiro-based devices. Therefore, the difference between the perovskite structures can be more easily revealed. The single-crystal devices exhibit better device stability than the polycrystalline counterparts.

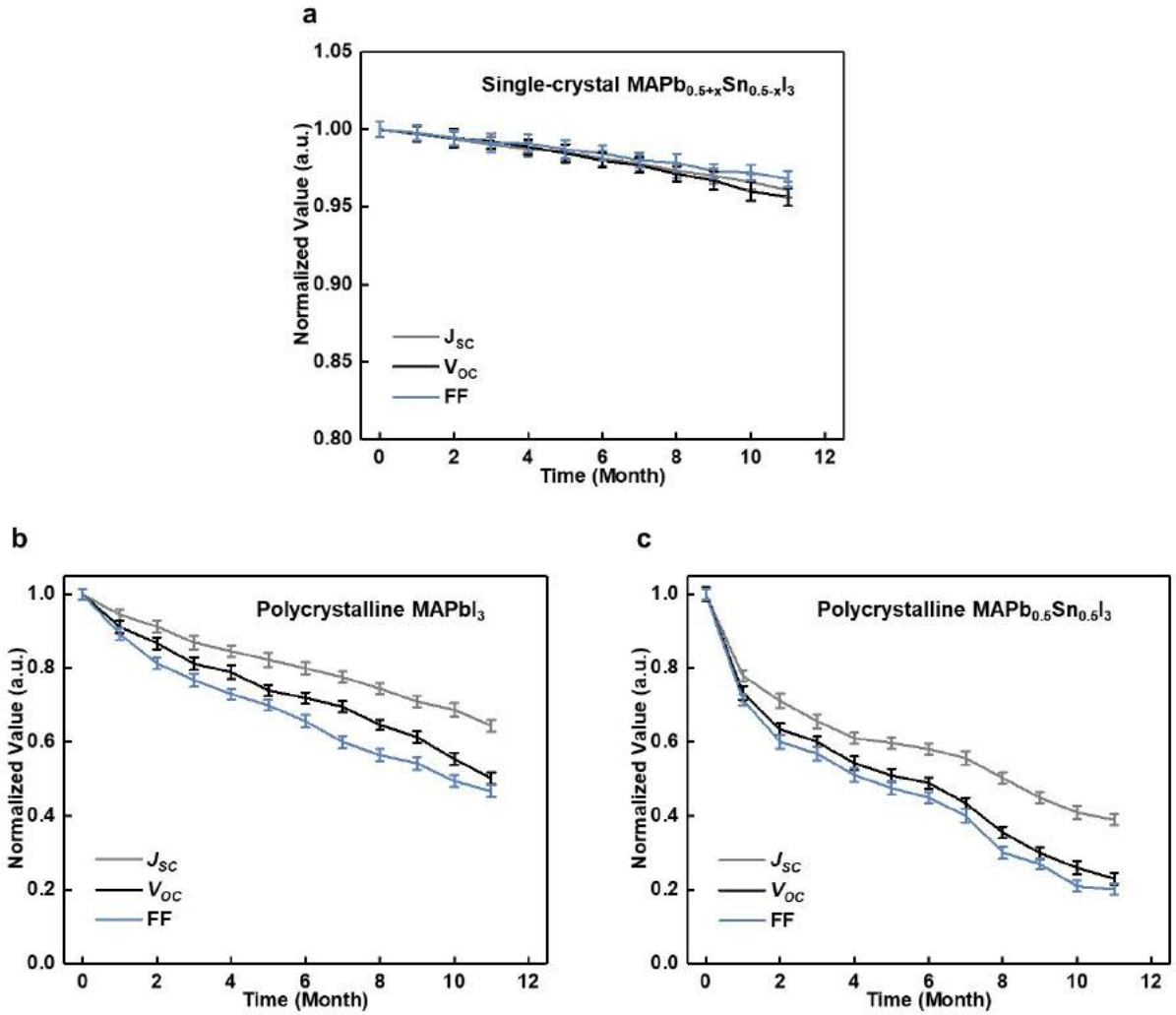

Supplementary Fig. 37 | Long-time stability measurements of photovoltaic devices. V_{OC}, J_{SC}, and FF data for PCE measurements in **a**, single-crystal $MAPb_{0.5+x}Sn_{0.5-x}I_3$, **b**, polycrystalline $MAPbI_3$, and c, polycrystalline $MAPb_{0.5}Sn_{0.5}I_3$ photovoltaic devices. Error bars come from three different measurements with different aperture positions.

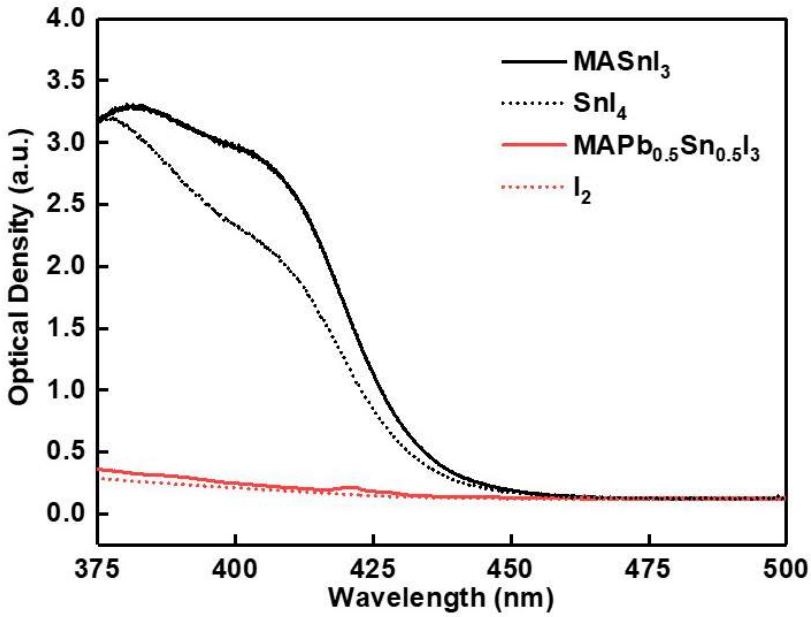

Supplementary Fig. 38 | Absorption measurements on single-crystal perovskite solutions. Purely Sn-based single-crystal perovskite and Pb-Sn mixed single-crystal perovskite exhibit different absorption peaks, indicating that the major by-products resulted from oxidations are different.

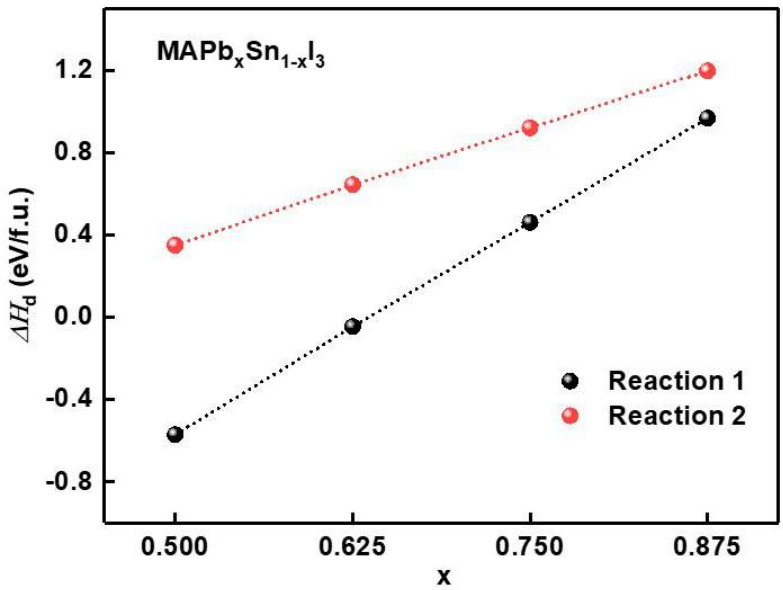

Supplementary Fig. 39 | Simulation results on decomposition enthalpies of different Pb-Sn ratios. In the Pb-Sn mixed system, reaction (1) is more favorable at any Pb-Sn ratios than reaction (2), which is consistent with the optical absorption results that the major by-products after oxidation are different from the purely Sn based system. Additionally, increasing the Pb ratio can further slow down the oxidation rate.

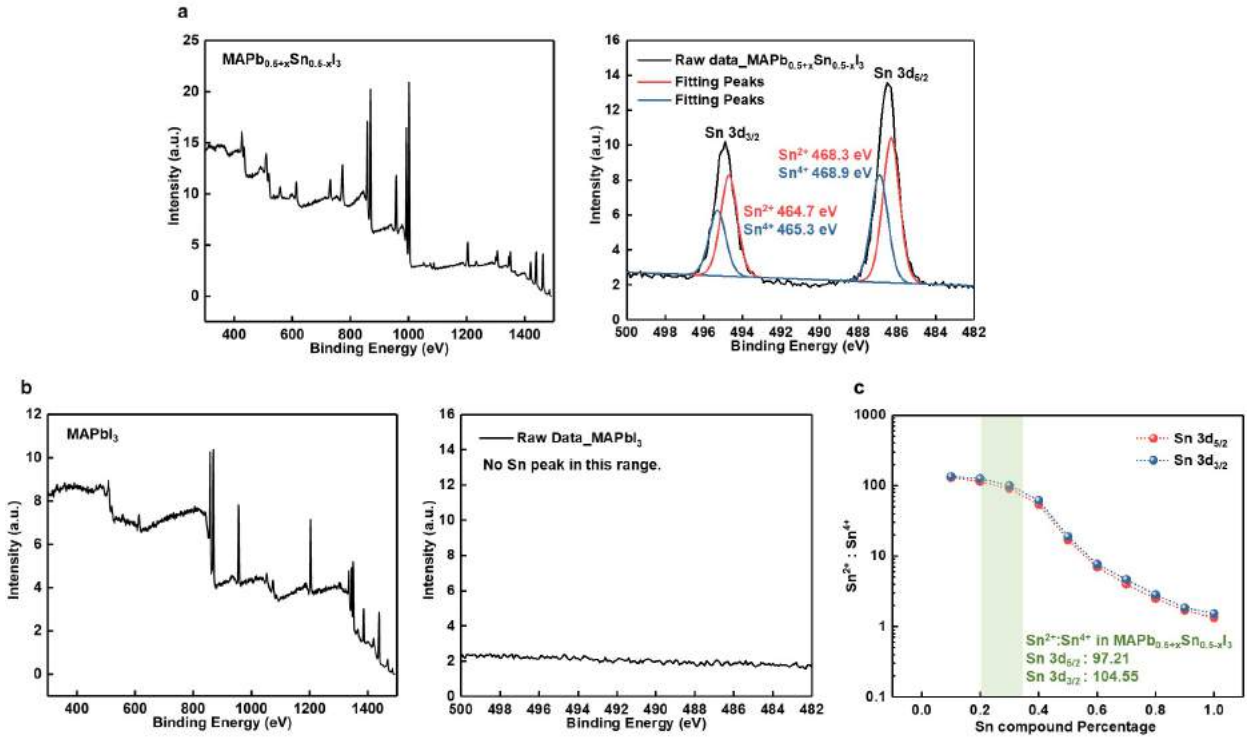

Supplementary Fig. 40 | XPS measurements with different Pb-Sn single-crystal compositions. a, XPS spectrum measured for single-crystal $MAPb_{0.5+x}Sn_{0.5-x}I_3$ (left) and zoom-in spectrum for typical Sn peaks in single-crystal $MASnI_3$ (right). Strong Sn^{2+} and Sn^{4+} peaks can be fitted. **b**, XPS spectrum measured for a control sample of single-crystal $MAPbI_3$ (left) and zoom-in spectrum for typical Sn peaks in single-crystal $MAPbI_3$ (right). No Sn peak can be found. **c**, Estimated Sn ratios in the single-crystal $MAPb_{0.5+x}Sn_{0.5-x}I_3$. The y-axis is the XPS peak ratio of Sn^{2+} to Sn^{4+}. We prepared and characterized samples with different Pb-Sn ratios using XPS. Under the same condition (preparation environment, transfer loading time, etc), increasing the Pb ratio can slow down the oxidation rate of Sn^{2+}. The shaded region is the estimated real Sn ratio in the graded single-crystal $MAPb_{0.5+x}Sn_{0.5-x}I_3$.

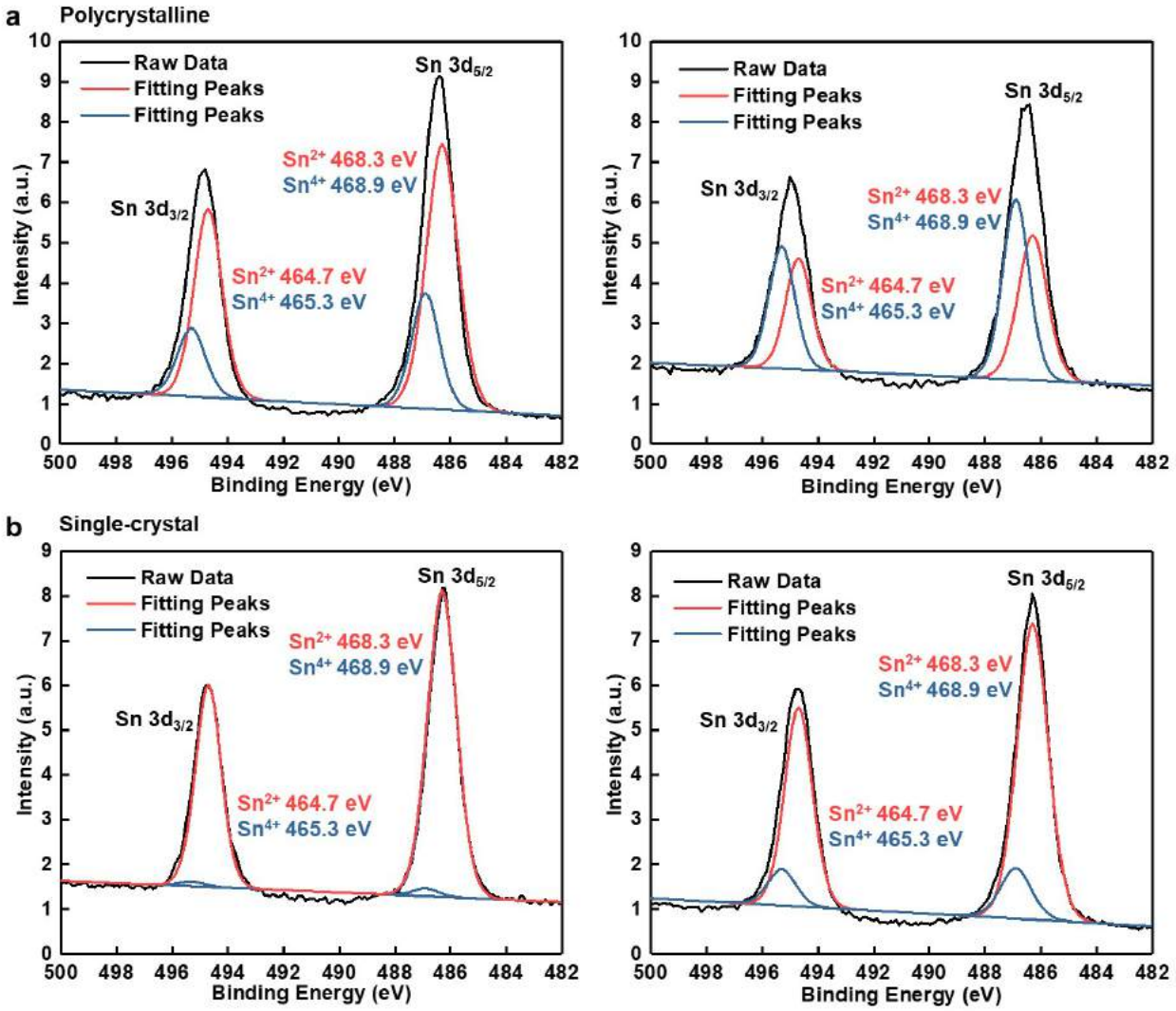

Supplementary Fig. 41 | Sn^{2+} oxidation mechanism studies with different crystal structures. **a**, XPS results of freshly prepared polycrystalline $MAPb_{0.5}Sn_{0.5}I_3$ (left) and aged polycrystalline $MAPb_{0.5}Sn_{0.5}I_3$ (right), where strong Sn^{4+} peaks can be fitted. **b**, XPS results of freshly prepared single-crystal $MAPb_{0.5}Sn_{0.5}I_3$ (left) and aged single-crystal $MAPb_{0.5}Sn_{0.5}I_3$ (right) under the same conditions, where the intensity of fitted Sn^{4+} peaks are much weaker than those in the polycrystalline samples, indicating the Sn^{2+} oxidation rate is much slower in the single-crystal than in the polycrystalline.

Single-crystal Thickness (μm)	J_{SC} (mA/cm^2)	V_{OC} (V)	FF (%)
~0.6	16.8	1.08	76
~0.9	17.4	1.07	76
~1.2	18.0	1.06	75
~1.5	18.7	1.06	74
~1.8	19.6	1.05	73
~2.1	20.1	1.03	72
~2.4	19.8	1.00	71

Supplementary Table 1. Absorber-thickness dependent photovoltaic performance. The data for each thickness is averaged from three separate devices. The thickness control is achieved by changing the growth time. All devices are in situ fabricated without transferring to isolate any possible confounding factors. The device structure is shown in Supplementary Fig. 15.

REFERENCES

1 Yang, W. S. et al. Iodide management in formamidinium-lead-halide-based perovskite layers for efficient solar cells. *Science* **356**, 1376-1379 (2017).

2 Lin, K. et al. Perovskite light-emitting diodes with external quantum efficiency exceeding 20 percent. *Nature* **562**, 245-248 (2018).

3 Feng, J. et al. Single-crystalline layered metal-halide perovskite nanowires for ultrasensitive photodetectors. *Nat. Electron.* **1**, 404-410 (2018).

4 NREL. *Best Research-Cell Efficiency Chart*.

5 Wang, Q. et al. Large fill-factor bilayer iodine perovskite solar cells fabricated by a low-temperature solution-process. *Energy Environ. Sci.* **7**, 2359-2365 (2014).

6 Chen, Z. et al. Thin single crystal perovskite solar cells to harvest below-bandgap light absorption. *Nat. Commun.* **8**, 1890 (2017).

7 Huang, Y. et al. The Exploration of Carrier Behavior in the Inverted Mixed Perovskite Single-Crystal Solar Cells. *Adv. Mater. Interfaces* **5**, 1800224 (2018).

8 Lee, L. et al. Wafer-scale single-crystal perovskite patterned thin films based on geometrically-confined lateral crystal growth. *Nat. Commun.* **8**, 15882 (2017).

9 Leblebici, S. Y. et al. Facet-dependent photovoltaic efficiency variations in single grains of hybrid halide perovskite. *Nat. Energy* **1**, 16093 (2016).

10 Zhang, W. et al. Enhanced optoelectronic quality of perovskite thin films with hypophosphorous acid for planar heterojunction solar cells. *Nat. Commun.* **6**, 10030 (2015).

11 Zheng, G. et al. Manipulation of facet orientation in hybrid perovskite polycrystalline films by cation cascade. *Nat. Commun.* **9**, 2793 (2018).

12 Zhao, Y. et al. Perovskite seeding growth of formamidinium-lead-iodide-based perovskites for efficient and stable solar cells. *Nat. Commun.* **9**, 1607 (2018).

13 Liu, Y. et al. Single-Crystal-like Perovskite for High-Performance Solar Cells Using the Effective Merged Annealing Method. *ACS Appl. Mater. Interfaces* **9**, 12382-12390 (2017).

14 Saidaminov, M. I. et al. High-quality bulk hybrid perovskite single crystals within minutes by inverse temperature crystallization. *Nat. Commun.* **6**, 7586 (2015).

15 Liu, M., Johnston, M. B. & Snaith, H. J. Efficient planar heterojunction perovskite solar cells by vapour deposition. *Nature* **501**, 395-398 (2013).

16 Chen, Z. et al. Single-Crystal $MAPbI_3$ Perovskite Solar Cells Exceeding 21% Power Conversion Efficiency. *ACS Energy Lett.* **4**, 1258-1259 (2019).

17 Lv, Q. et al. A universal top-down approach toward thickness-controllable perovskite single-crystalline thin films. *J. Mater. Chem. C* **6**, 4464-4470 (2018).

18 A decade of perovskite photovoltaics. *Nat. Energy* **4**, 1-1 (2019).

19 Lei, Y. et al. Controlled Homoepitaxial Growth of Hybrid Perovskites. *Adv Mater* **30**, e1705992 (2018).

20 Matthews, J. *Epitaxial growth*. (Elsevier, 2012).

21 Shi, D. et al. Low trap-state density and long carrier diffusion in organolead trihalide perovskite single crystals. *Science* **347**, 519-522 (2015).

22 Dong, Q. et al. Electron-hole diffusion lengths> 175 μm in solution-grown $CH_3NH_3PbI_3$ single crystals. *Science* **347**, 967-970 (2015).

23 Chen, Z. et al. Thin single crystal perovskite solar cells to harvest below-bandgap light absorption. *Nat. Commun.* **8**, 1890 (2017).

24 Wei, W. et al. Monolithic integration of hybrid perovskite single crystals with heterogenous substrate for highly sensitive X-ray imaging. *Nat. Photonics* **11**, 315 (2017).
25 Pearson, A. J. et al. Oxygen degradation in mesoporous $Al_2O_3/CH_3NH_3PbI_{3-x}Cl_x$ perovskite solar cells: kinetics and mechanisms. *Adv. Energy Mater.* **6**, 1600014 (2016).
26 Cowan, S. R., Roy, A. & Heeger, A. J. Recombination in polymer-fullerene bulk heterojunction solar cells. *Phys. Rev. B* **82**, 245207 (2010).
27 Olthof, S. & Meerholz, K. Substrate-dependent electronic structure and film formation of $MAPbI_3$ perovskites. *Sci. Rep.* **7**, 40267 (2017).
28 Climent-Pascual, E. et al. Influence of the substrate on the bulk properties of hybrid lead halide perovskite films. *J. Mater. Chem. A* **4**, 18153-18163 (2016).
29 Zhang, C. et al. Influence of different TiO_2 blocking films on the photovoltaic performance of perovskite solar cells. *Appl. Surf. Sci.* **388**, 82-88 (2016).
30 Fakharuddin, A., Schmidt- Mende, L., Garcia- Belmonte, G., Jose, R. & Mora- Sero, I. Interfaces in perovskite solar cells. *Adv. Energy Mater.* **7**, 1700623 (2017).
31 Furukawa, Y., Sato, M., Kitamura, K., Yajima, Y. & Minakata, M. Optical damage resistance and crystal quality of $LiNbO_3$ single crystals with various Li/Nb ratios. *J. Appl. Phys.* **72**, 3250-3254 (1992).
32 Liang, R., Bonn, D. & Hardy, W. Growth of high quality YBCO single crystals using $BaZrO_3$ crucibles. *Physica C: Superconductivity* **304**, 105-111 (1998).
33 Amano, H., Sawaki, N., Akasaki, I. & Toyoda, Y. Metalorganic vapor phase epitaxial growth of a high quality GaN film using an AlN buffer layer. *Appl. Phys. Lett.* **48**, 353-355 (1986).
34 Gfroerer, T. H. Photoluminescence in analysis of surfaces and interfaces. *Encyclopedia of analytical chemistry: applications, theory and instrumentation* (2006).
35 Zhang, D. et al. Atomic-resolution transmission electron microscopy of electron beam–sensitive crystalline materials. *Science* **359**, 675-679 (2018).
36 Tritt, T. M. *Thermal conductivity: theory, properties, and applications*. (Springer Science & Business Media, 2005).
37 Gantmakher, V. & Levinson, Y. *Carrier scattering in metals and semiconductors*. Vol. 19 (Elsevier, 2012).
38 Karakus, M. et al. Phonon–electron scattering limits free charge mobility in methylammonium lead iodide perovskites. *J. Phys. Chem. Lett.* **6**, 4991-4996 (2015).
39 Milot, R. L., Eperon, G. E., Snaith, H. J., Johnston, M. B. & Herz, L. M. Temperature-dependent charge- carrier dynamics in $CH_3NH_3PbI_3$ perovskite thin films. *Adv. Funct. Mater.* **25**, 6218-6227 (2015).
40 Biewald, A. et al. Temperature dependent ambipolar charge carrier mobility in large crystal hybrid halide perovskite thin films. *ACS Appl. Mater. Interfaces* (2019).
41 Filippetti, A., Mattoni, A., Caddeo, C., Saba, M. & Delugas, P. Low electron-polar optical phonon scattering as a fundamental aspect of carrier mobility in methylammonium lead halide $CH_3NH_3PbI_3$ perovskites. *Phys. Chem. Chem. Phys.* **18**, 15352-15362 (2016).
42 Liu, Y. et al. A 1300 mm^2 Ultrahigh- Performance Digital Imaging Assembly using High- Quality Perovskite Single Crystals. *Adv. Mater.* **30**, 1707314 (2018).
43 Liu, Y. et al. 120 mm single-crystalline perovskite and wafers: towards viable applications. *Sci. China Chem.* **60**, 1367-1376 (2017).
44 Klug, H. P. & Alexander, L. E. X-ray diffraction procedures: for polycrystalline and

amorphous materials. *X-Ray Diffraction Procedures: For Polycrystalline and Amorphous Materials, 2nd Edition, by Harold P. Klug, Leroy E. Alexander, pp. 992. ISBN 0-471-49369-4. Wiley-VCH, May 1974.*, 992 (1974).

45 Liu, Y. et al. Thinness- and shape- controlled growth for ultrathin single- crystalline perovskite wafers for mass production of superior photoelectronic devices. *Adv. Mater.* **28**, 9204-9209 (2016).

46 Stranks, S. D. et al. Electron-hole diffusion lengths exceeding 1 micrometer in an organometal trihalide perovskite absorber. *Science* **342**, 341-344 (2013).

47 Xing, G. et al. Long-range balanced electron-and hole-transport lengths in organic-inorganic $CH_3NH_3PbI_3$. *Science* **342**, 344-347 (2013).

48 Nie, W. et al. High-efficiency solution-processed perovskite solar cells with millimeter-scale grains. *Science* **347**, 522-525 (2015).

49 Liu, Z. et al. Gas-solid reaction based over one-micrometer thick stable perovskite films for efficient solar cells and modules. *Nat. Commun.* **9**, 3880 (2018).

50 Park, N.-G. Perovskite solar cells: an emerging photovoltaic technology. *Mater. Today* **18**, 65-72 (2015).

51 Chen, Z. et al. Thin single crystal perovskite solar cells to harvest below-bandgap light absorption. *Nat. Commun.* **8**, 1-7 (2017).

52 Yang, Y. et al. Top and bottom surfaces limit carrier lifetime in lead iodide perovskite films. *Nat. Energy* **2**, 16207 (2017).

53 Unger, E. L. et al. Hysteresis and transient behavior in current–voltage measurements of hybrid-perovskite absorber solar cells. *Energy Environ. Sci.* **7**, 3690-3698 (2014).

54 Correa-Baena, J.-P. et al. Identifying and suppressing interfacial recombination to achieve high open-circuit voltage in perovskite solar cells. *Energy Environ. Sci.* **10**, 1207-1212 (2017).

55 Wolff, C. M. et al. Reduced Interface- Mediated Recombination for High Open- Circuit Voltages in $CH_3NH_3PbI_3$ Solar Cells. *Adv. Mater.* **29**, 1700159 (2017).

56 O'Malley, K. M., Li, C. Z., Yip, H. L. & Jen, A. K. Y. Enhanced open- circuit voltage in high performance polymer/fullerene bulk- heterojunction solar cells by cathode modification with a C_{60} surfactant. *Adv. Energy Mater.* **2**, 82-86 (2012).

57 Leijtens, T. et al. Carrier trapping and recombination: the role of defect physics in enhancing the open circuit voltage of metal halide perovskite solar cells. *Energy Environ. Sci.* **9**, 3472-3481 (2016).

58 de Quilettes, D. W. et al. Impact of microstructure on local carrier lifetime in perovskite solar cells. *Science* **348**, 683-686 (2015).

59 Wu, X. et al. Trap states in lead iodide perovskites. *J. Am. Chem. Soc.* **137**, 2089-2096 (2015).

60 Chen, Q. et al. Controllable self-induced passivation of hybrid lead iodide perovskites toward high performance solar cells. *Nano Lett.* **14**, 4158-4163 (2014).

61 Noel, N. K. et al. Enhanced photoluminescence and solar cell performance via Lewis base passivation of organic–inorganic lead halide perovskites. *ACS Nano* **8**, 9815-9821 (2014).

62 Zheng, X. et al. Defect passivation in hybrid perovskite solar cells using quaternary ammonium halide anions and cations. *Nat. Energy* **2**, 17102 (2017).

63 Jiang, Q. et al. Surface passivation of perovskite film for efficient solar cells. *Nat. Photonics*, 1 (2019).

64 Li, B. et al. Surface passivation engineering strategy to fully-inorganic cubic $CsPbI_3$ perovskites for high-performance solar cells. *Nat. Commun.* **9**, 1076 (2018).
65 Tan, H. et al. Efficient and stable solution-processed planar perovskite solar cells via contact passivation. *Science* **355**, 722-726 (2017).
66 Gere, J. M. & Goodno, B. J. Mechanics of Materials 5th. *Brooks Cole*, 780 (2001).
67 Ćirić, L. et al. Mechanical response of $CH_3NH_3PbI_3$ nanowires. *Appl. Phys. Lett.* **112**, 111901 (2018).
68 Zu, F. et al. Constructing the Electronic Structure of $CH_3NH_3PbI_3$ and $CH_3NH_3PbBr_3$ Perovskite Thin Films from Single-Crystal Band Structure Measurements. *J. Phys. Chem. Lett.* **10**, 601-609 (2019).
69 Endres, J. et al. Valence and conduction band densities of states of metal halide perovskites: a combined experimental–theoretical study. *J. Phys. Chem. Lett.* **7**, 2722-2729 (2016).
70 Kresse, G. & Furthmüller, J. Efficient iterative schemes for ab initio total-energy calculations using a plane-wave basis set. *Phys. Rev. B* **54**, 11169 (1996).
71 Perdew, J. P., Burke, K. & Ernzerhof, M. Generalized gradient approximation made simple. *Phys. Rev. Lett.* **77**, 3865 (1996).
72 Setyawan, W. & Curtarolo, S. High-throughput electronic band structure calculations: Challenges and tools. *Comput. Mater. Sci.* **49**, 299-312 (2010).
73 Cai, S. in *IOP Conf. Ser. Earth Environ. Sci.* 022038 (IOP Publishing).
74 Bokdam, M. et al. Role of polar phonons in the photo excited state of metal halide perovskites. *Sci. Rep.* **6**, 1-8 (2016).
75 Yan, W. et al. Increasing open circuit voltage by adjusting work function of hole-transporting materials in perovskite solar cells. *Nano Res.* **9**, 1600-1608 (2016).
76 Suarez, B. et al. Recombination study of combined halides (Cl, Br, I) perovskite solar cells. *J. Phys. Chem. Lett.* **5**, 1628-1635 (2014).
77 Yan, W. et al. High-performance hybrid perovskite solar cells with open circuit voltage dependence on hole-transporting materials. *Nano Energy* **16**, 428-437 (2015).
78 Yang, Z. et al. Stable Low- Bandgap Pb–Sn Binary Perovskites for Tandem Solar Cells. *Adv. Mater.* **28**, 8990-8997 (2016).
79 Alshekhli, B. A. Theoretical Analysis of $Al_xGa_{1-x}As$/GaAs Graded Band Gap Solar Cell. *Al-Nahrain J. Sci.* **14**, 66-72 (2011).
80 Dullweber, T., Rau, U. & Schock, H. A new approach to high-efficiency solar cells by band gap grading in Cu (In, Ga) Se2 chalcopyrite semiconductors. *Sol. Energy Mater. Sol. Cells* **67**, 145-150 (2001).
81 Feng, J. Mechanical properties of hybrid organic-inorganic CH3NH3BX3 (B= Sn, Pb; X= Br, I) perovskites for solar cell absorbers. *APL Mater.* **2**, 081801 (2014).
82 Faghihnasiri, M., Izadifard, M. & Ghazi, M. E. DFT study of mechanical properties and stability of cubic methylammonium lead halide perovskites ($CH_3NH_3PbX_3$, X= I, Br, Cl). *J. Phys. Chem. C* **121**, 27059-27070 (2017).
83 Saraf, R., Tsui, T. & Maheshwari, V. Modulation of Mechanical Properties and Stable Light Energy Harvesting by Poling in Polymer Integrated Perovskite Films: A Wide Range, Linear and Highly Sensitive Tactile Sensor. *J. Mater. Chem. A* (2019).
84 Rakita, Y., Cohen, S. R., Kedem, N. K., Hodes, G. & Cahen, D. Mechanical properties of $APbX_3$ (A= Cs or CH_3NH_3; X= I or Br) perovskite single crystals. *MRS Commun.* **5**, 623-629 (2015).

85 Sun, S. et al. Factors influencing the mechanical properties of formamidinium lead halides and related hybrid perovskites. *ChemSusChem* **10**, 3740-3745 (2017).
86 Yu, J., Wang, M. & Lin, S. Probing the soft and nanoductile mechanical nature of single and polycrystalline organic–inorganic hybrid perovskites for flexible functional devices. *Acs Nano* **10**, 11044-11057 (2016).
87 Rösler, J., Harders, H. & Baeker, M. *Mechanical behaviour of engineering materials: metals, ceramics, polymers, and composites*. (Springer Science & Business Media, 2007).
88 Mezeix, L. & Green, D. J. Comparison of the mechanical properties of single crystal and polycrystalline yttrium aluminum garnet. *Int. J. Appl. Ceram. Technol.* **3**, 166-176 (2006).
89 Park, N.-G., Grätzel, M., Miyasaka, T., Zhu, K. & Emery, K. Towards stable and commercially available perovskite solar cells. *Nat. Energy* **1**, 16152 (2016).
90 Rong, Y. et al. Challenges for commercializing perovskite solar cells. *Science* **361**, eaat8235 (2018).
91 Rong, Y., Liu, L., Mei, A., Li, X. & Han, H. Beyond efficiency: the challenge of stability in mesoscopic perovskite solar cells. *Adv. Energy Mater.* **5**, 1501066 (2015).
92 Li, X. et al. Improved performance and stability of perovskite solar cells by crystal crosslinking with alkylphosphonic acid ω-ammonium chlorides. *Nat. Chem.* **7**, 703 (2015).
93 Deng, W. et al. Aligned single- crystalline perovskite microwire arrays for high-performance flexible image sensors with long- term stability. *Adv. Mater.* **28**, 2201-2208 (2016).
94 Futscher, M. H. et al. Quantification of ion migration in $CH_3NH_3PbI_3$ perovskite solar cells by transient capacitance measurements. *Mater. Horiz.* (2019).
95 Yun, J. S. et al. Critical role of grain boundaries for ion migration in formamidinium and methylammonium lead halide perovskite solar cells. *Adv. Energy Mater.* **6**, 1600330 (2016).
96 Shao, Y. et al. Grain boundary dominated ion migration in polycrystalline organic–inorganic halide perovskite films. *Energy Environ. Sci.* **9**, 1752-1759 (2016).
97 Ball, J. M. & Petrozza, A. Defects in perovskite-halides and their effects in solar cells. *Nat. Energy* **1**, 16149 (2016).
98 Sherkar, T. S. et al. Recombination in perovskite solar cells: significance of grain boundaries, interface traps, and defect ions. *ACS Energy Lett.* **2**, 1214-1222 (2017).
99 Azpiroz, J. M., Mosconi, E., Bisquert, J. & De Angelis, F. Defect migration in methylammonium lead iodide and its role in perovskite solar cell operation. *Energy Environ. Sci.* **8**, 2118-2127 (2015).
100 Yuan, Y. et al. Electric- field- driven reversible conversion between Methylammonium lead triiodide perovskites and lead iodide at elevated temperatures. *Adv. Energy Mater.* **6**, 1501803 (2016).
101 Seto, J. Y. The electrical properties of polycrystalline silicon films. *J. Appl. Phys.* **46**, 5247-5254 (1975).
102 Liu, L. et al. Grain- Boundary "Patches" by In Situ Conversion to Enhance Perovskite Solar Cells Stability. *Adv. Mater.* **30**, 1800544 (2018).
103 Sun, Q. et al. Role of microstructure in oxygen induced photodegradation of methylammonium lead triiodide perovskite films. *Adv. Energy Mater.* **7**, 1700977 (2017).
104 Shi, J., Xu, X., Li, D. & Meng, Q. Interfaces in perovskite solar cells. *Small* **11**, 2472-2486 (2015).

105 Ono, L. K., Qi, Y. & Liu, S. F. Progress toward stable lead halide perovskite solar cells. *Joule* **2**, 1961-1990 (2018).
106 Hawash, Z., Ono, L. K. & Qi, Y. Recent Advances in Spiro- MeOTAD Hole Transport Material and Its Applications in Organic–Inorganic Halide Perovskite Solar Cells. *Adv. Mater. Interfaces* **5**, 1700623 (2018).
107 Jeon, N. J. et al. A fluorene-terminated hole-transporting material for highly efficient and stable perovskite solar cells. *Nat. Energy* **3**, 682-689 (2018).
108 Xing, J. et al. Ultrafast ion migration in hybrid perovskite polycrystalline thin films under light and suppression in single crystals. *Phys. Chem. Chem. Phys.* **18**, 30484-30490 (2016).
109 Egger, D. A., Edri, E., Cahen, D. & Hodes, G. (ACS Publications, 2015).
110 Eames, C. et al. Ionic transport in hybrid lead iodide perovskite solar cells. *Nat. Commun.* **6**, 1-8 (2015).
111 Rajagopal, A., Yao, K. & Jen, A. K. Y. Toward perovskite solar cell commercialization: a perspective and research roadmap based on interfacial engineering. *Adv. Mater.* **30**, 1800455 (2018).
112 Berhe, T. A. et al. Organometal halide perovskite solar cells: degradation and stability. *Energy Environ. Sci.* **9**, 323-356 (2016).
113 Azpiroz, J. M., Mosconi, E., Bisquert, J. & De Angelis, F. Defect migration in methylammonium lead iodide and its role in perovskite solar cell operation. *Energy & Environmental Science* **8**, 2118-2127 (2015).
114 Haruyama, J., Sodeyama, K., Han, L. & Tateyama, Y. First-principles study of ion diffusion in perovskite solar cell sensitizers. *J. Am. Chem. Soc.* **137**, 10048-10051 (2015).
115 Meloni, S. et al. Ionic polarization-induced current–voltage hysteresis in $CH_3NH_3PbX_3$ perovskite solar cells. *Nat. Commun.* **7**, 1-9 (2016).
116 Futscher, M. H. et al. Quantification of ion migration in $CH_3NH_3PbI_3$ perovskite solar cells by transient capacitance measurements. *Mater. Horiz.* **6**, 1497-1503 (2019).
117 Hao, F., Stoumpos, C. C., Chang, R. P. & Kanatzidis, M. G. Anomalous band gap behavior in mixed Sn and Pb perovskites enables broadening of absorption spectrum in solar cells. *J. Am. Chem. Soc.* **136**, 8094-8099 (2014).
118 Leijtens, T., Prasanna, R., Gold-Parker, A., Toney, M. F. & McGehee, M. D. Mechanism of tin oxidation and stabilization by lead substitution in tin halide perovskites. *ACS Energy Lett.* **2**, 2159-2165 (2017).
119 Zuo, F. et al. Binary- Metal Perovskites Toward High- Performance Planar-Heterojunction Hybrid Solar Cells. *Adv. Mater.* **26**, 6454-6460 (2014).
120 Liu, X. et al. Improved efficiency and stability of Pb–Sn binary perovskite solar cells by Cs substitution. *J. Mater. Chem. A* **4**, 17939-17945 (2016).
121 Li, Y. et al. 50% Sn- Based Planar Perovskite Solar Cell with Power Conversion Efficiency up to 13.6%. *Adv. Energy Mater.* **6**, 1601353 (2016).
122 Yang, Z. et al. Stabilized wide bandgap perovskite solar cells by tin substitution. *Nano Lett.* **16**, 7739-7747 (2016).
123 Eperon, G. E. et al. Perovskite-perovskite tandem photovoltaics with optimized band gaps. *Science* **354**, 861-865 (2016).
124 Boyd, C. C., Cheacharoen, R., Leijtens, T. & McGehee, M. D. Understanding degradation mechanisms and improving stability of perovskite photovoltaics. *Chem. Rev.* **119**, 3418-3451 (2018).

125 Leijtens, T., Bush, K. A., Prasanna, R. & McGehee, M. D. Opportunities and challenges for tandem solar cells using metal halide perovskite semiconductors. *Nat. Energy* **3**, 828 (2018).

126 Saidaminov, M. I. et al. Planar-integrated single-crystalline perovskite photodetectors. *Nat. Commun.* **6**, 8724 (2015).

127 Maculan, G. et al. $CH_3NH_3PbCI_3$ single crystals: inverse temperature crystallization and visible-blind UV-photodetector. *J. Phys. Chem. Lett.* **6**, 3781-3786 (2015).

128 Liu, Y. et al. Multi-inch single-crystalline perovskite membrane for high-detectivity flexible photosensors. *Nat. Commun.* **9** (2018).

129 Wang, S., Jiang, Y., Juarez-Perez, E. J., Ono, L. K. & Qi, Y. Accelerated degradation of methylammonium lead iodide perovskites induced by exposure to iodine vapour. *Nat. Energy* **2**, 1-8 (2016).